

AD-A203 083

DEFORMATION, FRACTURE AND EXPLOSIVE
PROPERTIES OF REACTIVE MATERIALS

Principal Investigator: Dr. J. E. Field

EUROPEAN RESEARCH OFFICE

United States Army
London W1, England

Contract No. DAJA45-85-C-0052

DTIC
ELECTE
DEC 28 1988
S & D

FINAL TECHNICAL REPORT August 1988

Physics & Chemistry of Solids
Cavendish Laboratory
University of Cambridge
Madingley Road
Cambridge CB3 0HE
England

BEST
AVAILABLE COPY

DISTRIBUTION STATEMENT K
Approved for public release
Distribution Unlimited

"The research supported in this document has been made possible through the support and sponsorship of the US Government through its European Research office of the US Army. This report is intended only for the internal management use of the Contractor and the US Government"

DAJA45-85-C-0052
10/1/88
August 1988

88 12 27 026

Unclassified

SECURITY CLASSIFICATION OF THIS PAGE

A203 083

Form Approved
OMB No 0704-0188
Exp. Date Jun 30, 1986

REPORT DOCUMENTATION PAGE

1a. REPORT SECURITY CLASSIFICATION Unclassified			1b. RESTRICTIVE MARKINGS		
2a. SECURITY CLASSIFICATION AUTHORITY			3. DISTRIBUTION/AVAILABILITY OF REPORT Approved for public release; distribution unlimited		
2b. DECLASSIFICATION/DOWNGRADING SCHEDULE			5. MONITORING ORGANIZATION REPORT NUMBER(S) R&D 4380A-R-AN		
4. PERFORMING ORGANIZATION REPORT NUMBER(S)			6a. NAME OF PERFORMING ORGANIZATION University of Cambridge		
6b. OFFICE SYMBOL (if applicable)			7a. NAME OF MONITORING ORGANIZATION USARDSG(UK)		
6c. ADDRESS (City, State, and ZIP Code) Cavendish Laboratory, Madingley Road, Cambridge CB3 0HE, England			7b. ADDRESS (City, State, and ZIP Code) Box 65 FPO New York 09510-1500		
8a. NAME OF FUNDING/SPONSORING ORGANIZATION USARDSG(UK)		8b. OFFICE SYMBOL (if applicable) AMXSN-UK-RA		9. PROCUREMENT INSTRUMENT IDENTIFICATION NUMBER DAJA45-85-C-0052	
8c. ADDRESS (City, State, and ZIP Code) Box 65 FPO New York 09510-1500		10. SOURCE OF FUNDING NUMBERS		WORK UNIT ACCESSION NO	
		PROGRAM ELEMENT NO. 61103A		PROJECT NO. 1L161103BH57	
				TASK NO. 06	
11. TITLE (Include Security Classification) (U) Deformation, Fracture and Explosive Properties of Reactive Materials					
12. PERSONAL AUTHOR(S) J. E. Field, M. M. Chaudhri, J. N. Huntley, M. P. Parry, C. M. Pereira, S. J. F. Palmer, P. H. Pope					
13a. TYPE OF REPORT Final		13b. TIME COVERED FROM 85.11.12 TO 88.8.12		14. DATE OF REPORT (Year, Month, Day) 1988 . 8 . 22	
				15. PAGE COUNT 46 + 7i Figs.	
16. SUPPLEMENTARY NOTATION					
17. COSATI CODES			18. SUBJECT TERMS (Continue on reverse if necessary and identify by block number)		
FIELD	GROUP	SUB-GROUP			
19	01		Explosives, Ignition, Impact, Sensitiveness, Hot Spots,		
19	09		High Speed Photography, Deformation, Fracture, PETN, HMX, PBX		
19. ABSTRACT (Continue on reverse if necessary and identify by block number) See overleaf					
20. DISTRIBUTION/AVAILABILITY OF ABSTRACT <input checked="" type="checkbox"/> UNCLASSIFIED/UNLIMITED <input type="checkbox"/> SAME AS RPT. <input checked="" type="checkbox"/> DTIC USERS			21. ABSTRACT SECURITY CLASSIFICATION Unclassified		
22a. NAME OF RESPONSIBLE INDIVIDUAL Dr. Fritz H. Oertel, Jr.			22b. TELEPHONE (Include Area Code) 01-409 4423		22c. OFFICE SYMBOL AMXSN-UK-RA

DD FORM 1473, 84 MAR

83 APR edition may be used until exhausted.
All other editions are obsoleteSECURITY CLASSIFICATION OF THIS PAGE
Unclassified

ABSTRACT

A range of techniques have been developed for studies of the behaviour of explosives when impacted and for recording their strength, failure and ignition properties; these are described in Section 2. They include a drop-weight facility with transparent anvil, an instrumented drop-weight machine, a miniaturised Hopkinson bar system for high rate of strain property measurement, laser speckle for studies of deformation and fracture of PBX's, an automated system for analysing speckle and moiré records, and a heat sensitive film technique for recording the position and temperatures of "hot spots". The report gives data on the behaviour of polymer layers, binder materials, a range of PBX's, a range of HMX's of different particle sizes, and PETN when impacted in the drop-weight test. The data are in the form of force/time records and photographic observations (at microsecond framing intervals). As found in earlier studies, a variety of ignition mechanisms are possible during drop-weight impact. However, a considerable amount of evidence is given both for the occurrence of localised adiabatic shear (in polymers, PBX's, HMX and PETN) and for its importance in causing ignition. Significant advances have been made during this grant period in understanding the drop-weight test better. Situations giving ignition during loading and during unloading have been identified and the importance of anvil deformation is shown to be important. It is shown that it is useful to describe ignition, when viewed photographically as either "local" or "widespread". With HMX, studies were made with samples of five different particle sizes. The coarser material gave a more violent response (i.e. had a greater explosiveness). Two important factors which influence this are: (i) the compacted structure of the impacted samples which, with the coarser material, leaves more channels (porosity) for deflagration; and (ii) the greater thermal conductivity (by a factor of 2x) of compacted coarse grain material. Section 4 describes in detail the laser speckle techniques which allow the deformation and fracture of PBX's and other solids to be followed in detail. During the grant period the speed of processing by the automated methods has increased significantly. Section 5 gives data on the low strain rate deformation properties of AWRE and Los Alamos provided PBX's. The results were obtained using the Brazilian test geometry for stressing samples and the automated speckle techniques for recording their deformation. Section 6 gives microstructural information on PBX's including the initiation and growth of fracture through stressed samples. Finally, Section 7 describes optical and Raman studies of explosives under varying pressure and temperature conditions.

Accession For	
NTIS GRA&I	<input checked="" type="checkbox"/>
DTIC TAB	<input type="checkbox"/>
Unannounced	<input type="checkbox"/>
Justification	
Distribution	
Availability	
Notes	
List	
A-1	

Table of Contents

1. INTRODUCTION
2. EXPERIMENTAL
 - 2.1 High-speed photography; transparent drop-weight anvil apparatus.
 - 2.2 Instrumented drop-weight apparatus,
 - 2.3 Specimen failure in the drop-weight test.
 - 2.4 Miniaturised Hopkinson bar.
 - 2.5 Brazilian test and laser speckle for tensile strengths and strains to failure.
 - 2.6 Heat sensitive film technique.
3. RESULTS
 - 3.1 Hot spots produced during the deformation of polymers.
 - 3.2 Sensitisation of explosive layers by PTFE and Kel F 800.
 - 3.3 Impact on PE, PU and Viton.
 - 3.4 Drop-weight impact on PBX's; "local" and "widespread" initiation.
 - 3.5 Drop-weight impact on PETN; further evidence for ignition by adiabatic shear.
 - 3.6 Drop-weight impact on HMX:
 - (a) Experiments with heat sensitive film.
 - (b) Force-time curves.
 - (c) High-speed photography.
 - (d) Explosiveness and propagation; dependence on particle size.
 - 3.7 Hot-spot mechanisms during drop-weight impact.
4. THE APPLICATION OF LASER SPECKLE TO STRENGTH MEASUREMENT AND CRACK PROPAGATION
 - 4.1 Introduction.
 - 4.2 Laser speckle photography.
 - 4.3 Strength measurement of PBX's using the Brazilian test.
 - 4.4 Measurement of quasi-static displacement field around a crack tip.
 - 4.5 Measurement of dynamic displacement field around a crack tip.
 - 4.6 High resolution moiré photography.
 - 4.7 Conclusions.
5. QUASI-STATIC STRENGTHS AND STRAINS TO FAILURE OF SOME PBX'S
 - 5.1 Introduction.
 - 5.2 Experimental:
 - (a) Measurement of tensile strength.
 - (b) Measurement of strain.
 - (c) Analysis of speckle patterns and calculations of strains.
 - 5.3 Results.
 - 5.4 Discussions.
6. MICROSTRUCTURE AND FRACTURE PATHS IN PBX'S
 - 6.1 Introduction.
 - 6.2 Experimental:
 - (a) Polishing and staining techniques.
 - (b) Time-lapse photography.
 - 6.3 Results.
 - 6.4 Discussion.

**7. OPTICAL AND RAMAN STUDIES OF EXPLOSIVES UNDER
VARYING PRESSURE AND TEMPERATURE**

- 7.1 Introduction.
- 7.2 Experimental procedure.
- 7.3 Results and discussion.
 - (a) Optical absorption.
 - (b) Raman spectra.

REFERENCES

FIGURE CAPTIONS

1. INTRODUCTION

A range of techniques have been developed over the years for studies of the behaviour of explosives when impacted and for recording their strength, failure and ignition properties; these are described in Section 2. They include a drop-weight facility with transparent anvil, an instrumented drop-weight machine, a miniaturised Hopkinson bar system for high rate of strain property measurement, laser speckle for studies of deformation and fracture of PBX's, an automated system for analysing speckle and moiré records, and a heat sensitive film technique for recording the position and temperatures of "hot spots".

This report gives data on the behaviour of polymer layers, binder materials, a range of PBX's, a range of HMX's of different particle sizes, and PETN when impacted in the drop-weight test. The data are in the form of force/time records and photographic observations (at microsecond framing intervals). As found in earlier studies, a variety of ignition mechanisms are possible during drop-weight impact. However, a considerable amount of evidence is given both for the occurrence of localised adiabatic shear (in polymers, PBX's, HMX and PETN) and for its importance in causing ignition.

Significant advances have been made during this grant period in understanding the drop-weight test better. Situations giving ignition during loading and during unloading have been identified and the importance of anvil deformation is shown to be important. It is shown that it is useful to describe ignition, when viewed photographically as either "local" or "widespread".

With HMX, studies were made with samples of five different particle sizes. The coarser material gave a more violent response (i.e. had a greater explosiveness). Two important factors which influence this are: (i) the compacted structure of the impacted samples which, with the coarser material, leaves more channels (porosity) for deflagration; and (ii) the greater thermal conductivity (by a factor of 2x) of compacted coarse grain material.

Section 4 describes in detail the laser speckle techniques which allow the deformation and fracture of PBX's and other solids to be followed in detail. During the grant period the speed of processing by the automated methods has increased significantly.

Section 5 gives data on the low strain rate deformation properties of AWRE and Los Alamos provided PBX's. The results were obtained using the Brazilian test geometry for stressing samples and the automated speckle techniques for recording their deformation.

During the grant period techniques have been developed for polishing and staining PBX's. This has allowed the microstructure of PBX's to be examined. In some experiments specimens have been stressed to failure in the Brazilian test and fracture nucleation and growth followed by high magnification time-lapse photography; this work is described in Section 6.

Section 7 describes optical and Raman studies of explosives under varying pressure and temperature conditions. The pressure experiments were performed in a diamond anvil pressure cell. A study of the Raman spectrum of single crystals of silver azide for the temperature range 10 to 400K has recently been published (Pereira, C. M. and Chaudhri, M. M., 1988, Phil. Mag. A57, 173-185).

2. EXPERIMENTAL

This section summarises the main experimental approaches used in the research.

2.1 High speed photography; transparent anvil drop-weight apparatus

Advances in the understanding of explosive phenomena have been greatly assisted by direct observation of events using high-speed photography. The ability to obtain both temporal and spatial resolution in the heterogeneous process of impact initiation has been particularly valuable in establishing the sequence of events. The arrangement used in the present work was originally employed by Blackwood and Bowden [1] and has more recently been extensively used by Heavens, Field, Swallowe and others [2-9]. A schematic diagram of the apparatus is shown in fig. 1. Typically, 25 mg samples of material, in the form of powders, pressed discs or PBX samples, are compressed between toughened glass anvils with an impact velocity of typically 4.5 m s^{-1} . The drop weight (mass 5 kg) which bears the upper anvil is dropped from a height of up to ca. 1.5 m and is guided by three rods to ensure a planar impact. Shortly before contact, the mirror within the weight comes into alignment to complete the optical path from the xenon flash light source, through to the high-speed camera. A simple electrical contact is made at this point and triggers the light which has flash duration of 1 ms. The camera, an AWRE C4 rotating mirror camera, is of the continuous access variety so that synchronization is not required. The full length of film (140 frames) is scanned in approximately 1 ms so that the duration of the flash carries out the function of a shutter. There is usually some over-writing (double exposure) of some frames but it is not usually troublesome.

The view seen by the camera is along the axis of compression so that the basic behaviour observed is the expansion of the circular outline, seen in silhouette against the transmitted background light. Field et al. [6,7] determined that the initiation of explosive samples usually occurs after rapid radial flow (greater than ca. 100 m s^{-1}) unless sensitising grits are present. Valuable data which can be extracted from the photographs is therefore the radius as a function of time and, thereby, the velocity as a function of time. Rapid flow can occur as a result of mechanical failure of the sample but while this may be true in some cases, it is not a necessary precursor. If it is assumed that the material is sufficiently weak that it generates negligible retardation of the falling weight and that it deforms at constant volume, then high radial velocities are a natural outcome. The radius, r , as a function of time, t , is given by

$$r = r_0 \sqrt{\frac{h_0}{h_0 - vt}} \quad (1)$$

where r_0 is the initial radius, h_0 the initial height, and v the impact velocity. This function and the corresponding radial velocity are plotted in fig. 2. Although it is an idealisation, it is very useful since real materials can be described in terms of their departure from ideal.

In addition to the bulk plastic behaviour, other physical processes such as fracture, jetting, bulk plastic flow, localized adiabatic shear, melting and elastic recovery can be observed under favourable conditions. Explosive reaction is made visible since it is self-luminous, though early stages may be hidden within the opaque bulk, and as it develops the solid is consumed with the rapid expansion of gaseous products often being apparent.

Although photographs present a large amount of information, they cannot usually tell the whole story without corroborative evidence from other sources such as dynamic stress movement.

2.2 Instrumented drop-weight apparatus

A second drop-weight machine is available with instrumented steel anvils. A cross-section of the important features of the steel apparatus is shown in fig. 3. The system rests on a large blacksmith's anvil, which provides an almost ideal rigid support for a small load cell which measures the impact force. The cell is of in-house design, being made from a 12.7 mm x 12.7 mm steel bearing roller with a pair of strain gauges fixed axially on opposite sides of the roller. An impact cell is formed by two further rollers stacked on top of the load cell and test samples are placed between this pair, the whole arrangement being impacted by a weight of 2.5 or 4.7 kg, guided as before by three rods. The plain rollers may easily be replaced if they become damaged.

The dynamics of the system have been described in detail earlier [2,3], but a comparison with the behaviour of the direct impact Hopkinson bar (see section 2.4) is illuminating.

Unlike the Hopkinson bar, the dynamics of the drop weight system do not require explicit account to be taken of stress wave propagation. The pressure bar in our miniaturised Hopkinson apparatus is made deliberately long at 150 mm, so that a stress wave can be observed without interference from reflections. The drop-weight load cell is much shorter, being 25 mm including the protective roller on top of it, but the timescale over which it operates is much longer, 400 μ s compared with 16 μ s for the pressure bar. Consequently there are many stress wave reflections in the load cell and its behaviour is therefore quasi-static. In instrumentation terms, the pressure bar is used above its resonant frequency whereas the load cell is used below it. Similarly, the drop-weight itself is in stress equilibrium and can be regarded as rigid during the impact. The system therefore has two active components in the absence of a specimen, the drop weight mass and a spring composed of the three steel rollers. This is very familiar as a harmonic oscillator but one in which the "spring" only functions in compression. Elementary properties to emerge from this are that the contact force is a half sinusoid as a function of time and that the contact time is independent of the drop height and equal to half the period of the notional harmonic oscillator [2,3].

When a sample is present, its change in length as a function of time $l(t)$ is given by

$$l(t) = l_0 - v_0 t + \frac{f(t)}{k} + \int_0^t \int_0^t \frac{f(t')}{m} dt'^2 \quad (2)$$

where k is the spring constant, m the mass and $f(t)$ the force measured by the load cell.

The drop-weight is a relatively low accuracy machine by comparison with our Hopkinson bar apparatus and the calibration factor relating the output voltage from the load cell to the force can vary according to the weight used and the contact area between the rollers by about 10%. Calibration is carried out, analogous to the Hopkinson bar, by equating the area under the force-time curve to a known change in momentum of the weight and the sensitivity measured in this work was $75 \text{ kN V}^{-1} \pm 10\%$. Computer programs handle the data. As the apparatus is on a larger scale than the pressure bar, an additional check can be placed on the measurements by placing a steel "clash ring" around the specimen. This does not constrain the sample in any way but provides a defined end point to the compression which can be compared with calculation. It is also useful in avoiding the "pinch" regime (see later) with larger specimens where an explosion could cause considerable damage.

A further facility which is used with 25 mg samples when initiation is expected is the detection of electrical conductivity between the anvils. This can detect ionised gas and therefore pinpoint the initiation of explosion. A very simple circuit is used to monitor the current flowing between the anvils. Alternatively, ignition is detected by monitoring light output with a photo-cell.

2.3 Specimen failure in the drop-weight test

Failure by fracture is prevalent in specimens having a tall aspect ratio. The characteristic fracture patterns have been observed by Nadai [10], Timoshenko [11], and others. Nadai carried out a series of experiments on circular and square prisms of coloured paraffin wax which highlight regions of intense deformation by displaying stress whitening. The typical pattern is shown diagrammatically in fig. 4 for the most usual situation in which friction at the anvils is large. The supportive effect of the frictional forces results in regions near the anvils (marked I in the diagram) which remain essentially rigid and are forced into the bulk of the material. This results in intense shear along the lines marked S which may result in a shear fracture. The remaining material in region II is subjected to tensile hoop stresses (in the cylindrical case) due to the wedging effect of the advancing cones (region I). This results in vertical cracks running between the anvils so that region II is fragmented.

In an explosive, initiation is unlikely during this phase since the pressures are low, but the mode of failure by tensile or shear fracture may control the de-bonding process in PBXs and by creating particular kinds of surface morphology could influence the propagation of reaction at a later stage.

As compression proceeds, the fragmentation of region II continues and the rigid cones approach each other until their tips meet, at which point the load required to continue deformation begins to increase. The cones then begin to deform plastically first at the tip and then, progressively, towards the anvils until the situation shown in fig. 4(b) is reached. Now the plastic region (region III) occupies almost all the specimen although the rigid region I and brittle region II are still present. During this compaction stage some fragmented material is reconsolidated so that region III grows at the expense of region II. In the process, some voids may be incorporated in region III and this is significant for explosives since adiabatic compression of the resulting gas spaces forms a potential ignition mechanism.

In the final stages of compression, sometimes referred to in the explosives field at the "pinch" regime, the hydrostatic stress component can be very large and if, for the time being, region II is ignored the remaining situation is a classic problem in plasticity. The first solution to the two-dimensional problem was given by Prandtl [12] and later by Hill [13]. The slip-line field derived by these authors is shown in fig. 4(c). The presence of the central rigid regions is an indication that the hydrostatic stress component contributed by the axial load and the frictional traction prevents yield at these points. The Prandtl solution assumes a von Mises yield criterion and permits the pressure distribution to be calculated. In the case of axial symmetry, the problem is soluble if one assumes a so-called "Haar-von Karman" stress state in which two of the principle stresses are equal, in this case the radial and tangential stresses. The result for this has been given by Schroeder and Webster [14] which predicts a mean pressure, p , given by:

$$p = Y \left(1 + \frac{d}{3h\sqrt{3}} \right) \quad (3)$$

where Y is the uniaxial yield stress and d and h are the diameter and thickness of the sample respectively. In this "pinch" regime, it is quite possible to have mean pressures of 20 times the uniaxial yield stress and when combined with a substantial degree of shear, ideal conditions for explosive initiation can occur [15,16, 2-9]. In fact, the Prandtl velocity field includes a discontinuity at the boundary of the rigid region and this might be a prime site for initiation. Equation 3 also helps explain why there are often size effects during drop weight impact; note the importance of the ration d/h .

While this analysis gives some insight into the loading conditions, the assumption of a von Mises material is not ideal for granular explosives which might be expected to show a Coulomb

yield criterion. Since this assumes that the shear yield stress of the material increases as the hydrostatic pressure increases, it might be anticipated that such a material could support higher stresses than the von Mises equivalent. This is an area of current study.

2.4 Miniaturised Hopkinson bar

In a conventional Hopkinson bar system (see, for example, [17]), the specimen is placed between two long, cylindrical rods. A stress pulse is then sent down the input bar and gauges record the incident, reflected and transmitted waves. From these records, it is possible to obtain the stress/strain behaviour of the specimen of strain rates of ca. 10^3 s^{-1} . A few years ago [18], we developed a direct impact (no input bar) miniaturised system (see fig. 5). Initially, we used a high-speed camera to measure strains, but this is not essential and stress strain curves can be obtained from the gauge records on the output bar following an analysis given by Pope and Field [19]. The advantages of the new apparatus are that strain rates up to ca. 10^5 s^{-1} can be achieved and high strength specimens investigated. We have used the apparatus to measure the dynamic properties of PBXs supplied by AWRE, and some results were published in [9]. Our capabilities for measuring stress-strain curves range from Instron-type machines which can cover the low strain rate, drop weight machines ($\dot{\epsilon}$, 10^2 to 10^3), and the miniaturised Hopkinson bar system ($\dot{\epsilon}$, 10^4 to 10^5). Our results on PBXs show that compositions containing micronised explosive are in general stronger and that strengths at $\dot{\epsilon}$ of $2 \times 10^4 \text{ s}^{-1}$ can be at least double those at $\dot{\epsilon}$ of 10 s^{-1} . To date, the largest increases in strength with strain rate recorded have been with micronised HMX in polyurethane where the ultimate compressible strength increased from ca. 30 MPa to ca. 140 MPa.

2.5 Brazilian test and laser speckle for tensile strengths and strains to failure

The tensile strengths and rupture strains of a variety of PBX compositions were studied, at strain rates of ca. 10^{-4} s^{-1} , using the Brazilian test geometry and laser speckle photography. The Brazilian test is illustrated in fig. 6. The compression induces tensile stresses normal to the loading axis which are sensibly constant over a region about the centre of a specimen. The tensile strength of the material is then calculated from

$$\sigma_t = 2P / \pi Dt \quad (4)$$

in which P is the failure load, and D and t the diameter and thickness of the specimen respectively. The validity of equation (4) is based on the assumptions that failure occurs at the point of maximum tensile stress (i.e. at the centre), and that the compressive stress has no influence on the failure. In practice, the use of plan anvils can produce very high contact stresses at the loading points, and lead to the collapse of the contact edge. Awaji and Sata [20] have shown that by using curved anvils, collapse of the edge can be avoided, and shear stresses under the points of loading may be substantially reduced. If the ratio of the contact half-width, b , to the disc radius, R , is larger than approximately 0.27, the maximum principle stresses near the contact area are compressive. Then the stresses near the centre of the disc control the fracture, and cracking occurs at the centre, at a maximum tensile stress given by:

$$\sigma_t^* = \{1 - (b/R)^2\} \sigma_t \quad (5)$$

Other workers [21-23] using the Brazilian test geometry have employed displacement transducers to measure the average tensile strain across a diameter. However, the use of a relatively simple optical technique called "speckle photography", enables one to measure in-plane displacements to an accuracy of ca. $0.1 \mu\text{m}$ at different positions on the sample surface, and thereby determine the strain field at any point [24,25]. There is the added advantage that it is a remote sensing technique which does not involve adding gauges to the sample. For displacement and strain measurements, a double exposure is photographically recorded before and after deformation. The negative then consists of two identical speckle patterns that have been translated with respect to each other.

Displacement information can be extracted in a point-wise manner, by allowing an unexpanded laser beam to pass through the negative. If, at the point illuminated by the beam, the "speckles" have been displaced between exposures, the resulting displacement vector is manifested by a Young's fringe pattern observed on a screen placed at the far-field Fraunhofer diffraction plane. The displacement vector is perpendicular to the fringe orientation and the magnitude inversely proportional to the fringe spacing. However, complete analysis involves many measurements, and the procedure becomes tedious when performed manually. For this reason, a fully automatic electro-optical system for measuring the displacement field from a double exposure speckle photograph has been constructed [26].

Data obtained on 12 AWRE and 2 Los Alamos PBXs were reported in [9].

2.6 Heat sensitive film technique

The deformation of materials at high rates of strain leads to the conversion of mechanical energy into heat. Depending on the mode of deformation, this heating may be localized at crack tips or on shear planes, or it may produce a more uniform bulk temperature rise. The temperature rises produced during these processes can be very high and for materials such as polymers or explosives can lead to thermal decomposition, or, in the case of metals, phase transformations. Because of the transient nature of this heating, measurement of the temperatures involved is difficult. In this paper, we describe a simple technique based on the use of a heat sensitive film which gives the spatial distribution of heating. If used in conjunction with a technique such as high-speed photography, which provides temporal information about the deformation process, it is shown that reasonably accurate measurements of temperature can also be obtained. We have applied the technique to the deformation during impact of a wide range of polymers and explosives.

The technique used in this work was first suggested by Coffey and Jacobs [27]. It is based on the use of an acetate sheet coated with a sensitive layer which darkens on exposure to heat. The sheets are commercially produced for the production of transparencies for overhead projectors (3M type 570). The sheets do not darken when exposed to light or infrared radiation out to $10\text{ }\mu\text{m}$ [27]. Film darkening does not occur when the sheets are torn or impacted with peak pressures up to at least 1 GPa, and the darkening produced by heating is stable at room temperatures for periods of at least a year. However, if the film is subjected to high loading stresses at high strain rates ($\epsilon > 10^4$) catastrophic failure of this film backing may occur which will induce darkening of the sensitive layer. Details of the composition of the sensitive layer may be found in [28]. For very short duration heat pulses ($< 10^{-4}$ sec) the film colour obtained is yellowish-brown rather than black and the degree of darkening increases in intensity as the contact time is increased, until the film is fully blackened. The yellow-brown colouration is believed to be due to the reaction in the sensitive layer being unable to go to completion in the time available.

Film darkening is a function of both temperature and time so, in order to use the film to estimate the temperature achieved during deformation, one must know the time over which the deformation occurred and then refer to a set of calibration curves (darkening as a function of time and temperature) for the film. The film was calibrated by cutting out small circular discs (4 mm diameter) and attaching them sensitive side outwards to cylindrical steel rollers (5 mm diameter) using double-sided sellotape. The rollers were dropped down an accurately vertical tube onto a variable temperature hot plate whose surface temperature was measured using a chromel-alumel thermocouple. A simple catcher arm was used to prevent repeated impacts of the roller on the hot surface (fig. 7). The contact time of the heat sensitive layer on the hot plate was varied by using rollers of different lengths and by incorporating polymeric layers as sandwiches between the film and steel roller. The contact time for the impact of a cylinder depends on the double transit time of the stress wave in the cylinder. With a "soft" polymeric layer added, the contact time is increased.

Contact times were measured by dropping the rollers onto a 1 mm thick piezoelectric crystal mounted on the hot-plate surface and measuring the voltage pulses produced. A range of contact times from 30 to 600 μsec was obtained and plots of the optical density of the film measured relative to a standard reference on a Joyce Mk III B microdensitometer are illustrated in fig. 8. The

film colouration was quite grainy (grains ~ 0.2 mm) and this gave rise to random variations in optical density about the mean value for any given temperature and time of contact. The extent of this graininess is illustrated by the error bars on the calibration curves (fig. 8).

In order to use the calibration to obtain a temperature in an impact experiment, it was necessary to measure the time during which the events which caused the darkening took place. These measurements were made by using an Atomic Weapons Research Establishment designed high speed camera (C4) at a framing rate of 7 μ sec per frame to photograph the processes occurring during impact. The experimental set up is fully described by Heavens and Field [2,3]. Basically the system allows the impact process to be viewed perpendicular to the plane of the impact by using toughened glass anvil material in a drop-weight machine (see fig. 1). All the high-speed photographic sequences illustrated in this paper have been obtained with this system. Experiments were carried out by placing a small square of the film surmounted by the sample on the glass anvil with the sensitive side in contact with the sample. Impacts were photographed using the high speed camera system, and the temporal information from the photographic sequences was used in conjunction with the calibration curves to obtain estimates of the temperatures reached during sample deformation.

3. RESULTS

3.1 Hot spots produced during the deformation of polymers

Earlier research [4-6] has shown that some polymers can sensitise explosives despite polymers having low melting points. Polymers which do sensitise tend to be those which fail catastrophically by fracture or adiabatic shear bonding. The heat-sensitive film technique, when used in combination with high-speed photography (see section 2.6), allows hot-spots to be located and their temperatures estimated.

Experiments have been carried out on a range of polymers. The materials investigated were polymethylmethacrylate (PMMA), polycarbonate (PC), polystyrene (PS), polytetrafluorethylene (PTFE), nylon 6, high density polyethylene (HDPE), polypropylene (PP) and polyvinylchloride (PVC). All the samples investigated were cylindrical and were approximately 5 mm in diameter and 1 mm high. Samples were produced either by slicing a cylindrical rod of the material or by punching discs from flat cast sheets.

Broadly speaking, the materials investigated fell into two categories, those which failed by shear banding or cracking (PMMA, PC, PS, PTFE) and those in which mainly bulk plastic deformation was observed (PP, HDPE, nylon, PVC). Fig. 9 is a typical high-speed photographic sequence for the latter type of behaviour. It shows a 5 mm diameter disc of PP (central dark region) which expands radially during the course of the impact. No cracking or shearing is observed. Fig. 10 illustrates the pattern left on the heat sensitive film after such an impact. Neglecting the no-flow zone at the centre, the darkening is concentrated towards the central area (the impact was not perfectly symmetric and occurred initially at the lower part of the disc as illustrated here). An indirect estimate of the temperature reached during the flow process can be made by using the high-speed photographs to work out the amount of time during which plastic flow had been occurring at the boundary of the darkened region. For PP, this time turns out to be 300 μ sec. Since darkening is just occurring after 300 μ sec, the temperature is likely to be $\sim 230^\circ\text{C}$ (given by the lower point on the 330 μ sec calibration curve). Similar calculations for the other bulk deforming polymers yield temperatures of $\sim 400^\circ\text{C}$ for nylon 6 and an upper limit of 200°C for HDPE. Fig. 11 shows a typical trace left on the film for a sample of nylon. It is clear from just a casual visual inspection of these traces that the temperature reached in the nylon is very much greater than that in PP which is in turn greater than that of HDPE, since *no* colouration is obtained with HDPE samples.

The behaviour of PVC was similar to that of the materials described above. Most of the heating took place during the bulk plastic stage of deformation and the trace left on the film was similar to that for nylon. Although a ring-type fracture of the material did occur at a strain of ~ 0.4 , producing a "tyre" around the main bulk of the sample, this did not leave any trace on the heat-sensitive film. The temperature reached during bulk deformation was estimated to be $450 \pm 100^\circ\text{C}$ and was high enough to produce severe distortion of the sample and heating of the film backing on several occasions.

PC, PMMA, PS and PTFE all sensitise explosives and all deformed first by bulk plastic flow and then with the production of "parallel" and "perpendicular" cracks, followed by general random cracking. The word "cracks" is used here because when a specimen is examined after impact, it separates along these visible lines. However, both fracture and shear banding can be found with PC, PMMA and PS and with some of the line features shear failure almost certainly occurred initially. The sequence of cracking is illustrated in the drawings of fig. 12. The deformation could be halted at any of the stages illustrated by judicious variation of the height from which the weight was dropped on the sample. Use of the heat-sensitive film in conjunction with variations in the drop height of the weight showed that the amount of film darkening was the same for each set of cracks and that the darkening took place at the intersection of cracks with the surface.

The extent of the bulk deformation and timescale of the cracking were different for the different materials. Fig. 13 illustrates this behaviour for PS. Bulk deformation occurs in frames

(a) and (b) and then at a strain of 0.003 "parallel" cracks are produced sequentially across the specimen, frames (c)-(g). These cracks are then connected by "perpendicular" cracks, and eventually the sample becomes covered in a network of cracks (frame (h)). The timespan from first production of the "parallel" cracks to the final multiple cracking is $\sim 250 \mu\text{sec}$. Fig. 14 illustrates a similar sequence for PC. Bulk deformation from frames (a)-(e) then at a strain of 1.1 cracking occurs. However, in this case the failure of the sample is much more rapid and cracking is complete by frame (i), a timespan of $25 \mu\text{sec}$. PMMA behaves in a similar manner, cracking occurring when the strain is ~ 0.04 but the duration of cracking is now $\sim 400 \mu\text{sec}$. Table 1 summarizes the behaviour of these polymers for loading of similar sized samples by impacts with the same weight dropped from approximately the same height (5 kg mass from $\sim 0.5 \text{ m}$).

Of the polymers which cracked during deformation, only very slight darkening was produced when the impact energy was restricted so as to prevent cracking whilst still allowing some plastic deformation to occur. This implies that the temperature achieved during bulk deformation of these materials cannot be much more than 200°C . Fig. 15 illustrates the traces obtained for a crack running through a sample of PMMA. It can be seen that the dark line on the film follows the course of the crack. Measurement of the optical density of the trace together with an estimate of the time of heating yield a temperature of $530 \pm 50^\circ\text{C}$. This is in very good agreement with the value of 500°C quoted by Fuller et al. [29] for cracks in PMMA moving at similar velocities but measured by a totally independent technique.

Fig. 16 illustrates the pattern left on the film after the failure of a sample of PC. It is clear that the darkening is irregular and in some areas very intense. Measurement of the optical density of the most intense areas with an estimated heating time of $30 \mu\text{sec}$ yield peak temperatures $\sim 700^\circ\text{C}$. For materials which undergo catastrophic failure (PC) the estimated heating time is typically 30 to $50 \mu\text{sec}$.

With materials such as PS, PTFE and PMMA, the total deformation process could take several hundred microseconds. However, the high speed photographs showed that stages of this deformation could take place very rapidly with a set of cracks taking 20 to $30 \mu\text{sec}$ to form. Fig. 12, frames (b)-(d), is an example of a set of parallel cracks in PS which took $\sim 20 \mu\text{sec}$ to form.

These times are reasonable estimates of the duration of the high temperature regions since measurements by Fuller et al. [29] on PMMA and PS, using an infrared detector to observe the temperature rise after the passage of a crack, yield values of $\sim 10 \mu\text{sec}$ for the rise time of the temperature pulse in PMMA and PS for cracks travelling at similar velocities to those we have observed. Taking $1 \mu\text{m}$ as being a typical thickness of the plastic zone ahead of the crack tip ($2 \times$ typical craze thickness) and assuming the temperature drops by diffusion of heat into the bulk material, we find that the time taken for the temperature to drop to < 200 from 500°C would be $20 \mu\text{sec}$ using $T = T_0 \text{erf}[R/(4kt)^{1/2}]$ [30], where T is the temperature after time t , T_0 is the initial temperature rise in a hot region of thickness R , and k is the thermal diffusivity which for a polymer is typically $10^{-7} \text{ m}^2 \text{ sec}^{-1}$. The total heating time of the film would therefore be typically $30 \mu\text{sec}$. The actual peak temperatures achieved in the polymer may be even higher than the values quoted in table 1, since our estimates of duration of film heating includes the time taken to reach the peak as well as to drop below values which will cause no further film darkening.

Our experimental results indicate that in polymers which are subject to cracking very high temperatures are reached in the crack zone. These temperatures are higher than could be achieved by conversion of the energy of the falling weight directly into heat throughout the sample. Assuming no energy losses and complete conversion of mechanical energy into heat, a temperature rise of 600°C would be expected in our samples taking a value of $2 \text{ kJ kg}^{-1} ^\circ\text{C}^{-1}$ as a typical specific heat. Differential scanning calorimetry (DSC) experiments over the range 50 to 350°C yielded values of specific heat which varied in an approximately linear value from 1.3 at 50°C to $2.4 \text{ kJ kg}^{-1} ^\circ\text{C}^{-1}$ at 350°C for PC and 1.9 at 50°C to $2.1 \text{ kJ kg}^{-1} ^\circ\text{C}^{-1}$ at its melting point (130°C) for PP. The specific heat of PMMA has been found to be relatively constant at $2.9 \text{ kJ kg}^{-1} ^\circ\text{C}^{-1}$ until decomposition occurred at $\sim 360^\circ\text{C}$.

However, the assumption of complete conversion of the mechanical energy of the falling weight into heat in the sample is rather unrealistic. Typically 20 to 30% of the impact energy will be used in elastic energy in the system which causes the weight to recoil. Smaller portions of the impact energy probably totalling another 10% will be used in plastic distortion of the machine components and emitted as sound waves. Thus one would expect at most 2/3 of the impact energy to be deposited in the sample, yielding a maximum expected temperature rise of 400°C which is in agreement with our results (since temperature rise of approximately 450°C is in fact the maximum that is observed in those materials which deform in our equipment solely by bulk plastic deformation).

If one assumes that the temperature produced at the crack tip is due to the release of elastic stored energy one would expect those materials in which the failure was most catastrophic, i.e. the energy release rate was highest, to produce the highest temperatures. Inspection of table 1 will confirm that this is indeed the case. However the release rate will not be the only factor in determining potential for production of high temperatures. Consideration must also be given to the magnitude of the stored energy. This will be determined by the stress at which failure occurs and the failure strain less the residual strain ($\epsilon_f - \epsilon_r$). A measure of the residual strain may be obtained by carrying out experiments to just less than ϵ_f and observing the strain in the sample after the experiment. Information on the failure stress and strain can be obtained from standard compressional stress-strain curves. Unfortunately this information is not readily available for the materials of interest at the appropriate strain rates ($\dot{\epsilon} \sim 10^2 \text{ sec}^{-1}$). Work on the production of stress-strain curves at strain rates of 10^2 to 10^3 to high total strains is currently in progress in this laboratory. However, table 1 does reveal that those materials which fracture at higher strains produce higher temperatures.

Table 1

The last four polymers can sensitize explosive layers when impacted

TABLE I

	A^* natural strain	Time of cracking	Max temperature of plastic deformation	Max observed crack temperature	Latent heat [†] (kJ kg)
HDPE	0.9	—	< 200	—	120
PP	> 2.5	—	230	—	95
NYLON 6	1.0	—	400	—	130
PVC	0.7	—	450	—	60
PS	0.01	250	< 200	550	—
PMMA	0.04	400	< 200	530	—
PTFE	0.25	150	< 200	600	37
PC	1.1	20	< 200	700	7.2

A^* represents the strain at which cracking occurs or the observed maximum plastic strain.

[†] obtained on a Mettler DSC-30.

The prediction of a high yield stress leading to higher temperature during failure is supported by the work of Krishna Mohan and Field [7] who carried out impact experiments on explosive layers and observed that those materials which had the highest yield strengths were most likely to ignite in an impact experiment. However, in order to make a quantitative comparison between the estimates of temperatures produced during deformation and the mechanical properties of the materials it will be necessary to produce a set of stress-strain curves for the polymers at strain rates appropriate to our impact conditions.

Another factor which can limit the potential for high temperature production is the latent heat of any phase transformation that may occur before a high temperature is reached. The most common will be melting or softening of the material and one finds that those materials which have a definite melting range with a high latent heat produce the lower temperatures. Measurements of the latent heats made on the materials using a Mettler DSC 30 are included in table 1.

It is not too surprising that some polymers reach high local temperatures (well above their softening temperatures) during rapid deformation. Polymers in general have relatively low thermal capacities and conductivities and still retain a high viscosity even when the softening temperatures are exceeded. High temperatures are favoured, particularly in those which fail at high stresses such as, for example, PC. In contrast, polymers such as HDPE and PP have much lower yield stresses and noticeably higher latent heats (see table 1). Both of these factors favour bulk, rather than localized, deformation and the attainment of lower temperatures.

It is clear that there are a large number of factors which determine how high a temperature is likely to be produced in a material during impact and that prediction of the likely temperature rises is a difficult task. The method of direct measurement outlined here does however produce a useful experiment window onto these short timescale temperature excursions.

The use of heat sensitive film has been demonstrated to give spatially resolved information on the temperatures produced during the deformation of polymers. It is a simple technique which, when calibrated, gives quantitative results or, uncalibrated, can be used to provide comparative information on a range of materials. It is of particular use with soft materials, such as polymers, which do not cause damage to the backing layer during deformation. The present work has considerably extended the range of the technique from the first proposals of Coffey and Jacobs [27] who only undertook a very limited calibration and did not use cameras to follow the progress of the deformation. A paper on this research has now been published [31]. Other examples of the use of the heat sensitive technique are given in later sections.

3.2 Sensitisation of explosive layers by PTFE and Kel-F 800

In several PBXs of current interest, PTFE and Kel-F 800 (a copolymer of chlorotrifluoroethene and vinylidene fluoride) are used as binders. Although the sizes of polymer particles in the moulding powders are considerably smaller than those used in our previous studies [4-6], the SEM showed that the particle size of PTFE in particular may be many tens of microns. It was considered worthwhile to investigate the effect of impact upon these two polymers and to determine what effect they have on the sensitiveness of explosives in the drop-weight test.

Impacts on pure polymers were carried out on both irregular and disc-shaped samples up to 5 mm in diameter and 2 mm thick. 10-15 mg samples of PETN containing small pieces of the polymers were pressed at 650 MPa into 3 mm diameter pellets for the photographic investigation and for a quantitative determination of the effects of the two polymers on PETN. H_{50} heights were determined for the pure explosive and the explosive + polymer in the form of a loosely compacted pellet containing 10 mg PETN. These samples were placed on the top of roller R2 (see fig. 3) and a single, small piece of polymer placed on top of the PETN. 25 drops on each sample type were performed. In extending the examination of the deformation of polymers in the glass anvil drop-weight machine, the technique of placing the sample on heat-sensitive film (3M type 570) and then impacting, was employed (see section 3.1). By combining this technique with high-speed photography, estimates of the temperatures attained in the polymers during impact were made.

Photographic records of the behaviour of PTFE and Kel-F 800 under the impact of a 5.5 kg mass from 1 m showed that the polymers underwent plastic deformation at velocities of 20-40 m s⁻¹. Neither failed as catastrophically as polysulphone or polycarbonate [4-6], but the remains of the impacted PTFE showed that extensive fracture had occurred. Kel-F 800 showed evidence for bulk plastic flow associated with extensive softening together with a minor amount of fracture. Both polymers caused extensive darkening of the heat-sensitive film. With PTFE, the darkest areas were located in the regions of the fracture whereas with Kel-F 800, the film was uniformly darkened. Analysis of the photographic and heat-sensitive film records according to the method outlined above gave temperatures of 650 ± 50 K for PTFE and 700 ± 50 K for Kel-F 800. The temperature attained by PTFE was slightly lower than that found for polymers which underwent massive deformation by cracking and shearing; the high value for Kel-F 800 was, however, not unusual for a tough material that undergoes bulk plastic flow.

Extensive drop-weight tests on PETN [2,3] showed that the explosive first undergoes plastic flow followed by the material becoming translucent and finally transparent at which stage the velocity of flow between the anvils attained 300 m s^{-1} . Shear bands were observed in the explosive before the sample melted and if ignition of the material occurred, it invariably took place at a limited number of locations after the high flow velocity regime. When polymers were mixed with PETN, localisation of the impact energy into "hot spots" occurred when the polymer underwent catastrophic failure and could lead to ignition sites developing before the PETN underwent rapid flow [5].

Fig. 17 shows an impact sequence of PETN + Kel-F 800. The PETN/polymer pellet was impacted in frame 2 and deformed plastically; shear bands in the PETN were apparent (labelled A in frame 5). By this stage the PETN had become partially translucent but no rapid flow was observed. Despite this, an ignition site (labelled B in frame 6) developed at the junction of PETN and Kel-F 800 which propagated throughout the explosive, consuming it. This behaviour was repeatable and observed with both polymers. Confirmation of the sensitising effect that PETN and Kel-F 800 imparted to PETN was obtained from the 2.4 kg drop-weight apparatus (table 2).

Stress-strain curves for the two polymers at initial strain rates of $1.1 \times 10^3 \text{ s}^{-1}$ are shown in fig. 18. Both polymers exhibited a small region of elastic behaviour followed by the major plastic deformation regime. Kel-F 800 showed considerable strain softening and was capable of greater strains than those achieved by PTFE. Although there was a difference in the failure mode of the two polymers, neither failed as catastrophically as polysulphone or polycarbonate [4-6]. The ability of PTFE and Kel-F 800 to sensitise explosives to impact was found to agree with the theory proposed by Swallowe and Field [4-6]. PTFE was seen to undergo extensive fracturing upon failure, thereby concentrating the stored impact energy along discrete zones which were found to attain high temperatures. With Kel-F 800, the impact energy was not localised but the whole of the material attained elevated temperatures by means of bulk plastic flow to high strains, together with viscous heating before failure occurred. Because of the low latent heat value (3.9 kJ kg^{-1}), little energy was absorbed when the Kel-F 800 softened and therefore only minor assistance was afforded in relieving the energy build-up in the sample. Consequently both polymers were found to exert a sensitising influence on PETN, but by different mechanisms. The results of this section have now been published in [32].

Table 2

50% heights for PETN and PETN + polymer samples

Sample	H_{50} / cm
PETN	$17.2 + / - 3.6$
PETN + Kel-F 800	$10.8 + / - 0.6$
PETN + PTFE	$9.5 + / - 1.4$

3.3 Impact on PE, PU and Viton

Polyethylene (PE), polyurethane (PU) and Viton A are all binder materials, and it is interesting to know how they behave during impact.

Fig. 19 shows a sequence taken with the apparatus illustrated in fig. 1. The field of view is 20 mm and the polymeric discs were initially 4 mm diameter and 1 mm thick. The PE flows most easily tending to engulf the other binders. This is most likely due to melting since a spray of

droplets was found on the anvils afterwards. Melting appears to occur between frames 1 and 2 when the sample becomes more transparent. The behaviour of the other two materials reflects their static properties. PU is highly elastic but eventually fails by fracturing (see fig. 20 which is at a later stage and the weight is rebounding). Viton is also very elastic but shows permanent plastic deformation in addition to numerous holes formed by a ductile process (see the mottled pattern in fig. 20).

The fracture and compaction stages alone were investigated in PBXs containing these binders, the pinch regime being avoided by using a clash ring so that ignition was very unlikely. Three materials were tested representing the three binders and all containing type B HMX (see table 3 in section 3.6(a)). The results are presented as stress-strain curves in fig. 21 at a strain rate of approximately 200 s^{-1} . The difference in stress between the peak at fracture and the subsequent plateau is quite marked in this case since the specimens were 6 mm diameter and 5 mm high. The PE composition in particular is very brittle, supporting a stress of less than 2 MPa during compaction. Evidence from above suggests that this may be due to melting of the binder. The V composition on the other hand can support more than 20 MPa and this is probably due to the maintenance of some continuous structure through the presence of fibrils of polymer.

3.4 Drop-weight impact on PBXs; "local" and "widespread" initiation modes

We first make the point that the mechanical response of a cylinder of PBX depends on its aspect ratio (i.e. height to diameter ratio). Fig. 22 shows the force variation during drop-weight impacts on samples of a mock explosive (i.e. inert crystals) having different aspect ratios. The first specimen was 6 mm in diameter and 2.5 mm high and shows two peaks in the force. This can be interpreted in accord with the three stage model of compression such that the first peak corresponds to fracture, this is followed by a lower stress during compaction and finally the second peak corresponds to pinch. This experiment was not carried out with high explosive since a sample of 60 mg or more is required which could cause severe damage to the apparatus. However, evidence from other experiments confirms that the same qualitative behaviour is equally characteristic of the PBXs. The second specimen was also 6 mm in diameter but only 1.5 mm high and with this flat aspect ratio the compaction phase is obscured so that fracture is only noticeable as an inflexion in the leading edge of the main peak.

When flat specimens (4 mm diameter by 1 mm thickness) of PBXs are used in the drop-weight apparatus the force-time records are shown in fig. 23; these are all PE binder/HMX explosive compositions. Similar behaviour occurs with other PBXs. Also shown in fig. 23 are the records of ionisation current which is one of our techniques for detecting ignition (another is light output). The sensitivity of the recorder is set to capture the full stress reached during pinch ($\sim 500 \text{ MPa}$) so that the fracture and compaction stages are very insignificant. During pinch the explosive layer is only about 0.1 mm thick and the underlying response of the machine, which is a half sine pulse, is still clearly distinguishable. The main features contributed by the explosive are the very marked stress fluctuations which were also seen by Heavens and Field [2,3] in some materials. Heavens associated them with mechanical failure of the sample but now it is possible to be more explicit and suggest that in PBXs they are associated with the formation of shear bands. It was also observed by Heavens and Field that ignition (the onset of conduction) often corresponded in time to a drop in stress and this is also observed with PBXs in most cases. It is expected that each of the pressure drops would be associated with an increment of rapid flow implying that there are many more such events in the steel apparatus than in the glass apparatus.

A selection of photographic sequences of impacts on PBX compositions are presented in figs. 24-27. A small number of frames have been chosen from each film to illustrate the ignition and burning phases. The progress of radial expansion in the explosives before initiation is illustrated by the plot of radius against time which accompanies each sequence. A feature common to all the compositions which ignited is that they undergo rapid radial flow before ignition. This behaviour is also seen in pure explosives [2-8]. The combination of high velocity and a confining pressure provides favourable conditions for initiation and ignition sites are often seen midway

between the centre and edge of the sample.

Two distinctive forms of ignition are evident in the sequences. The first is illustrated in figs. 24 and 25 which show initiation occurring at well-defined localities. The ignition area typically has the appearance of a pattern of cracks in the material which also play a role in the propagation stage. They extend into the sample and permit convective heat transfer into the bulk which enhances the burning rate. The second form of ignition, of which figs. 26 and 27 are examples, occurs at a multitude of sites scattered over a wide area. These sites burn out towards their nearest neighbours, first dividing the sample into numerous small particles which are then consumed. Usually, part of the sample shows no ignition sites and this part burns slowly from the outside often leaving a small residue.

These two forms of ignition we refer to as "local" and "widespread" respectively. Some sequences may be difficult to classify immediately into one category or the other but the broad distinction is a useful one. The type of ignition correlates very closely with the amount of damage found on the glass anvils after the event (see also section 3.6). Where damage occurs, the glass surface is divided into a fine mosaic pattern on the scale of 100 μm . In the most severe cases mosaic elements, with a thickness of only a few microns, detach themselves from the surface and their edges curl upwards. The curvature is in the opposite sense to that expected from relief of the compressive stresses in the surface produced in the toughening process. It is therefore likely that the surface is annealed by the heat of explosion and the curling is produced by quenching of the surface layer by the glass bulk. The presence of glass fragments on the surface clearly has implications for secondary initiation by high melting point grits. However, the fact that the majority of fragments remain partially attached to the surface suggests that they are only formed after the scouring action of the explosion has passed. The correlation which is observed is that "local" ignition produces extensive damage over a radius of approximately 10 mm. Widespread ignition, on the other hand, produces no damage except near the residual explosive particles where, before it extinguishes, burning closely resembles the type seen generally after local ignition.

Another step in the understanding of impact ignition is to look more closely at the change of radius with time. The feature of rapid radial flow has already been mentioned as a necessary precursor to explosion. It may also be observed that in some cases ignition occurs during rapid flow but in others there can be considerable delay up to 100 μs . Rapid flow is quite a dramatic effect particularly as it often follows a period in which flow is very slow or zero. The presence of rapid flow is not in itself an unexpected phenomenon as was discussed earlier (see fig. 2). In fact, if the records of radial expansion are compared with the ideal case of fig. 2 the surprising feature is not the rapid flow but the plateau in which no flow occurs (see figs. 26 and 27). Prior to these plateaux the radial expansion usually follows fig. 2 very closely. This feature has been observed before by Heavens and Field [2,3] and Krishna Mohan and Field [7] when using this apparatus but it was not discussed. Given the abrupt way in which the ideal expansion stops there is a strong indication of some kind of mechanical interference in the apparatus.

In discussing the radial flow of liquid explosives Heavens made calculations of the elastic distortions expected in the anvils and came to the conclusion that at a pressure of 100 MPa the maximum depression in each anvil would be 5 μm . However, he modelled an anvil as a semi-infinite solid. An improved calculation implies that if a specimen is deformed to a mean thickness of 160 μm , the depth of indentation is sufficient to allow the anvils to make contact at the rim if the pressure is 800 MPa. This figure is of the order generated in the instrumented drop-weight (see next section) and since the glass apparatus uses a heavier weight, higher drop height, and the calculation did not take account of bending of the finite anvil discs, it seems almost certain that the plateau observed are caused by contact of the anvils.

On the basis of this hypothesis the sequence of events occurring during an impact can be described. In the early stages of impact, lasting approximately 170 μs , the sample is compressed at constant volume and causes negligible retardation of the falling weight. During this time the anvils become indented so that compression takes place, not only with frictional constraint at the interfaces but with material flowing into a radially converging channel. The result of this is that the stress

state in the sample has a very large hydrostatic component. In some cases, ignition occurs during this loading. However, if the sample survives this stage the indentation becomes deep enough to allow the anvils to make contact around the periphery and subsequent increases in load are borne, almost entirely, by this annulus of contact. The sample is trapped in the resulting cavity in a state of equilibrium and since the system has become very stiff due to the annular contact, displacements are very small and the equilibrium can be maintained until the weight rebounds. During rebound the indentation relaxes and the radial constraint due to the shaped cavity progressively retreats. The sample can no longer support the stress as it changes from hydrostatic towards uniaxial and the radial flow starts again. The flow velocity can potentially be very large since it can be driven by the elastic stored energy in the anvils! In the extreme case, if the strength of the material spontaneously vanishes (due to removal of constraint or the onset of slip) the anvils can relax in $4 \mu\text{s}$ which would not be observable with a $7 \mu\text{s}$ framing interval. The resulting approach velocity of the anvils would be 40 m s^{-1} or ten times the original impact velocity!

Comparison of this sequence of events with the radius-time plots suggests that the weight is brought to rest approximately $250 \mu\text{s}$ after initial contact with the sample. This is similar to the time measured on the instrumented drop hammer. "Local" ignition is favoured by the confinement of deeply indented anvils so that it can occur during the loading phase. The appearance of ignition is shown particularly well in fig. 24. Light first becomes visible in frame 3 as a series of pinpoints which grow into fissures in frame 4. The impression is one of initiation occurring in the bulk and becoming visible when burning reaches the surface in frame 3. In frames 4 and 5 fracture is caused by internal pressure from the reaction products and the confinement of this hot gas encourages rapid burning. Energy is generated quickly and the intensity of reaction is reflected in the damage caused to the anvils. Since the sample is trapped by the anvils at the time of initiation, the rapid flow which commences in frame 2 is probably caused by slip in the material which would be consistent with initiation in the bulk by localised adiabatic shear.

"Widespread" initiation occurs during unloading when the stress distribution on the sample is changing dramatically. The hydrostatic pressure maintained during the trapped stage is relieved progressively, starting at the edge of the sample and moving inwards towards the centre. A schematic diagram of this situation is shown in fig. 4(d) where rigid cones, analogous to those of the Prandtl slip line field, are shown in the central region.

The changing geometry and release of elastic stored energy in the anvils encourage rapid flow seen in frame 3 of sequence C (fig. 26). At this point widespread ignition occurs and by frame 4 a very large proportion of the area of the sample is emitting light. Note that the centre of the sample remains dark, corresponding to the rigid region. The clarity with which ignition is seen suggests that it is occurring at the explosive-glass interface and therefore that initiation is aided by friction. During burning, in contrast to the trapped case, the confinement is being removed and the interface provides a direct route for reaction products to escape easily. The intensity of reaction is therefore low and there is little damage to the anvils. When the pressure is released (frame 5) each ignition site has consumed material in its immediate vicinity leaving an open structure of more or less isolated grains (frame 6). Subsequently these grains are largely consumed (save for the largest fragment) but over a long period of about $100 \mu\text{s}$. The amount of material consumed by widespread and by local initiation is therefore similar but reaction is much faster after local ignition.

Fig. 28 shows a sample of a PE/HMX composition, taken with normal illumination, after it was impacted in the glass apparatus but failed to ignite. The extreme edge of the material ($100 \mu\text{m}$) has the appearance of a lightly compacted powder consistent with the existence of a peripheral brittle region (see region II, fig. 4(b)). Inside this is an annulus about 3 mm wide which has a predominantly glassy appearance. In the photograph there is a light region which is extremely smooth and gives a strong indication of melting (the binder is PE with a distinct, low melting point). The remainder of the annulus also shows evidence of melting but has a textured surface with radial flow markings. Under some lighting the central region is indistinguishable from the annulus but the photograph clearly shows that there are a number of distinctive, linear, surface features. These are shear bands, and again under the microscope one can see evidence of melting. The presence of shear bands has been discussed by Field et al [6,9] and the temperature rise

associated with them has been detected by using a heat sensitive film.

3.5 Drop-weight impact on PETN; further evidence for ignition by adiabatic shear

Drop-weight impact, using the transparent anvil and instrumented apparatus (figs. 1 and 3), was first used by Heavens and Field in the early 1970's [2,3]. They showed that thin layers exhibited fracture, compaction, sintering, plastic flow at high velocities, jetting, melting, and ignition in the glass anvil apparatus. Banded structures which became visible in some sequences, with both PETN and RDX, were interpreted, we now think wrongly, as ripples caused by jetting. The evidence on this point was reinterpreted by Field et al [6] and evidence was presented to show that the features were shear bands, a mechanism for hot-spot production and ignition which has been suggested by Winter and Field for other explosives in 1975 [33]. Recent work, using a range of drop-heights, has obtained more support for shear banding and its role in ignition and propagation.

Fig. 29 is for a 25 mg sample of PETN impacted from 1.3 m. At first the sample appears dark since it is viewed in silhouette. In frames 1 to 3 the bulk flow is at a low velocity of ca. 10 m s^{-1} though in frame 3 a small amount of material is ejected as high-speed jets. In frame 3 onwards, families of shear bands become visible. The transparency is associated with sintering and fusion of the sample [2,3]. Rapid bulk flow commences in frame 4, at a velocity ca. 125 m s^{-1} , and ignition in frame 7. Note that the ignition and initial directions of propagation are controlled by the shear bands. Fig. 30 is also for a 25 mg sample of PETN impacted from 1.3 m. Several shear bands (mainly vertical as printed here) are visible of which two associated with the ignition are arrowed. Again the initial reaction is along the shear bands as would be expected since they are at a higher temperature.

Fig. 31 shows the result of an experiment when the heat sensitive film was used. The original is in colour but the black and white reproduction shows the key features. Where there has been fast reaction the products have removed much of the heat-sensitive layer, but at the top of the picture where the film remains it is a deep orange-brown. In the lower part of the film there is a great arc of banding and where the heat sensitive layer remains attached it is various stages of light brown to almost black, all indicative of high temperatures. The ignition also clearly starts from the region where the bands are located. Fig. 32 shows an impact from a sub-critical height onto a PETN layer. It shows the families of shear bands particularly well.

3.6 Drop-weight impact on HMX

Experiments on the effect of particle size on the behaviour of HMX are in progress and a selection of results are reported in this section. The HMX was provided by AWRE and table 3 gives details.

(a) Experiments with heat-sensitive film

The HMX samples were impacted using 12 mm discs of type 570 3M HSF (heat-sensitive film) on the lower roller of the steel anvil apparatus, with the emulsion side of the film against the explosive. A range of drop-heights were used and the H_{50} s determined for the HMX samples in the presence of HSF. These H_{50} s were in fact higher than the H_{50} s with bare anvils. This desensitising effect of the HSF is thought to be due to the increased friction which decreases the velocity and extent of rapid flow.

Fig. 33 shows two HSF discs viewed in silhouette, and also the extent of flow of the HMX (dashed line). The HMX sample originally occupied an area similar to that of the discoloured region. The extent of radial flow of the sample with HSF was less than when bare metal anvils were used. Presumably this was due to increased friction between the explosive and the HSF. The band-like character of the heat output during the impact experiment is evident in fig. 33(a) and can still be detected in fig. 33(b), even though partial ignition and propagation of the explosive had occurred.

Table 3

Type	Comments	Particle size range / μm	Median particle size / μm
A	Granular powder produced by recrystallisation from cyclohexanol.	100 to 1000	480
B	Fine powder produced by colloid milling of type A. Bimodal distribution.	2 to 130	28.5
TC/14	Micronised by fluid energy milling of type A.	2 to 180	20
TC/13		2 to 36	10
TC/12		2 to 29	6.4

Figs. 34-36 are photographs of some of the HSF discs in reflected light and show that the lines observed in transmitted light are not necessarily due to discolouration of the HSF but may be the result of failure or "scoring" of the HSF. Note, the original photographs were in colour! The patterns on the recovered HSF discs consist of families of approximately parallel lines, some of which bifurcate, and which are characteristic of shear bands. The area near the brown line (A) in fig. 34 shows no evidence of film failure. The broader "lines" have brown edges, and where they are broadest a black discolouration (B) of the films occurs. This is due to intense localized heating and to discolouration caused by reaction products emanating from the shear bands in the HMX. Fig. 35 shows that black (very hot) areas also occur at the junction of some lines (labelled C). Fig. 36 is an example where some residual HMX remains attached. A failure line can be seen running through the intersection of two shear planes of an HMX crystal (E), and parts of either the disc or HMX have been molten (F). These observations show that where the explosive has undergone shear, scoring of the HSF film has occurred.

Fig. 37 shows failure patterns in HMX which has remained on the steel rollers after impact. Fig. 37(a) shows the HMX after a test with HSF and shows the close resemblance between lines on the HSF and failure in the explosive. This type of failure pattern was also observed during impact of HMX with bare metal rollers. Three examples are shown in figs. 37(b)-(d). Fig. 37(c) is a clear example of shear bands in an impacted layer of HMX. The conclusion is that HMX fails by shear banding in these experiments and that these shear bands are the hot-spot sites which cause ignition.

(b) Force-time curves

These are not reproduced here since they are essentially similar to those published before [2-9] and illustrated in fig. 23. They showed: (i) pressure drops which we associate with the onset of rapid flow (shear banding); (ii) that this does not necessarily cause ignition (this is consistent with the fact that we can find non-ignited samples with shear bands); (iii) that when ignition takes place it does so after a pressure drop (rapid flow); (iv) ignitions can take place either as the load is increasing or decreasing. As shown below, the photographic evidence provides cases of both and the classification of "local" and "widespread" ignitions are also valid for HMX.

(c) High-speed photography

Heavens and Field [2,3] showed that HMX compacted, jetted, flowed plastically, and ignited, but unlike PETN and RDX did not sinter and melt. Although the propagation rate in HMX was high, combustion was invariably incomplete in the drop-weight experiments. This type of behaviour was found in the present work, with the residue varying considerably. All the experiments were from a 1 m drop-height onto 25 mg powdered layers.

Fig. 38 is for type A HMX and is typical of all impacts on this coarse material (table 3) where ignition took place. The small, slight, darker region which is just visible near the centre in most of the frames is due to overwriting as the camera mirror comes into position again and can be ignored. All the stages listed above are clearly shown. Ignition occurred on rebound after a short plateau region and it is a perfect example of "widespread" ignition from a multitude of sites.

The finer grain samples all exhibited "local" ignitions. Fig. 39 is an example for TC/12 HMX (table 3) where it took place during the initial rapid flow stage. The initial propagation in frame 42 is very similar to the patterns found on the heat-sensitive film (figs. 34-36).

Fig. 40 is for type B HMX (table 3) and is included because it contains some interesting extra features. Local ignition occurs during the rapid flow stage at a group of small sites (three white dots) in frame 48. But these fade and extinguish (frames 48-54). Local ignition at a new site eventually takes over. Enlarged views of frames 48, 49 and 54 are shown in fig. 41. Note that the structure of the main hot spot is reminiscent of the patterns on the HSF (figs. 34-36). Finally, the banded structure which influences the propagation so strongly in frame 57 also suggests the presence of shear bands in the deforming HMX.

(d) Explosiveness, propagation; dependence on particle size

Damage to the surface of the glass anvils after impact depended on the particle size of HMX used and only occurred when there was an explosive reaction. The area of damage for coarse HMX was larger than fine HMX, although there was overlap. Fig. 42 shows damage to four anvils. Fig. 42(a) shows the extent of damage with fine HMX when all the material reacted and for comparison, fig. 42(c) shows damage caused by coarse HMX. Although the amount of residue after an ignition varied widely, the specimens of fine HMX left residue more frequently. Fig. 42(b) shows an anvil after partial reaction of fine HMX. The area of damage is arrowed. Fig. 42(d) shows the extent of anvil damage after partial reaction of coarse HMX. The area affected is similar to a full reaction with fine HMX.

When the damaged surface was viewed from a radial direction, fine fibres were seen to protrude from the surface. An SEM was used to examine the surface. Fig. 43(a) shows that the failure of the glass (after full reaction of fine HMX) occurs in a "flower pattern" similar to that reported by Field and Zafar [34] after irradiation of glass with a laser. Fig. 43(b) shows an example of the more severe "flaking" damage which occurs after full reaction of coarse HMX. This type of flaking damage was also observed in glass by Field and Zafar, and in other brittle materials by Bastow et al. [35]. The larger strips are about 50 μm wide, about 1 mm long, and curl away from the surface. Since glass particles are known to sensitise explosives it is important to know when fracture of the glass occurred. Field and Zafar showed that the mode of failure in glass after irradiation with laser depended on the thickness of any surface film and on the energy density of the laser. A "flower pattern" failure occurred at a lower energy density than did flaking damage. The anvils used in the impact experiments with HMX were of toughened glass, which is about five times stronger than plate glass, and is produced by a heat treatment process which puts the outer layer in compression and leaves the inner layer in tension. If a crack grows completely through the outer compression layer, fracture will propagate. Field and Zafar explained that fracture occurred when a thin surface layer was left in a state of tension. This occurred as a result of viscoelastic expansion of the outer surface layer of the glass when it was heated and which was then unable to relax completely on cooling. High-speed photography was used to show that flaking of the glass occurred during cooling, typically 10 ms after the lifetime of the laser pulse. It can, therefore, be

assumed that glass fracture has no influence on the results of the impact experiments with explosives except to indicate the violence of reaction ("witness block"). The area of damage on the anvils is assumed to be the area which was heated to, or near, the softening point of glass (typically 800°C) and the extent of microfracture is taken to indicate the level of tension in the layer on cooling. It is a useful guide to what is often called the "explosiveness" of an event. Note that the greatest damage occurred with the coarser HMX.

The high-speed photographic records also showed that the propagation of reaction was higher in coarser material. This fits in with LABSET data (the AWRE test for "explosiveness") on the PBXs that we have tested. The LABSET figure is usually higher if it contains coarser material compared to micronised crystals.

Cross-sections of impacted layers which did not ignite show a denser compacted material with fine powders and an open structure with coarser material. The burning front clearly propagates more readily through a compacted layer of coarser material. See, for example, fig. 38 with its "widespread" ignition and propagation. For finer material (see, for example, figs. 39 and 40) there is propagation from "local" sites along a few channels. A second factor which assists more rapid propagation through a compacted layer with larger particles is the higher heat conduction. The more frequent grain boundaries with compacted fine-grain crystals lowers the bulk conductivity. We have measured the thermal conductivity of pressed powdered layers; the value for coarse HMX was twice that of pressed micronised HMX.

3.7 Hot-spot mechanisms during drop-weight impact

These have been discussed in earlier reports and, in particular, in [6]. A few points are worth emphasis:

- (a) The thermal energy required to produce the required hot spot frequently comes from different mechanisms acting additively. Adiabatic shear can be important but it is **not** the only mechanism.
- (b) Liquid explosives such as nitroglycerine (NG) are very susceptible to the adiabatic compression of gas spheres.
- (c) The fact that PETN and RDX can melt during impact, can seal in gas spaces and affect their ignition.
- (d) Adiabatic shear banding has been observed by us in many explosives, and sufficiently high temperatures recorded in them to explain ignition (temperatures recording using a heat-sensitive film technique). A considerable amount of new evidence is given in this report.
- (e) The addition of hard, high melting point grits, sensitised by a friction mechanism [36,37]. Some polymers can also sensitise despite having low melting or softening points [4-6]. This occurs with polymers such as polycarbonate (PC), polysulphone (PS), PTFE, or PMMA which fail catastrophically by fracture or shear (rather than by bulk flow, as would a polymer like polypropylene (PP)). The hot spots are associated with the crack tips or with the shear bands.
- (f) The hot spot at a crack tip in an explosive crystal is **not** sufficient to cause ignition. This is because the fracture surface energy of most explosives is rather low, of order a few tens of mJ's [50], rather than a few 100 J's as with the polymers which sensitise. Recently we have shown [7] that the higher the yield stress of a pure explosive, the higher its plastic flow velocity in the drop-weight test. Thus although with a strong sample the onset of irreversible deformation is delayed, it eventually develops more rapidly when stored energy is released. This means that the likelihood of ignition during the conversion of mechanical energy is greater and explains why a relatively soft, low melting point explosive such as trinitrotoluene (TNT) does not ignite so readily in the drop-weight test.
- (g) During drop-weight impact the anvil deformation has to be considered. Ignition can occur during loading and during unloading. It is useful to consider two types of ignition, "local" and "widespread".
- (h) In several cases that we have considered "widespread" ignition and rapid propagation giving a greater "explosiveness" occurs with larger grain material.

- (i) Hot spots do not only form at the periphery as suggested by Coffey et al. [27,38]. The photographic sequences show that this is clearly not the case. The central region, however, is less likely for the reasons discussed in section 2.3.

4. LASER SPECKLE AND MOIRE PHOTOGRAPHY: APPLICATION TO STRENGTH MEASUREMENT AND CRACK PROPAGATION

4.1 Introduction

Over the years, many ways have been developed to measure the stress distribution in a material or an engineering component. A list of the more important would include photoelasticity, caustics, holographic interferometry, moiré photography and speckle photography. Each technique has its advantages and drawbacks: the use of photoelasticity, for example, is relatively straightforward and easily extended to the study of dynamic events, but is restricted to a few transparent materials which exhibit the photoelastic effect. Laser speckle is a non-contacting method for obtaining whole-field in-plane displacement information, from which the in-plane strain field may be calculated. It is relatively straightforward to use, but analysis of the speckle photographs can be time-consuming. An automatic image processing system has been built at the Cavendish to overcome this disadvantage, and its use in solving practical problems is illustrated in this report.

The first example concerns strength measurement of plastic bonded explosives (PBXs) using the Brazilian test (disc under diametral compression). From the safety viewpoint, only small specimens can be tested and the sensitivity of the laser speckle method is therefore an important consideration. The displacements of typically only a few μm are too small to be accurately measured by moiré photography, for example. Attachment of a moiré grating to the specimen surface also poses problems in this case because the adhesive may attack the polymer binder, and the grating may significantly reinforce a low-modulus material. The use of strain gauges also suffers from these last two disadvantages.

Two further examples illustrate some applications of laser speckle in the field of experimental fracture mechanics, both quasi-static and dynamic.

A high resolution moiré technique (spatial frequency of specimen grating = $150 / \text{mm}^{-1}$) has been developed for measuring dynamic displacement fields. This is illustrated in the final section by high speed photographic sequences showing the propagation of stress waves in plates of polymethylmethacrylate (PMMA) caused by solid particle impact.

4.2 Laser speckle photography

The conventional double exposure laser speckle technique was first proposed by Burch and Tokarski at the National Physical Laboratory.³⁹ The specimen to be deformed is photographed by the light of a laser beam. The film is exposed twice: once before, and once after the deformation. Light is scattered from surface features of the specimen to create a fine random speckle pattern in the image plane. The speckles move with the scattering surface, so that when the film is developed, the image is found to be covered, in effect, by a random array of speckle pairs. The in-plane displacement vector of any point on the specimen can be obtained by measuring the speckle displacement vector at the corresponding point on the film. This is normally done by probing the photograph with a narrow laser beam. A diffraction pattern is formed which is similar to that from a mask containing two small apertures, and is therefore commonly called the "Young's fringes" pattern. The displacement vector can be deduced from the spacing and angle of the Young's fringes. The laser beam is then moved to another region of the photograph and the fringe pattern measured in the same way; this process is repeated until the complete 2-D displacement field has been mapped out. A single photograph might require upwards of several hundred such measurements, and the procedure becomes impractical when performed manually. For this reason, we have built an image processing system²⁶ and developed fringe analysis algorithms^{26,40-42} which allow the analysis to proceed completely automatically. The image processing system consists of a linear photodiode array interfaced to a microcomputer. The speckle photograph is mounted on a stepper-motor-driven X-Y translation

stage so that the computer can digitise the fringe pattern from any point on the photograph. Fourier or Walsh spectral analysis is then used to process the image. With good quality fringe patterns, the system measures the speckle displacement to an accuracy of better than 50 nm. Acquisition and analysis of the fringe pattern, and translation of the photograph to the next point of interest, takes under 10 s; measurement of the displacement field from one photograph on a typical mesh of 16x16 datapoints therefore requires around 40 minutes.

4.3 Strength measurement of PBXs using the Brazilian test

In the Brazilian test, the specimen is in the form of a disc and undergoes diametral compression between two anvils (see section 2.5). The results of experiments on two contrasting PBX compositions are presented here. Further results are described in Section 5.

Composition A contains micronised HMX and polyurethane (96.0:4.0 by volume); composition I contains micronised HMX and Viton A (96.0:4.0 by volume). Each specimen was a disc of diameter 10 mm and thickness 4 mm. A sequence of several double exposure speckle photographs was recorded during each experiment, with the strain increment between exposures sufficiently small for good Young's fringes to be produced from each photograph. The total strain field is then the sum of contributions from each photograph. The first two photographs from each composition were analysed on the image processing system over a grid of 17x17 datapoints. The region covered is indicated by the larger square in Fig. 44(a). The smaller square represents the region (13x13 datapoints) over which the strain field could be accurately evaluated. The strains are calculated from the displacements by numerical differentiation; the algorithm used here is described in ref. 44.

The measured displacement fields from the two photographs of composition I are shown in Figs. 45 and 46. The vector format used in 45(a) and 46(a) is perhaps the easiest to interpret. It should be remembered that the upper anvil moved downwards while the lower anvil remained fixed, so that all the displacements have a rigid body component in the -y direction. An equivalent representation is provided by contour maps of the two displacement components (parts (b) and (c) of Figs. 45 and 46). The contours are entirely analogous to the u- and v-field moiré fringe patterns. The sensitivity, however, is far superior: the contour spacing of 0.5 μm should be compared with a moiré fringe order representing a displacement of typically 25 μm or more.

The displacement field from the second photograph of composition I (Fig. 46) shows that the disc has started to fail. If a horizontal line is followed in the lower half of Fig. 46(a), it can be seen that the vectors suddenly change direction when the vertical diameter is crossed. The sudden change indicates a discontinuity in the x displacement component, u_x , which is also revealed in the contour map shown in Fig. 46(b). The failure of the disc between the two exposures means that the results from this experiment cannot be used to calculate a strain to failure. They do, however, demonstrate one of the potential hazards of a pointwise technique, such as the use of a strain gauge, in an application of this sort. A single strain gauge at the centre of the disc cannot locate the position or time of initiation of a failure zone. The estimate of the strain to failure could then be over-optimistic.

Contour maps of the strains ϵ_{xx} and ϵ_{yy} are shown in Fig. 47 (composition I) and Fig. 48 (composition A). These were calculated from the measured displacement components u_x and u_y by the equations:

$$\begin{aligned}\epsilon_{xx} &= \partial u_x / \partial x \\ \epsilon_{yy} &= \partial u_y / \partial y\end{aligned}\tag{6}$$

From the point of view of strain to failure, ϵ_{xx} is the parameter of interest (Fig. 47(a), (c) and Fig. 48(a), (c)). ϵ_{xx} calculated from the second photograph of composition I (Fig. 47(c)) is not a good estimate of the strain field, because of the discontinuities in u_x arising from the failure zone. The data analysis procedure requires a smoothly varying displacement field. The other three maps are believed to be good estimates of the distribution of ϵ_{xx} , because the displacement field is continuous in the other three photographs.

The experimental results agree qualitatively with the theoretical strain distributions shown in Fig. 44(c).⁴³ The curve ϵ_{rx} , which represents ϵ_{xx} along the horizontal diameter, reaches a maximum at the centre of the disc. $\epsilon_{\theta y}$ is identical to ϵ_{xx} along the vertical diameter, but on this line ϵ_{xx} has a local minimum at the centre of the disc. Thus the tensile strain field predicted by linear elasticity theory is essentially saddle-shaped. This feature is clearly visible on the experimental maps of ϵ_{xx} (Fig. 47(a), 48(a),(c)).

At the centre of the disc, the calculated ($\epsilon_{xx}, \epsilon_{yy}$) values, in millistrain, are:

(1.10, -1.72)	composition I	photograph 1
(2.79, -2.37)	composition A	photograph 1
(3.65, -2.06)	composition A	photograph 2
(3.96, -1.41)	composition A	photograph 3

The ratio of ϵ_{yy} to ϵ_{xx} for composition I is similar to that predicted by theory (compare $\epsilon_{\theta x}$ and ϵ_{rx} at $x=0$, Fig. 44(c)). This ratio is markedly different in the case of composition A, where the non-linear behaviour of the material becomes increasingly apparent with increasing load (photograph 3 was recorded at the highest load levels). The total tensile strain at the centre of the disc up to the second exposure of the third photograph is 1.04%. The disc failed while the fourth photograph was being recorded. 1.04% therefore represents a lower-bound estimate of the strain to failure of composition A. It may be compared with values of 0.91% and 0.99% for two samples of the same composition, measured by manual analysis of speckle photographs along the horizontal diameter.⁴⁵

As mentioned earlier, the specimen of composition I failed between the two exposures of the second photograph, so that an accurate strain to failure cannot be deduced from this one experiment. The image processing system is now used routinely in the course of research on PBXs. With the speed of analysis provided by the system, many more double exposure photographs (typically 5-10) are now recorded as the specimen is loaded, with smaller strain increments between the exposures, so that the strain to failure can be determined much more precisely. Further results are described in Section 5.

4.4 Measurement of quasi-static displacement field around a crack tip⁴⁶

The two standard stress analysis techniques used at present in fracture studies are photoelasticity and the method of caustics. The former requires a transparent material exhibiting the photoelastic effect, while the latter can be used with opaque materials only if the surface has a mirror finish. Laser speckle, on the other hand, is a viable technique with any material, transparent or opaque, which has an optically rough surface.

Experiments have been carried out on single edge notch (SEN) specimens of PMMA ('Perspex'). The specimen dimensions were 300x75x6 mm³. A sharp crack was introduced into one long edge of each sample by means of a razor blade, followed by loading on a Hounsfield tensometer to induce slow crack growth. A suitable surface finish was created by rubbing with fine carborundrum grit, and evaporating a thin layer of aluminium. Before recording the speckle photographs, the specimens were given a small pre-load to ensure that the crack was fully open. The first exposure was made, a further load applied, and the film exposed a second time.

The displacement field from one of the photographs, measured over an area of 16x16 datapoints by the image processing system, is shown in Fig. 49(a). Figure 49(b) shows the crack orientation and coordinate system. Each of the vectors drawn on Fig. 49(a) represents the results of analysing one Young's fringe pattern. Material which was positioned at one of the dots at the time of the first exposure had moved to the end of the line connected to the dot by the time the second exposure was recorded. The displacements have been scaled up 15 times relative to the specimen coordinate system for clarity. Rigid body movement is clearly present: the contribution to u_y is due to one end of the specimen being pulled while the other remained fixed; the u_x

component arises from the basic asymmetry of the SEN specimen geometry about the specimen centreline. Nevertheless, the presence of the crack is clear from the discontinuity in displacement magnitude and angle across the crack line. Contour maps of the two displacement components are shown in Figs. 49 (c) and (d); the contour spacing is 1 μm .

The most important fracture mechanics parameter is the mode I stress intensity factor, K_I , which is essentially the size of the singularity in the stress field at the crack tip. When K_I reaches K_{Ic} (a material property), the crack will propagate, causing failure of the specimen. Slow crack growth can occur in many materials with K_I below K_{Ic} , and at a rate dependent on K_I .

K_I was calculated from the measured displacement fields in two different ways: least squares fitting of the theoretical displacement field; and numerical evaluation of the J-integral.⁴⁷ The details of the algorithms are described elsewhere.⁴⁸ Young's modulus and Poisson's ratio were taken to be 3.31 GPa and 0.35, respectively. The results of the analysis of six photographs are shown in Table 4.

Table 4

Results of the analysis of six speckle photographs. K_I^{ls} and K_I^J are the stress intensity factors calculated by the least-squares and J-integral methods respectively. K_I^{sa} is the value predicted by stress analysis from the applied load. Units are MPa $\text{m}^{1/2}$. Uncertainty in last significant figure is shown in parentheses.

Photo	K_I^{ls}	K_I^J	K_I^{sa}	K_I^J/K_I^{ls}
1	0.159(1)	0.155(2)	0.156(7)	0.975
2	0.190(1)	0.187(1)	0.189(10)	0.984
3	0.201(1)	0.192(5)	0.189(10)	0.956
4	0.255(1)	0.246(2)	0.258(10)	0.964
5	0.321(1)	0.313(3)	0.311(12)	0.975
6	0.306(1)	0.293(5)	0.311(12)	0.959

The results from the two methods of data analysis are in reasonable agreement, although the J-integral method produces estimates consistently lower than the least-squares method- by upto 4.4%, with an average discrepancy of 3%. This difference has also been observed in tests on simulated data, and it is thought that the most likely reason for this is small systematic errors produced by the numerical differentiation procedure required in the J-integral calculations. The advantage of the J-integral method is that the crack tip position does not enter the analysis: all that is required is that the crack tip lies within the integration path.

4.5 Measurement of dynamic displacement field around a crack tip

The technique described in the previous section can be extended to study dynamic fracture, if a high speed camera and powerful laser are available. We are currently developing such a system, with a multiply Q-switched ruby laser as the light source. In this section the results of some preliminary experiments are described in which the ruby laser was configured to produce two short (ca. 50 ns) pulses separated by ca. 15 μs . These two pulses recorded one double exposure laser speckle photograph on a stationary high resolution plate.

A ruby laser has a relatively long response time between application of the trigger signal and production of the light pulses (typically 1400 μs), so that the laser must trigger the event rather than the other way round. In these experiments, the specimen (PMMA, dimensions identical to static experiments) was pre-tensioned to about 80% of the failure load, and the crack initiated by means of an explosively-driven chisel at the mouth of the starter notch. The crack velocity was measured by the resistor grid method, in which a set of silver strips is evaporated onto the specimen surface. Each strip is connected across a resistance in a series network (Fig.

50); as the crack grows, the strips rupture sequentially and the resistance of the network rises. This is recorded as a changing voltage (Fig. 51). Fig. 52 shows a transient recorder trace from the network when the crack was initiated by the detonator-driven chisel. The two light pulses from the laser are also recorded so that the crack tip position at the time of each exposure can be determined.

A print from one of the speckle photographs is shown in Fig. 53, together with some fringe patterns from points near the crack. The displacement field, measured from the photograph by the image processing system, is displayed in vector format in Fig. 54. As in the quasi-static case, the stress intensity factor was estimated by a least squares fit of the theoretical displacement field to the measured displacements. The dynamic form of the field equations⁴⁹ was used however: at high crack velocities, the inertia of the material causes significant distortion of the quasi-static displacement field. Dynamic values of the Young's modulus and Poisson's ratio of 5.46 GPa and 0.338, respectively, were used in the calculations. The calculated stress intensity factors were $(2.59 \pm 0.08) \text{ MPa m}^{1/2}$ at the first exposure, and $(2.39 \pm 0.05) \text{ MPa m}^{1/2}$ at the second; the average crack velocity was $287 \pm 8 \text{ m s}^{-1}$ at the time of the two exposures. These K_{Id} values should be compared with the fracture toughness $K_{Ic} = 1.6 \text{ MPa m}^{1/2}$.⁵⁰ Further experiments are planned as part of an investigation into the uniqueness of the stress intensity factor-crack velocity relationship.

4.6 High resolution moiré photography

In experimental mechanics, the moiré technique refers to the superimposition of two line gratings: one attached to the specimen (specimen grating), the other stationary. A fringe pattern is formed which is essentially a contour map of the in-plane displacement component normal to the grating lines, with a contour interval equal to the specimen grating pitch. When both in-plane displacement components are required, a crossed specimen grating is used.

When applying moiré to dynamic events, the usual technique of double exposure followed by optical spatial filtering of the developed film is not appropriate: the limited spatial resolution of most high speed cameras (typically $10\text{--}30 \text{ / mm}^{-1}$) severely limits the sensitivity. However, the optical arrangement shown in Fig. 55 overcomes this problem by imaging the specimen grating onto the reference grating; the camera then records the fringe pattern rather than the grating. The spatial frequency of the specimen and reference gratings used for the fringe patterns shown in Figs. 56-59 was 150 / mm^{-1} , giving a sensitivity of $6.7 \text{ } \mu\text{m fringe}^{-1}$. The objective OL₁ (Olympus f/4 Macro) was masked⁵¹ to enhance the fringe contrast, field coverage, and depth of field.

Figure 56 shows a fringe pattern from an experiment in which a sharp crack in PMMA was loaded quasi-statically under mode I conditions. A crossed grating was used, and a magnification of slightly greater than unity was chosen to produce linear mismatch or "carrier" fringes. The presence of the carrier fringes allows both in-plane displacement components to be extracted from the one photograph, provided the spatial frequency is sufficiently high that the horizontal and vertical fringes do not become parallel at any point.

The image processing system described earlier in the report has been used to analyse such fringe patterns using the Takeda Fourier transform method.⁵² This converts a fringe intensity map into a phase map; the difference between two phase maps of the deformed and undeformed state is then proportional to the appropriate displacement component. The photograph shown in Fig. 56 (together with one of the undeformed specimen) resulted in the two wrapped phase maps shown in Fig. 57, which may be compared directly with the maps of u_x and u_y produced by speckle photography (Fig. 49). In Fig. 57, the phase discontinuities occur at intervals representing a relative displacement equal to the specimen grating pitch, $6.58 \text{ } \mu\text{m}$. From a least squares analysis, the stress intensity factor was calculated to be $0.490 \text{ MPa m}^{1/2}$, which compares well with the value of $0.501 \text{ MPa m}^{1/2}$ deduced from the applied load.

The high resolution technique has been used in studies of the transient displacement field caused by solid and liquid impact. Figures 58 and 59 are sequences showing the u_x and u_y components resulting from a ball impact at 115 m s^{-1} , with an interframe time of $0.95 \text{ } \mu\text{s}$. The mismatch fringes in Fig. 58 are tensile (i.e. SG was imaged onto RG at a magnification slightly

greater than unity) whereas those in Fig. 59 are compressive (magnification slightly less than unity). For example, the bunching of the fringes directly under the ball in Fig. 58 indicates tensile strains parallel to the edge being impacted. The Fourier transform method is at present being extended to calculate the strain field directly.

4.7 Conclusions

It is now nearly two decades since the invention of laser speckle photography. The technique has proved to be attractive as a stress analysis method because of its simplicity and sensitivity. Its widespread adoption has been somewhat inhibited, however, by the time-consuming step of extracting displacement information from the speckle photograph. It has been shown in this report that this need no longer be a drawback of the technique. A relatively inexpensive image processing system is capable of reliable and accurate automatic analysis of speckle photographs. The system has been illustrated by three important practical applications: strain to failure measurement of PBXs, and measurement of quasi-static and dynamic stress intensity factors. It is now hoped to extend the technique by combining the ruby laser with a rotating mirror camera capable of 2.5×10^6 frames s^{-1} .

A high resolution moiré technique has been used to study transient displacement fields caused by solid particle impact. Preliminary results are encouraging; further experiments are planned with opaque materials (metals, ceramics and PBXs) using reflective phase gratings.

5. QUASI-STATIC STRENGTHS AND STRAINS TO FAILURE OF SOME PBX'S

5.1 Introduction

Samples from five different PBX compositions have been supplied by Los Alamos, in the form of discs 6.35 mm in diameter by 2.0 mm thick (see Table 5). These samples were used to measure the quasi-static strengths and strains to failure, at a strain rate of 10^{-4} s^{-1} .

TABLE 5 DETAILS OF PBX COMPOSITIONS

Composition	Constituent	Weight/percent
PBX 9501	HMX	95.0
	ESTANE	2.50
	BDNPA	1.25
	BDNPF	1.25
PBX 9502	TATB	95.0
	KEL F	5.0
PBX 0298	HMX	97.50
	Kraton	1.125
	oil	1.375
PBX 0407	TATB	69.8
	PETN	25.0
	KEL F	5.0
PBX 0344	dye	0.20
	TATB	71.25
	HMX	23.75
	KEL F	5.0

5.2 Experimental

(a) Experimental Measurement of tensile strength

The quasi-static tensile strengths have been measured using the Brazilian test used in previous years, and described in earlier reports and sections 2.5 and 4. The jig used for loading the specimens is the same as before with the exception of the loadcell. This has now been replaced by one which can measure forces up to 100 kgf. The output from the transducer is fed to an operational amplifier which has a gain of 2000 times, giving an output voltage of 1.80 volts at a load of 32 kgf. The analogue output from the amplifier is then input to an A to D converter on a BBC microcomputer which can accept DC voltages up to 1.80 volts. This enables the load verses time history of a sample under test to be stored directly on to a floppy disc; where the data can be easily manipulated and processed. In addition a real time plot of the load or stress-time data can be displayed during the test by means of auto-scaling graphics routines written for the computer.

(b) Measurement of strains

The strains in the samples under test have been measured using Laser Speckle Photography (see Section 4). The experimental set up used for recording speckle patterns has been substantially modified during this report period. Originally speckle patterns were recorded on holographic plates which necessitated the use of a darkened room. This requirement has been overcome, by using the same emulsion (Holotest 10E75) on a 35 mm cassette film, manufactured by AGFA GEVEART.

The ability to house the holographic film in a conventional 35 mm camera (ie in these experiments an Olympus OM2), has two major advantages

- (i) An Olympus OM2 motor drive can be used to rapidly advance successive film frame eliminating the need to interrupt the loading of the sample whilst a new plate was inserted.
- (ii) By using a narrow band-pass filter tuned to the wavelength of a He-Ne gas laser fitted to the speckle patterns can be recorded under ambient lighting conditions.

A 20 mW He-Ne gas laser was used to illuminate the specimen under test, with the beam expanded to just cover the sample. The speckle patterns were recorded with an ANASTIGMAT 4 inch focal length lens at an F number of 2.80. An object to image magnification of 3.15 times was used. With these settings, the smallest speckle size that can be resolved by the recording lens is $2.85 \mu\text{m}$ which defines the smallest displacement which can be measured. Typically exposure times of 1 to 2 s were required for each of the two exposures recorded for each speckle pattern. The maximum displacement of the speckle pattern during each exposure is about 1/2 the diameter of the smallest speckle that can be resolved by the lens. Consequently the speckle patterns could be recorded whilst the sample was being loaded. Recording a double exposure on to a single frame of film using an Olympus OM2 camera in the normal manner, is not practical in the experimental set up being used. To overcome this difficulty, the camera lens has been replaced by an electronic shutter (Melles Griot ILEX electronic shutter) operated by the computer, thereby enabling multiple exposures to be recorded automatically. The camera shutter is opened and closed at the appropriate times by a solenoid, and the film advanced to the next frame by the motor drive; both of which are also controlled by the computer. In order not to interfere with the BASIC data logging program, the operation of the camera etc, is accomplished using the interrupt facilities on the BBC microcomputer.

- (c) Analysis of speckle patterns and calculation of strains

During the loading of a sample typically 4 to 10 speckle patterns were recorded. The interval between double exposures ranged from 20 s to 50 s depending on the material. It is necessary to record multiple speckle patterns otherwise poor visibility fringes would be obtained, due to strain induced decorrelation. The speckle patterns were analysed on an image processing system designed and built by J M Huntley which is described in detail in Section 4 and in ref. 26. This system can measure displacements to an accuracy of $\pm 0.05 \mu\text{m}$ on good visibility fringes. It takes 4 minutes to analyse one fringe pattern with the present system, and so the majority of patterns have been analysed on a 5 by 5 grid positioned at the centre of image of the disc, with a mesh size of 1.0 mm; which corresponds to a spacing of 0.318 mm on the specimen. However one sample from composition PBX 0344 has been analysed on a 15 by 15 grid with a mesh size of 1.0 mm, to enable contour maps of the strain and displacement fields to be obtained. The strains have been calculated by numerically differentiating the displacement field using the technique described in ref. 44. To plot continuous stress strain curves the experimental strain values obtained from the speckle patterns; were fitted using second degree polynomials by the least squares method. An estimated strain was calculated for each stress value recorded, and a stress strain plot generated. For comparison purposes the experimental values are plotted as well.

5.3 Results

The results for the tensile strengths and strains to failure, for the five different compositions studied are presented in tables 6 to 10.

Table 6 - Results for composition PBX-0344.

Sample number	Failure load/kgf	Stress/MPa	Strain/millistrain
1	7.96	3.92	
2	8.70	4.30	
3	7.60	3.70	
4	9.20	4.53	
5	7.91	3.89	
6	7.90	3.90	
7	7.90	3.90	
8	8.37	4.12	
9	9.40	4.63	1.68
10	9.48	4.67	1.72

Mean 8.44
dev ± 0.70

Mean 4.17
dev ± 0.36

Mean 1.70
dev \pm

Table 7 - Results for Composition PBX 0298

Sample number	Failure load/kgf	Stress/MPa	Strain/millistrain
1	1.90	0.93	
2	2.30	1.13	11.20
3	2.20	1.08	
4	2.20	1.08	11.20.

Mean 2.15
dev ± 0.17

Mean 1.06
dev ± 0.09

Mean 11.20
dev \pm

Table 8 - Results for Composition PBX 9501

Sample number	Failure load/kgf	Stress/MPa	Strain/millistrain
1	1.50	0.74	
2	1.73	0.85	
3	1.70	0.84	4.40
4	1.30	0.64	
6	1.70	0.84	3.43

Mean 1.59
dev ± 0.18

Mean 0.78
dev ± 0.09

Mean 3.92
dev \pm

Table 9 - Results for Composition PBX 0407

Sample number	Failure load/kgf	Stress/MPa	Strain/millistrain
1	8.10	3.98	3.07
2	8.30	4.08	
3	8.0	3.93	
4	8.03	3.95	
5	8.38	4.12	
6	9.32	4.54	
7	8.23	4.05	
8	7.41	3.64	2.99
9	8.73	4.29	
10	9.30	4.57	

Mean 8.38
dev ± 0.59

Mean 4.12
dev ± 0.29

Mean 3.03
dev \pm

Table 10 - Results for Composition PBX 9502

Sample number	Failure load/kgf	Stress/MPa	Strain/millistrain
1	6.90	3.39	3.28 2.54
2	6.58	3.24	
3	6.20	3.05	
4	6.30	3.10	
5	6.80	3.34	
6	6.70	3.29	
7	6.50	3.20	

Mean 6.57
dev ± 0.26

Mean 3.23
dev ± 0.12

Mean 2.91
dev \pm

5.4 Discussion

Of the five materials tested compositions PBX 0298 and 9501 showed the lowest tensile strengths, failing at a stress of 1 MPa or less. Both materials behaved in a rather ductile manner as shown in figures 61 and 62. However the strains to failure were very different since PBX 0298 fails at about 1 percent strain, whilst PBX 9501 fails at less than half this value. The remaining three materials PBX 0344, 0407 and 9502; show very similar tensile strengths, particularly 0407 and 0344. The stress-strain and stress-time curves for these materials, given in figures 60, 63 and 64; show a much more brittle behaviour. Although the tensile strengths of 0344 and 0407 are very close, the failure strain of 0344 is significantly smaller than 0407. If the tensile strengths of 0407 and 9502 are compared, together with their compositions; it appears that the replacement of TATB by a TATB/PETN mixture, significantly increases the tensile strength of the composite without affecting its strain to failure. Replacing TATB by a TATB/HMX mixture also increases the tensile strength by a similar amount, although the strain to failure is reduced. This may be due to the HMX component, as this is a weaker and more brittle crystal than PETN; and may be more susceptible to fracture as a result of deformation twinning ref. 53. Unfortunately since neither of

6. MICROSTRUCTURE AND FRACTURE PATHS IN PBX'S

6.1 Introduction

Techniques have recently been developed to study the relationship between the microstructure of two Los Alamos plastic bonded explosives (X-0298 and PBX 9501) and their fracture routes when broken in the Brazilian test under quasi-static conditions. Attempts have also been made to monitor the initiation and growth of fracture in these materials using time-lapse photography.

6.2 Experimental

(a) Polishing and Staining Techniques

Samples from both materials were initially polished on a fine grade wet and dry paper (silicon carbide P600A) to obtain flat surfaces. Further polishing was carried out in an automatic polishing machine using a 2 μm Cerirouge powder (consisting of zirconium oxides) with the sample being lubricated with distilled water. The samples were polished for several hours under a light load of approximately 50 grams. Microscopic examination of the polished surfaces of both materials revealed a smooth but almost opaque surface with few crystals visible at this stage. To the unaided eye however, the surfaces appeared to be very reflective. Further polishing with heavier loads, did not improve the surface finish. It was concluded that the polymer binder had become smeared out over the surface of the sample during the polishing process. Attempts were made to etch away this layer using a variety of solvents. After a process of trial and error, it was found that wiping the polished surface with iso-methyl butyl ketone, immediately followed by washing with distilled water, was very successful both in removing the polymer layer and revealing the underlying microstructure. This technique worked well with both materials although the explanation is not well understood. Microscopic examination of the surfaces after polishing and etching, showed that it was sometimes difficult to discriminate between the binder and the crystals. To overcome this problem, a technique for staining the binders without affecting the crystals⁵⁴, has been used. This required exposing the polished samples to ruthenium tetroxide vapour for several hours in a sealed container. After exposure the binders for both materials were stained black, whereas the HMX crystals remained unaffected. The microstructure could then be observed with considerably improved definition. This was particularly important for the time-lapse photographic studies.

(b) Time-Lapse Photography

A post-failure examination of the fracture route through the microstructure, provided a valuable insight into the fracture mechanisms. It was not, however usually possible to determine where failures initiated, or the order in which events occurred for example, in the case of crack propagation. A technique has therefore been developed using a computer operated camera (Olympus OM2 with motor drive), attached to a microscope stage to record photographic sequences of the microstructure at the centre of a sample during a Brazilian test. Under ideal conditions fracture of the material should start at the center of the disc, but in practice it sometimes started outside the field of view of the microscope. Despite these limitations, results for both X-0298 and PBX 9501 have been obtained and are presented in the results section together with fracture route montages.

6.3 Results

A time-lapse sequence showing the initiation and growth of fracture in a region close to the centre of a sample of X-0298, during loading in the Brazilian test, is shown in figure 67. This sample failed at a load of 1.64 kgf corresponding to a tensile stress at the centre of 1.28 MPa at a time of 167 s. The first frame in the sequence was recorded at 156.15 s, with the subsequent frames being recorded at 8 s intervals, with exposure times of 0.1 s. The sequence shows six frames labelled a) to d). The white arrows in frame b) show two sites where failure has initiated. The lower of the two arrows indicates that a rupture of the binder adjacent to the edge of a crystal has occurred. The fracture site indicated by the top arrow, shows a thin crack in the binder between two HMX crystals. In this case it is difficult to determine if the failure initiated in the binder or one of the crystals. In frame c) the crack has extended vertically through the two large crystals, whereas the rupture at the bottom of the frame has opened up and moved towards the interface of a large crystal above it. It can also be seen that there are two additional cracks, which appear to be ruptures in the binder, to the left and above the same crystal. The left hand crack has caused the debonding of one face of the adjacent crystal. Frame (d) shows these cracks more clearly, but as yet not connected. These cracks extend as they open, eventually linking up to form a continuous fracture, as shown in frames (e) and (f). A post-failure fracture route montage, is shown in figure 68. In the absence of a time-lapse sequence for comparison, it might be assumed that failure initiated in the region where the crack opening is greatest, and resulted from debonding of the large crystal from the binder. Examination of the time-lapse sequence however shows that failure at this site did not occur until a later stage, and that the fracture did not result from the debonding of the large crystal, but from the rupture of the binder and debonding of a small adjacent crystal. The fracture route montage shows examples of crystal fracture, interfacial failure and binder rupture. In this sample there is quite extensive fracture of the larger crystals. A time-lapse sequence showing the failure of a sample of composition of PBX 9501 is shown in figure 69. This material fails in a ductile manner as shown in figure 62, with the load-time curve (i.e. with the load proportional to stress until failure), showing a steady rise, before reaching a peak value at the onset of fracture. This sample attained a maximum load prior to failure of 1.8 kgf, which corresponds to a tensile stress of 0.9 MPa at the centre after a time of 90 s. The first frame in the time-lapse sequence was recorded at a time of 99.76 s with subsequent frames recorded at 4 s intervals, with each frame being exposed for 0.2 s. The two black arrows in frame (a) show the initiation of failure at two sites. The lower arrow, (pointing right) shows the formation of a crack very close to the interface of a large crystal. In subsequent frames, this crack opens up, and propagates along the interface causing debonding of part of the crystal. The crack continues to grow vertically up into the field of view, as shown in frames (c) and (d) resulting in the interfacial failure of two smaller crystals above it. The fracture route montage for this sample, shown in figure 70, does not show the extensive crystal fracture that is apparent in composition X-0298, but shows rather more interfacial failure. In this case the loading of the sample was halted before the cracks and ruptures at different sites had time to link up to form a continuous fracture path. Figure 71 shows a montage of the microstructure through another sample of composition PBX 9501 before and after a Brazilian strength test. In this case the sample failed at a load of 1.14 kgf which corresponds to a tensile stress of 0.61 MPa at the centre. It can be seen from the montage, that interfacial failure has occurred at the sites of two large crystals. The large crystal at the top of the figure appears to have a smaller crystal butted up against it, without a layer of binder between them, which may have contributed to its interfacial failure. Also there are several points between the large crystals where there are unconnected ruptures in the binder. This sample had a low tensile strength of 0.61 MPa when compared with the average value of 0.78 ± 0.09 MPa for other samples. It should be noted, that the sample was deliberately orientated in the loading jig, so that the large crystals were situated in a region of uniform tensile stress. This provided an opportunity to observe the effect of the large crystals on the fracture behaviour.

6.4 Discussion

The time-lapse sequences for X-0298 and PBX 9501 shown in figures 67 and 69, show that fracture initiates at different sites with cracks slowly extending as they open up. If these cracks are allowed to grow they can link up to form a continuous fracture path. The time-lapse sequence for X-0298 suggests that failure can initiate from ruptures of the binder, as well as interfacial failure between the HMX crystals and the binder. In addition there is clear evidence of crack propagation through crystals of HMX. If the critical stress-intensity factor K_{Ic} for a mode I (tensile) failure is known, then the flaw size corresponding to a given fracture stress can be estimated from the Griffith criterion. For this sample, the tensile stress at failure was 1.28 MPa and the mode I stress-intensity factor for HMX is $6.2 \times 10^4 \text{ Nm}^{-3/2}$. The predicted flaw-size, $2c$, is then 1.5 mm. This is clearly much larger than any of the fractured crystals shown in figure 68. The extensive fracture of HMX crystals is a particularly interesting result, as the calculation above implies that the stress is insufficient to cause the fracture of the crystals shown. It is apparent, that the only examples of fractured crystals, are those on the crack path. This suggests that crystals are fractured when they impede the growth of a crack, which cannot easily go around them. Under these conditions, the crystals could be subjected to significantly higher tensile stresses, due to the stress concentration at the tip of the propagating crack. The time-lapse sequence for the PBX 9501 sample also shows two examples where failure appears to have initiated in the binder. The cracks from the sites identified by the black arrows, extend slowly in a vertical direction as they open, and appear to propagate through the binder, and along the crystal/binder interfaces without going through the crystals. Examination of the fracture route montage confirms that there is very little crack propagation through HMX crystals. The montages showing the microstructure of another sample from composition 9501, before and after a Brazilian strength test, also show a similar result. As mentioned in the Results section, this sample was mounted in the loading jig so that the effect of the large crystals on failure could be determined. The sample failed at a significantly lower stress. The fracture route montage shows very clearly that interfacial failure has occurred at the sites of the two large crystals. Theoretical work^{55,56} has shown that the square of the stress required to detach a rigid spherical inclusion from an elastic matrix is inversely proportional to the size of the inclusion. It is suggested that the low stress at which the sample failed, may be due to interfacial failure /debonding at the sites of the large crystals.

OPTICAL AND RAMAN STUDIES OF EXPLOSIVES UNDER VARYING PRESSURE AND TEMPERATURE

C.M. PEREIRA and M.M. CHAUDHRI

Cavendish Laboratory, University of Cambridge, Madingley Road, Cambridge, England

Recent studies of the effect of pressure and temperature on the optical and Raman spectra of the azides of K, Tl, Ag and Pb have been made using a diamond anvil cell, helium cryostat and a furnace. With increasing pressure or decreasing temperature the Raman spectra of KN_3 was found to show stiffening of the lattice modes. TlN_3 , however, showed a pressure induced structural phase transition at 5kbar leading to a doubling in the size of its unit cell. AgN_3 does not show any phase transition at low temperatures although some of its Raman modes are found to soften. Optical measurements on AgN_3 show strong excitonic features on the band edge at low temperatures and with increasing pressure the crystals are found to darken suddenly and irreversibly. This effect is not seen in $\text{B-Pb(N}_3)_2$ where the edge is seen to shift linearly to lower energy with pressure.

1. INTRODUCTION

A study has been made of the optical absorption and Raman phonons in single and polycrystalline samples of potassium, thallium and silver azide. Of interest is why small differences in their crystallographic structures cause large differences in their relative stabilities^{1,2}.

The experiments were performed under conditions of varying pressure and temperature.

2. EXPERIMENTAL PROCEDURE

Optical absorption spectra were measured using a P-E Lambda9 UV-NIR spectrometer. The Raman spectra were obtained on either a Coderg T800 high resolution spectrometer or a Dilor Omar 98 multichannel spectrometer with an Ar^+ laser at 5145Å (above the azides absorption edge). Laser powers of ~3mW were used to avoid sample decomposition and only unpolarised Raman spectra were obtained because of the small sample sizes.

Samples were either mounted in a continuous

flow He cryostat, high temperature furnace or diamond anvil cell.

3. RESULTS AND DISCUSSION

3.1. Optical Absorption

At pressures of about 5 kbar AgN_3 was found to darken irreversibly and transmission measurements could not be obtained. It is suggested that this is due to the decomposition of the samples leading to the precipitation of metallic silver. Also electrical conductivity measurements on powder samples under pressure³ do not show evidence of a phase transition at these pressures.

Figure 1 shows the optical absorption spectra of AgN_3 recorded as a function of temperature. At low temperatures three bands at 3.44, 3.46 and 3.51eV are seen which sharpen and shift to higher energy as the temperature is reduced.

Previously, Deb and Yoffe⁴ had reported two very weak bands at 3.44 and 3.46eV. These were explained, following the initial work of McLaren and Rogers⁵, as Wannier type excitons with $n=3$

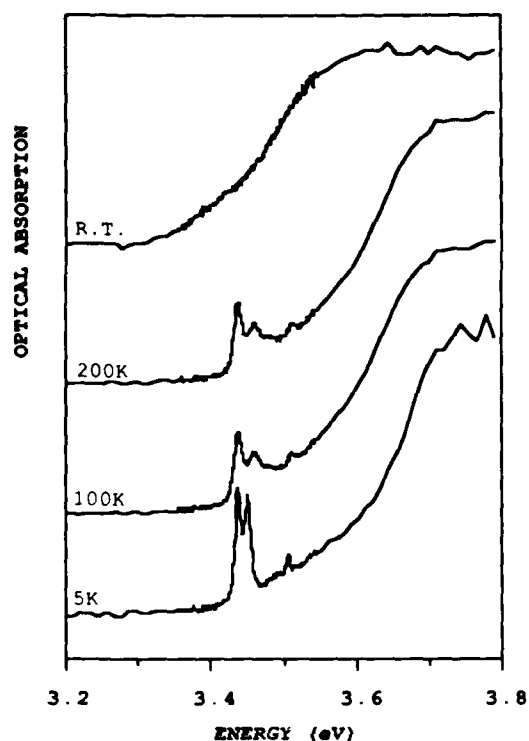


Figure 1: Change in the optical absorption of silver azide with temperature.

and 4. This interpretation has been disputed by Gora et al.⁶ who argued on the absence of $n=1$ and 2 excitons. From our results the measured bands do not fit the $E_n \propto 1/n^2$ relationship for Wannier type excitons and the energies of the bands are also too low to be excited states of the cation or anion⁶. In conclusion, the nature of the exciton bands is still unresolved.

By comparison $\beta\text{-Pb(N}_3)_2$ remains clear under pressure and the band edge is found to shift linearly with pressure with a gradient of $-8.1 \times 10^4 \text{ eV kbar}^{-1}$ and no excitonic features were resolved on the band edge. However on very thin films, a band at 3.3eV which shifts by $4 \times 10^{-3} \text{ eV kbar}^{-1}$ has been reported and this has been attributed to an exciton⁴.

3.2 RAMAN SPECTRA

Unpolarised Raman spectra were obtained from potassium, thallium and silver azide under varying pressure or temperature. With intensities of over 5mW the Raman spectra of both AgN_3 and TlN_3 were found to change as the samples decomposed. As the wavelength of the laser light (514.5nm) was above the crystals absorption band edges (typically $\sim 360\text{nm}$) it is suggested that sample decomposition takes place initially because of absorption by impurities within the crystals.

KN_3 , with one of the simplest azide structures has an tetragonal unit cell (D_{4h}^{1F}). There are 5 Raman active modes in total, 2 internal modes associated with the azide group (A_{1g}, B_{2g}) and 3 external metal-metal (E_{1g}) and azide-azide modes (B_{1g}, E_{2g}). Under increasing temperature, up to the melting point (623 K), or with decreasing pressure the potassium azide phonons behave in an expected way with the modes softening as given in Table 1.

Table 1: Rate of Change in Internal Mode Frequencies in KN_3 with Pressure and Temperature. The E_{1g} mode is a cation lattice mode and the E_{2g} and B_{1g} modes azide libration modes (not resolved with temperature).

Mode	R.T. Freq. cm^{-1}	Temp. Dep cm^{-1}/K	Pressure Dep. $\text{cm}^{-1}/\text{kbar}$
E_{1g}	105.7	-0.014	0.023
E_{2g}	146.5		1.506
B_{1g}	153.1	-0.091	1.441

At R.T. TlN_3 has the crystallographic structure of KN_3 giving a similar Raman

spectrum. Below 240K there is a phase change to lower symmetry with an orthorhombic unit cell (D_{2h}^{20}) which is accompanied with a doubling of the unit cell from two formula units to four⁷.

Correlation between the zone centre phonons in the R.T. and L.T. phases show that the original room temperature phonons are still Raman active in the L.T. phase. This is observed in the Raman spectrum of the external modes, Figure 2, by the splitting of the original room temperature Raman modes. The internal modes, Figure 3, are not greatly affected by the phase change although these also split due to the doubling of the unit cell below the transition temperature. Preliminary Raman studies up to

pressures of 45kbar show a structural phase change at about 5kbar where there appears to be a doubling of the unit cell in the *c* axis similar to that found at L.T. phase.

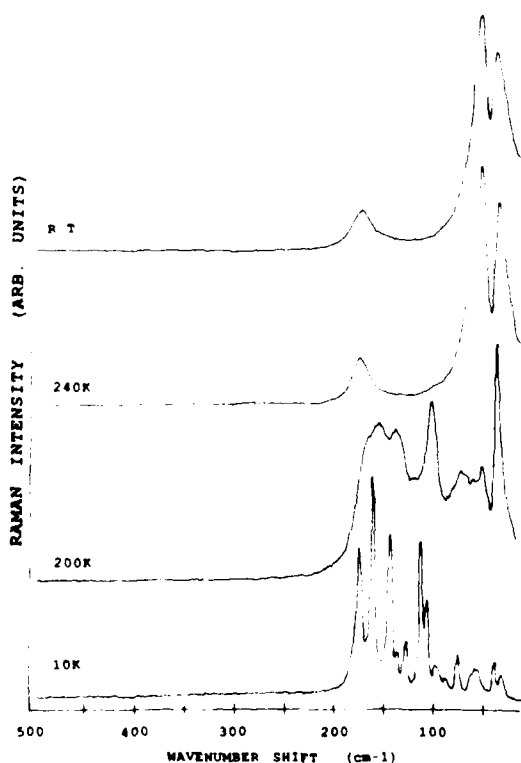


Figure 2: Raman Spectra of internal modes in thallous azide

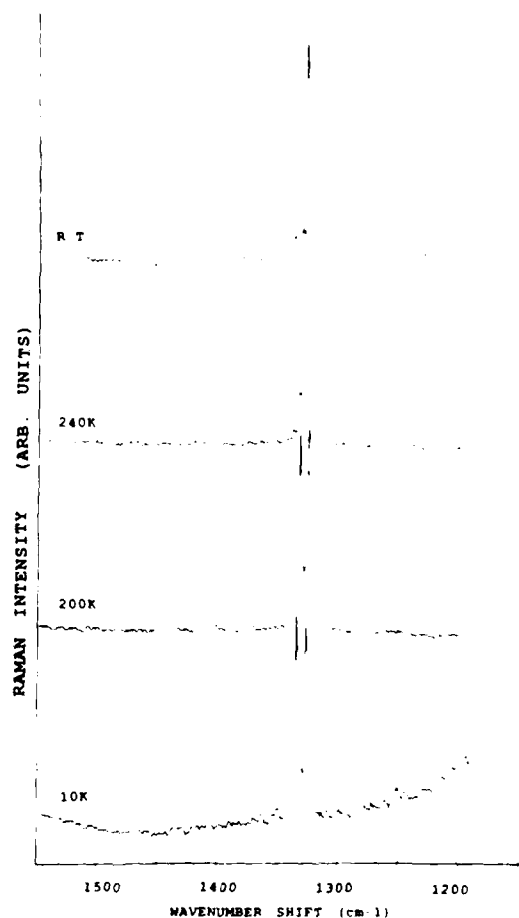


Figure 3: Raman Spectra of external modes in thallous azide

Silver azide is similar crystallographically to KN_3 but because the angles between neighbouring azide ions in the *c* axis are slightly distorted from the KN_3 the lengths of the *a* and *b* axes are different lowering the crystal symmetry is lowered to orthorhombic, D_{2h}^{26} ⁸. This is thought to be due to a degree of

covalent bonding between the metal and azide ions, forming a layer type structure in the *b* direction. Because of this, the doubly degenerate KN_3 modes split, and there are nine Raman active modes; 2 internal (A_g, B_{2g}) and 7 internal ($A_g + 3B_{1g} + B_{2g} + 2B_{3g}$). Seven Raman modes were measured, five external (Figure 4) and two internal. These were assigned by cross-correlation between the AgN_3 and KN_3 zone centre modes and their temperature dispersion measured, Table 2.

Table 2: Frequencies of the Raman active phonons measured in silver azide.

Frequency 70K	R.T.	Temp. Dep $\Delta f/\Delta T (\times 10^{-2})$	Assignment
65	56	-4.7	B_{13g}^1
77.5	76.5	-0.52	B_{12g}^1
149	160	4.1	A_g
209	189.5	-7.3	B_{23g}^2
226	230	2.3	B_{22g}^2
1248	1245 (250K)	-2.352	ν_2 (comb.)
1339	1334	-2.096	A_g

The directions of the shifts of the lattice modes suggest that, somewhat unusually, the crystal lattice tends towards a higher symmetry phase on cooling. Although the azide rocking modes, B_{22g}^2, B_{23g}^2 , (which are derived from the single doubly degenerate E_g mode in the KN_3 structure), tend to converge at low temperature suggesting the formation of a tetragonal potassium azide like lattice, although the A_{1g}^1 mode does not converge to the same frequency. It would appear that on cooling the dominant effect is the anharmonic interaction between the π -orbitals of the stacked azide groups which stop the angle between them in the *b* direction from reducing as the lattice contracts.

ACKNOWLEDGEMENTS

We would like to thank Dr. W.Y. Liang and Dr. A.D. Yoffe for their helpful comments and suggestions and the S.E.R.C., M.O.D. Procurement Executive and U.S. Government for their support.

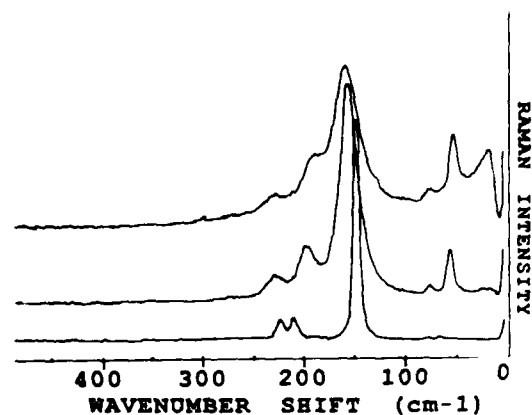


Figure 4: Raman Spectra of the external modes in Thallous Azide

REFERENCES

1. C.B. Colburn, Developments in Inorganic Nitrogen Chemistry, Volume 1 (Elsevier, London, 1966).
2. H.D. Fair and R.F. Walker, Energetic Materials, Volume 1 (Plenum Press, London, 1977).
3. C.S. Rees and M.M. Chaudhri, J. Phys. C, 'in print'.
4. S.K. Debb and A.D. Yoffe, Proc. Royal. Soc. A256 (1960) 514.
5. A.C. McLaren and J.T. Rogers, Proc. Royal. Soc. A240 (1959) 346.
6. T. Gora, D.S. Downs, P.J. Kemmy, and J. Sharma, Electronic Structure of the Azide and Metal Azides, [1].
7. D.V. Alekseev and G.A. Kazunina, Sov. Phys. Solid State 27 (1985) 19.

REFERENCES

1. Blackwood J.D. & Bowden F.P. - 1952, Proc. Roy. Soc. Lond. A 213, 285.
2. Heavens S.N. - 1973, Ph.D. Thesis, University of Cambridge.
3. Heavens S.N. & Field J.E. - 1974, Proc. Roy. Soc. Lond. A 338, 77.
4. Swallowe G.M. - 1979, Ph.D. Thesis, University of Cambridge.
5. Swallowe G.M. & Field J.E. - 1982, Proc. Roy. Soc. Lond. A 379, 389.
6. Field J.E., Swallowe G.M. & Heavens S.N. - 1982, Proc. Roy. Soc. Lond. A 382, 231.
7. Krishna Mohan V. & Field J.E. - 1984, Combustion and Flame 56, 269.
8. Krishna Mohan V., Field J.E. & Swallowe G.M. - 1984, Combustion Sci. and Tech. 44, 269.
9. Field J.E., Palmer S.J.P., Pope P.H., Sundararajan R. & Swallowe G.M. - 1985, Proc. 8th Int. Symp. on Detonation, Albuquerque, U.S.A.
10. Nadai A. - 1931, "Plasticity", McGraw Hill.
11. Timoshenko S. - 1941, "Strength of Materials", Vol. II, van Nostrand, p.403.
12. Prandtl L. - 1923, ZAAM 3, 401.
13. Hill R. - 1950, "Mathematical theory of plasticity", Clarendon Press.
14. Shroeder W. & Webster D.A. - 1949, J. Appl. Mech. 16, 289.
15. Kolevo N.A. - 1946, Trudy Kazan Khim. Tech. Inst. 10, 91.
16. Afanas'ev G.T. & Bobolev V.K. - 1971, "Initiation of Solid Explosives by Impact", Israel Program for Scientific Publications, Jerusalem.
17. Kolsky H. - 1953, "Stress Waves in Solids", Clarendon Press, Oxford.
18. Gorham D.A. - 1979, Inst. of Physics U.K. Conf. Series 47, 16.
19. Pope P.H. & Field J.E. - 1984, J. Phys. E: Sci. Instrum. 17, 817.
20. Awaji H. & Sata S. - 1979, J. Engr. Mater. and Tech. 101, 140.
21. Johnson H.D. - 1979, MH SMP-78-08.
22. Johnson H.D. - 1979, MH SMP-79-26.
23. Johnson H.D. - 1981, MH SMP-81-22.
24. Chiang F.P. - 1982, Opt. Eng. 21, 379.
25. Ennos A.E. - 1975, in "Laser Speckle and Related Phenomena", Springer, Heidelberg, 203.
26. Huntley J.M. - 1986, J. Phys. E: Sci. Instrum. 19, 43.
27. Coffey C.S. & Jacobs S.J. - 1981, J. Appl. Phys. 52, 6991.
28. Wingert L.E. - U.S. Patent 3031329.
29. Fuller K.N.G., Fox P.G. & Field J.E. - 1975, Proc. Roy. Soc. Lond. A 341, 537.
30. Carlslow H.S. & Jaeger J.C. - 1959, "Conduction of Heat in Solids", 2nd edition, Clarendon Press, Oxford, p.54.
31. Swallowe G.M., Field J.E. & Horn L.A. - 1986, J. Mater. Sci. 21, 4089.
32. Hutchinson C.D., Swallowe G.M. & Field J.E. - 1986, in "Shock Waves in Condensed Matter", ed. Gupta Y.M., Plenum, p.891.
33. Winter R.E. & Field J.E. - 1975, Proc. Roy. Soc. Lond. A 343, 399.
34. Field J.E. & Zafar M.A. - 1972, J. Phys. D: Appl. Phys. 5, 2015.
35. Bastow T.J., Packer M.E., Gane N. - 1969, Nature 222, 27.
36. Bowden F.P. & Gurton O.A. - 1949, Proc. Roy. Soc. Lond. A 198, 337.
37. Bowden F.P. & Gurton O.A. - 1949, ibid, 350.
38. Coffey C.S., Frankel M.J., Liddiard T.P. & Jacobs S.J. - 1981, Proc. 7th Int. Symp. on Detonation, O.N.R., p.970.
39. Burch J.M. & Tokarski J.M.J. - 1968, Opt. Acta. 15, 101.
40. Huntley J.M. - 1986, Appl. Opt. 25, 382-386.

41. Huntley J. M. - 1986/7, Opt. Lasers Eng. 7, 149-161.
42. Huntley J. M. and Field J.E. - 1986, Appl. Opt. 25, 1665- 1669.
43. Hondros G. - 1959, Aust. J. Appl. Sci. 10 (3), 243-268.
44. Bossaert W., Dechaene R. and Vinckier A. - 1968, J. Strain Analysis 3 (1), 65-75.
45. Palmer S. J. P., Field J. E. and Hu X. M. - 1984, Cavendish Report.
46. Huntley J. M. and Field J. E. - 1988, Eng. Fract. Mech. (to be published).
47. Rice J. R. - 1968, in "Fracture", ed. Liebowitz H., Academic Press, New York, Vol. II, Chapter 3.
48. Huntley J. M. - 1986, PhD Thesis, University of Cambridge.
49. Nishioka T. and Atluri S. N. - 1983, Eng. Fract. Mech. 18 (1), 1-22.
50. Williams J. G. - 1984, "Fracture Mechanics of Polymers", John Wiley and Sons.
51. Burch J. M. and Forno C. - 1982, Opt. Eng. 21, 602-614.
52. Takeda M., Ina H. and Kobayashi S. - 1982, J. Opt. Soc. Am. 72, 156-160.
53. Palmer, S. J. P. & Field, J. E. - 1982 Proc. Roy. Soc. Lond. A 383, 399.
54. Cady H. - Private Communication.
55. Gent A. N. - 1980, J. Mat. Sci. 15, 2884.
56. Nicholson D. W. - 1979, J. Adhesion 10, 255.

FIGURE CAPTIONS

- Fig. 1 A cross-section of the C4 drop-weight system. W is the weight, M a mirror, and G the toughened glass anvils with the specimen S between them.
- Fig. 2 Plots showing the radius and radial expansion velocities of an ideal plastic sample offering negligible retardation to the drop weight. Specimen is 4 mm diameter by 1 mm high; impact velocity 4.5 m s^{-1} .
- Fig. 3 A cross-section of the instrumented drop weight. W is the weight, A the anvil, and R_1 , R_2 , and R_3 are the steel rollers, the lowest being the load cell having strain gauges G. Ignition is recorded either by a light detector D, or by an electrical circuit which detects ionisation.
- Fig. 4 (a) Fracture in a tall sample of brittle material. Region I -- Rigid, Region II -- Brittle, S -- Shear failure.
 (b) Compression of a flat specimen of semi-brittle material. Region I -- Rigid; Region II -- Brittle, Region III -- Plastic.
 (c) The Prandtl slip line field for a plastic material deformed in plane strain between rough anvils. Region I -- Rigid.
 (d) Schematic of an explosive sample trapped in a "cavity" between anvils with elastic deformation.
- Fig. 5 Schematic of the direct-impact apparatus. A cylindrical projectile compresses a small specimen (1-2 mm diameter) supported on the end of an instrumented pressure bar. Two miniature strain gauges are mounted diametrically opposite each other (one shown as S). The Imacon high speed camera views the specimen through the image-splitting refraction element and lens L. Illumination is provided by a xenon flash and condenser lens C. The camera and light source are triggered when the projectile interrupts a laser beam.
- Fig. 6 Loading arrangement used in Brazilian test.
- Fig. 7 Apparatus for calibration of heat sensitive film. F is disc of film, R cylindrical roller, S sliding support, J joint to adjust drop-tube perpendicular to heated surface, D drop-tube, C catcher arm to prevent bounces causing repeated impacts, I thermal insulation, H heater element, and B steel block.
- Fig. 8 Calibration curves for film. Density is measured relative to a standard neutral density filter. Times represent the contact time of the film with the heated plate. Error bar is shown is typical of all points. Contact times (μsec): (●) 30; (◐) 50; (◑) 140; (▽) 330; (▲) 440; (○) 600.
- Fig. 9 High-speed photographic sequence of impact on a 5 mm diameter, 1 mm high PP disc. Times after frame (a):
 (b) 168 μsec ; (e) 378 μsec ;
 (c) 268 μsec ; (f) 402 μsec .
 (d) 335 μsec ;
 The diffuse shading around the disc in frame (a) is due to overwriting on the film.
- Fig. 10 Pattern left on film after impact on a PP disc. Arrows indicate final diameter of the disc. Original in colour.
- Fig. 11 Pattern left on film after impact on a Nylon 6 disc. Arrows indicate final diameter of the disc. Original in colour.

- Fig. 12 Sketches of shear and cracking sequences observed during impact on PC, PS, and PMMA. The sequence was similar for each of the materials although the duration and time between stages differed. The failure frequently started as shear banding but ended with separation (cracking) along the bands:
 (a) represents initial undeformed disc;
 (b) disc at completion of plastic flow stage;
 (c) failure by "parallel shear-cracks";
 (d) continued failure by "perpendicular shear-cracks".
- Fig. 13 Impact on a 5 mm diameter, 1 mm high disc of PS. Times after frame (a):
 (b) 35 μ sec; (f) 196 μ sec;
 (c) 42 μ sec; (g) 203 μ sec;
 (d) 49 μ sec; (h) 259 μ sec;
 (e) 189 μ sec;
- Fig. 14 Impact on a 5 mm diameter, 1 mm high disc of PC. Times after frame (a):
 (b) 161 μ sec; (f) 275 μ sec;
 (c) 188 μ sec; (g) 281 μ sec;
 (d) 241 μ sec; (h) 288 μ sec;
 (e) 268 μ sec; (i) 295 μ sec.
- Fig. 15 Trace obtained from crack running through PMMA. F is the fracture surface, T the trace left on the film, H the film, and P the remaining portion of the PMMA on the film surface. Original in colour.
- Fig. 16 Pattern left on film after catastrophic failure of PC. The PC is still in contact with the film and is here viewed through the film. Original in colour.
- Fig. 17 Impact on PETN + Kel-F 800. See text for details. Frame time (μ s):
 (1) 0; (6) 462;
 (2) 168; (7) 469;
 (3) 295; (8) 476;
 (4) 395; (9) 496;
 (5) 456;
- Fig. 18 True stress/strain curves for samples of Kel-F 800 and PTFE.
- Fig. 19 Impact sequence on polymer discs: PE, polyethylene wax; PU, polyurethane; V, Viton A. Times of frames after contact: 63, 91, 133, 140, 147, and 154 μ s. Melting in PE takes place between frames 1 and 2. Field of view 20 mm.
- Fig. 20 Impact sequence on polymer discs. In this sequence the weight is rebounding. Times of frames after contact: 504, 525, 553, and 560 μ s. Note fracture in PU and ductile tearing in Viton. Field of view 20 mm.
- Fig. 21 Stress-strain curves for PBX compositions containing type B HMX. Strain rate 200 s^{-1} .
- Fig. 22 Signals from the instrumented drop weight recorded with mock explosive samples. In the upper trace the specimen was 2.5 mm high and shows a double peak structure indicating fracture, compaction and pinch. For the lower trace a 1.5 mm specimen was used which enters the pinch regime almost immediately. Impact velocity 1 m s^{-1} .
- Fig. 23 Results from the drop-weight apparatus for impacts on PE compositions. Note that compositions G and H ignite after the pressure peak. Impact velocity 3 m s^{-1} .

- Fig. 24 (a) An example of a local ignition. Maximum velocity 170 m s^{-1} , framing interval $7 \mu\text{s}$, field of view 20 mm .
(b) Radius/time plot.
- Fig. 25 (a) An example of a local ignition. Maximum velocity 114 m s^{-1} , framing interval $7 \mu\text{s}$, field of view 20 mm .
(b) Radius/time plot.
- Fig. 26 (a) An example of widespread ignition. Maximum velocity 190 m s^{-1} , framing interval $7 \mu\text{s}$, field of view 20 mm .
(b) Radius/time plot.
- Fig. 27 (a) An example of widespread ignition. Maximum velocity 190 m s^{-1} , framing interval $7 \mu\text{s}$, field of view 20 mm .
(b) Radius/time plot.
- Fig. 28 A sample after impact in the C4 drop weight without ignition. Note shear bands in the centre of the specimen.
- Fig. 29 Impact on a 25 mg PETN sample from a drop height of 1.3 m . See text for details, but note in particular the shear band formation which causes ignition and the transparency which is due to sintering and fusion. Interframe times: $0, 28, 49, 63, 77, 91, 105, 112$, and $133 \mu\text{s}$. Field of view 20 mm .
- Fig. 30 Impact on a 25 mg PETN sample from a drop height of 1.3 m . Shear bands are arrowed frame 1. Interframe times: $0, 7, 14$, and $21 \mu\text{s}$. Field of view 20 mm .
- Fig. 31 Heat sensitive film record of an impact on PETN. The original was in colour. Clear evidence of shear banding and associated ignition. See text for details.
- Fig. 32 Transmitted light photomicrographs of shear banding in PETN after impact but where ignition failed to occur. Photograph 2 is an enlargement of the area outlined in white in 1. Sample mass 15.9 mg .
- Fig. 33 Two recovered discs of heat-sensitive film (HSF) photographed in transmitted light. The explosive has been removed:
(a) The approximate area that the HMX occupied after impact is indicated. The discolouration of the HSF disc appears as a central pattern consisting of both radial and parallel lines. The sample originally covered an area similar to the discoloured area.
(b) Partial reaction has occurred and part of the HSF disc has been consumed, but the band-like pattern is still apparent near the centre of the disc.
- Fig. 34 HSF recovered after impact of HMX. The view is of the emulsion (explosive) side of the disc in reflected light after removal of the explosive. The disc consists of fairly parallel lines, some of which bifurcate, characteristic of shear bands. The lines are brown-black, indicating the sample has been hot at these points. Notice the line, A, shows no signs of failure of the disc of HSF. The wider lines have a brown border and are broadest in the black (very hot) ignition region, B. Original in colour.
- Fig. 35 HSF recovered after impact of HMX showing branching of the shear bands and discolouration where branching occurs. Original in colour.
- Fig. 36 HSF recovered after impact of HMX. Residual HMX on film. View shows failure line running through the intersection of two slip surfaces of an HMX crystal at E. Parts of either the disc or HMX have been molten, F. Original in colour.

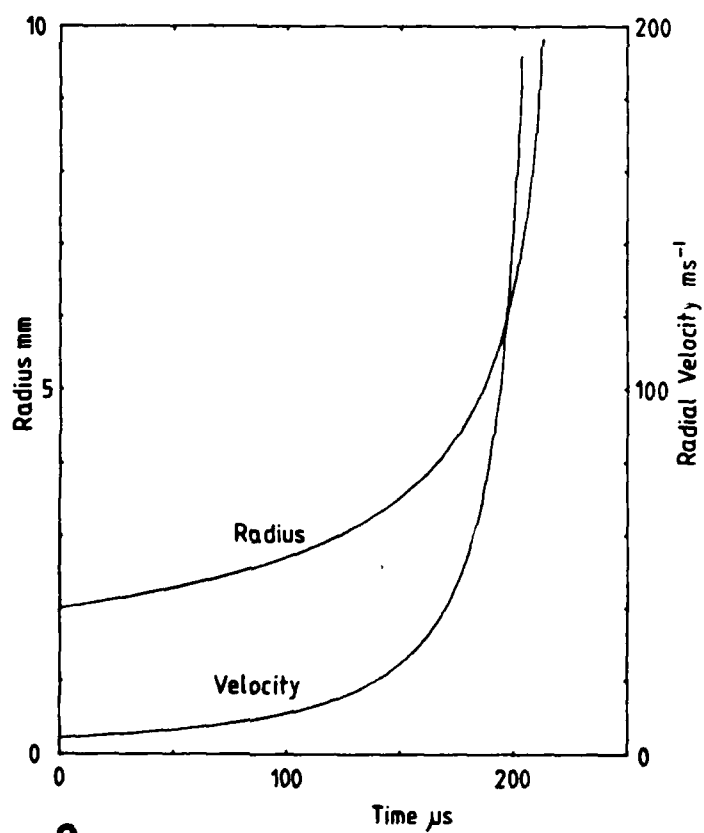
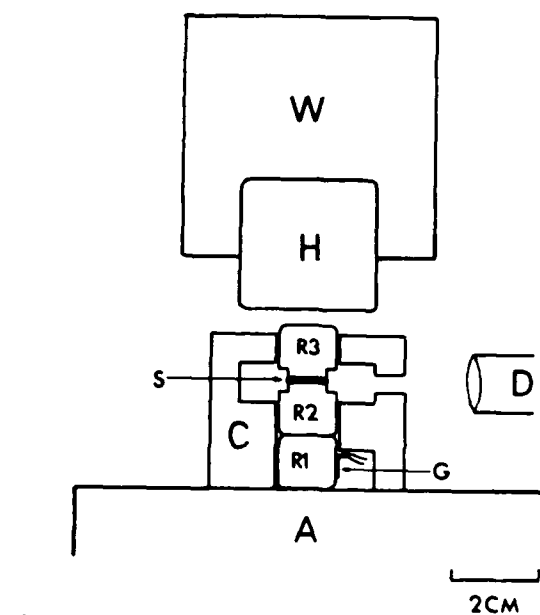
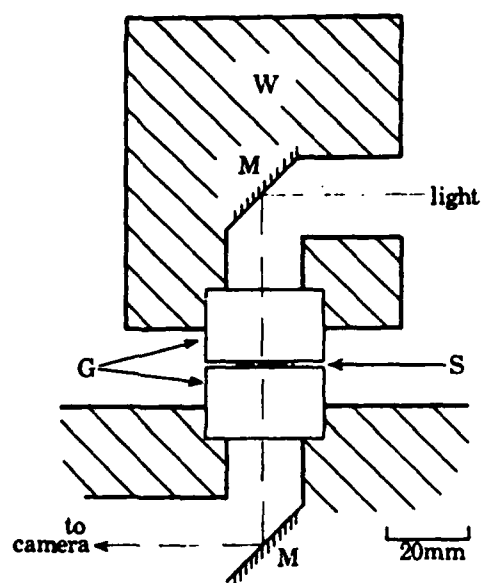
- Fig. 37 Photographs of explosive remaining on 12.7mm diameter hardened steel rollers after impact. The rollers are from separate experiments. (a) is from a test with heat-sensitive film. Notice the lines in the disc resemble the failure pattern in the explosive. (b), (c) and (d) were obtained during impacts with bare metal rollers. (b) shows a band-like failure pattern. When the residue is spread across both rollers used for impact, the shear band pattern is more clearly noticeable, as in (c) and (d).
- Fig. 38 Impact on type A HMX, widespread ignition with rapid flow (maximum velocity 240 m s^{-1}). Framing interval $6.5 \mu\text{s}$, field of view 20mm.
- Fig. 39 Impact on fine grain HMX (TC/12). Local ignition during rapid flow (maximum velocity 240 m s^{-1}), framing interval $7 \mu\text{s}$, field of view 20 mm.
- Fig. 40 Type B HMX. Maximum velocity 185 m s^{-1} . The first local ignitions seen in frame 48 fade. A local ignition which propagates starts in frame 54. Note the banded appearance in frame 27. Framing interval $7 \mu\text{s}$, field of view 20 mm.
- Fig. 41 Enlarged view of frames 48, 49 and 54 of Fig. 40. Frame 1 is $337 \mu\text{s}$ after first contact.
- Fig. 42 Damage to the surface of glass anvils after impact of HMX. (a) full reaction in fine HMX; (b) partial reaction in fine HMX (damage is arrowed); (c) full reaction in coarse HMX; (d) partial reaction in coarse HMX.
- Fig. 43 Scanning electron micrographs of the damaged surface of glass anvils after impact initiation of HMX. (a) fine (type B) HMX, which shows "flower pattern" damage; (b) coarse (type A) HMX, which shows flaking damage, similar to fracture caused by giant laser pulses. The horizontal lines are due to charging of the specimen.
- Fig. 44(a) The Brazilian test loading geometry. A disc is loaded across the diameter between two curved anvils. The larger square represents the region over which the displacements were measured, and the inner square is the region over which the strains could be accurately calculated. The diameter of the disc for these experiments is 10.0 mm.
- Fig. 44(b) Theoretical stress distribution along the horizontal and vertical diameters (after Hondros⁴³). On the horizontal diameter, σ_{xx} and σ_{yy} are displayed as σ_{rx} and $\sigma_{\theta x}$ respectively; on the vertical diameter they are displayed as $\sigma_{\theta y}$ and σ_{ry} . Note the sign convention used on the axes: σ_{xx} is tensile over most of the vertical diameter whereas σ_{yy} is compressive.
- Fig. 44(c) Theoretical strain distribution along the horizontal and vertical diameters (after Hondros⁴³). On the horizontal diameter, ϵ_{xx} and ϵ_{yy} are displayed as ϵ_{rx} and $\epsilon_{\theta x}$ respectively; on the vertical diameter they are displayed as $\epsilon_{\theta y}$ and ϵ_{ry} . The sign convention used is the same as in 44(b): ϵ_{xx} is tensile over most of the vertical diameter whereas ϵ_{yy} is compressive.
- Fig. 45 Measured displacement field from the first speckle photograph of composition I. The upper anvil moved downward while the lower anvil remained fixed, so that all the displacements have a rigid body component in the -y direction. (a) shows the displacements in vector format; each vector required the analysis of one Young's fringe pattern. Material which was at the top of any given vector at the time of the first exposure had moved to the bottom of the vector at the time of the second exposure. The vectors have been magnified relative to the specimen coordinate system for clarity: note the $50 \mu\text{m}$ scale. (b) and (c) are equivalent representations of the displacement field, being contour maps of u_x and u_y respectively. The numbers on the contours are μm ; in (b), the contour spacing is $0.5 \mu\text{m}$.

- Fig. 46 Measured displacement field from the second speckle photograph of composition I. (a) shows the displacements in vector format; the comments made in the caption to Fig. 45 also apply here. (b) and (c) are equivalent representations of the displacement field, being contour maps of u_x and u_y respectively. The numbers on the contours are μm . Between the two exposures recorded on this photograph, the disc has started to fail along the lower half of the vertical diameter. The discontinuity in u_x across the failure zone shows up as a sudden change in displacement direction (a) and as a 'cliff edge' in the contour map of u_x (b). u_y does not appear to have been appreciably affected by the failure.
- Fig. 47 Strain fields calculated from the measured displacement fields for composition I. ϵ_{xx} and ϵ_{yy} from the first photograph are shown in (a) and (b). (c) and (d) are the corresponding strains for the second photograph. The numbers on the contours should be multiplied by 10^{-5} (except (c): multiply by 10^{-4}) to give the true strain values. As explained in the text, the algorithm for calculating strains requires a continuous displacement field. The strains displayed in (c) are therefore in error near the failure zone.
- Fig. 48 Strain fields calculated from the measured displacement fields for composition A. ϵ_{xx} and ϵ_{yy} from the first photograph are shown in (a) and (b). (c) and (d) are the corresponding strains for the second photograph. The numbers on the contours should be multiplied by 10^{-5} to give the true strain values.
- Fig. 49 (a) Displacement field around a sharp crack in PMMA under quasi-static loading conditions, measured using laser speckle photography. Each vector results from the analysis of 1 Young's fringe pattern. (b) Orientation of crack relative to the coordinate system. (c), (d) u_x and u_y contour maps of the displacement field shown in (a). Contour interval = $1 \mu\text{m}$.
- Fig. 50 Electrical method for measuring crack velocity.
- Fig. 51 Typical digital oscilloscope trace of the resistor network signal.
Hor. scale: $20.0 \mu\text{s div}^{-1}$.
Distance between silver strips: 6 mm.
- Fig. 52 Typical digital oscilloscope trace of the resistor network signal when the crack is initiated by the detonator-driven wedge. Channel 1('CH1') is a photodiode signal showing the light produced by the ruby laser. The time resolution of the scope ($0.2 \mu\text{s}$) meant that the signal had to be low-pass filtered in order to record the 50 ns pulses.
- Fig. 53 Print of a dynamic speckle photograph recorded with the ruby laser, together with some representative fringe patterns from the points indicated. Crack velocity = 287 m s^{-1} .
- Fig. 54 Measured displacement field from the speckle photograph shown in Fig. 53. A and B show the approximate crack tip positions at the time of the first and second light pulses respectively. The inter-pulse time was $14.6 \mu\text{s}$. Displacements are shown on a 1.7 mm square mesh, scaled by 40 times.
- Fig. 55 Experimental arrangement for high resolution moiré photography. X: Xenon flash tube; F: filter (Kodak Wratten No. 44); FL1, FL2: field lenses; SG: specimen grating; RG: reference grating; OL1: high quality objective lens with masked aperture; OL2, C: recording camera with lens.
- Fig. 56 Moiré fringe pattern around a quasi-statically loaded crack in PMMA. The crack orientation is as shown in Fig. 49(b). The dimensions of the scribed rectangle are $26 \times 36 \text{ mm}^2$. The grating (spatial frequency: 150 l mm^{-1}) tended to inhibit crack growth and was therefore removed from the expected crack path: this region shows up as a horizontal white strip.

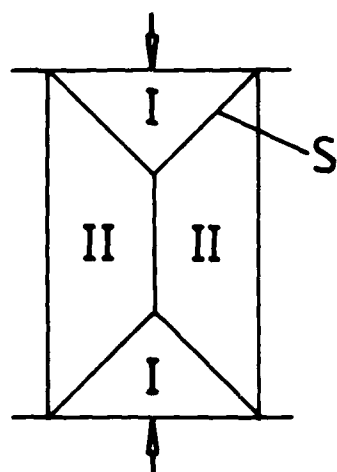
- Fig. 37 Photographs of explosive remaining on 12.7mm diameter hardened steel rollers after impact. The rollers are from separate experiments. (a) is from a test with heat-sensitive film. Notice the lines in the disc resemble the failure pattern in the explosive. (b), (c) and (d) were obtained during impacts with bare metal rollers. (b) shows a band-like failure pattern. When the residue is spread across both rollers used for impact, the shear band pattern is more clearly noticeable, as in (c) and (d).
- Fig. 38 Impact on type A HMX, widespread ignition with rapid flow (maximum velocity 240 m s^{-1}). Framing interval $6.5 \mu\text{s}$, field of view 20mm.
- Fig. 39 Impact on fine grain HMX (TC/12). Local ignition during rapid flow (maximum velocity 240 m s^{-1}), framing interval $7 \mu\text{s}$, field of view 20 mm.
- Fig. 40 Type B HMX. Maximum velocity 185 m s^{-1} . The first local ignitions seen in frame 48 fade. A local ignition which propagates starts in frame 54. Note the banded appearance in frame 27. Framing interval $7 \mu\text{s}$, field of view 20 mm.
- Fig. 41 Enlarged view of frames 48, 49 and 54 of Fig. 40. Frame 1 is $337 \mu\text{s}$ after first contact.
- Fig. 42 Damage to the surface of glass anvils after impact of HMX. (a) full reaction in fine HMX; (b) partial reaction in fine HMX (damage is arrowed); (c) full reaction in coarse HMX; (d) partial reaction in coarse HMX.
- Fig. 43 Scanning electron micrographs of the damaged surface of glass anvils after impact initiation of HMX. (a) fine (type B) HMX, which shows "flower pattern" damage; (b) coarse (type A) HMX, which shows flaking damage, similar to fracture caused by giant laser pulses. The horizontal lines are due to charging of the specimen.
- Fig. 44(a) The Brazilian test loading geometry. A disc is loaded across the diameter between two curved anvils. The larger square represents the region over which the displacements were measured, and the inner square is the region over which the strains could be accurately calculated. The diameter of the disc for these experiments is 10.0 mm.
- Fig. 44(b) Theoretical stress distribution along the horizontal and vertical diameters (after Hondros⁴³). On the horizontal diameter, σ_{xx} and σ_{yy} are displayed as σ_{rx} and $\sigma_{\theta x}$ respectively; on the vertical diameter they are displayed as $\sigma_{\theta y}$ and σ_{ry} . Note the sign convention used on the axes: σ_{xx} is tensile over most of the vertical diameter whereas σ_{yy} is compressive.
- Fig. 44(c) Theoretical strain distribution along the horizontal and vertical diameters (after Hondros⁴³). On the horizontal diameter, ϵ_{xx} and ϵ_{yy} are displayed as ϵ_{rx} and $\epsilon_{\theta x}$ respectively; on the vertical diameter they are displayed as $\epsilon_{\theta y}$ and ϵ_{ry} . The sign convention used is the same as in 44(b): ϵ_{xx} is tensile over most of the vertical diameter whereas ϵ_{yy} is compressive.
- Fig. 45 Measured displacement field from the first speckle photograph of composition I. The upper anvil moved downward while the lower anvil remained fixed, so that all the displacements have a rigid body component in the -y direction. (a) shows the displacements in vector format; each vector required the analysis of one Young's fringe pattern. Material which was at the top of any given vector at the time of the first exposure had moved to the bottom of the vector at the time of the second exposure. The vectors have been magnified relative to the specimen coordinate system for clarity: note the $50 \mu\text{m}$ scale. (b) and (c) are equivalent representations of the displacement field, being contour maps of u_x and u_y respectively. The numbers on the contours are μm ; in (b), the contour spacing is $0.5 \mu\text{m}$.

- Fig. 46 Measured displacement field from the second speckle photograph of composition I. (a) shows the displacements in vector format; the comments made in the caption to Fig. 45 also apply here. (b) and (c) are equivalent representations of the displacement field, being contour maps of u_x and u_y respectively. The numbers on the contours are μm . Between the two exposures recorded on this photograph, the disc has started to fail along the lower half of the vertical diameter. The discontinuity in u_x across the failure zone shows up as a sudden change in displacement direction (a) and as a 'cliff edge' in the contour map of u_x (b). u_y does not appear to have been appreciably affected by the failure.
- Fig. 47 Strain fields calculated from the measured displacement fields for composition I. ϵ_{xx} and ϵ_{yy} from the first photograph are shown in (a) and (b). (c) and (d) are the corresponding strains for the second photograph. The numbers on the contours should be multiplied by 10^{-5} (except (c): multiply by 10^{-4}) to give the true strain values. As explained in the text, the algorithm for calculating strains requires a continuous displacement field. The strains displayed in (c) are therefore in error near the failure zone.
- Fig. 48 Strain fields calculated from the measured displacement fields for composition A. ϵ_{xx} and ϵ_{yy} from the first photograph are shown in (a) and (b). (c) and (d) are the corresponding strains for the second photograph. The numbers on the contours should be multiplied by 10^{-5} to give the true strain values.
- Fig. 49 (a) Displacement field around a sharp crack in PMMA under quasi-static loading conditions, measured using laser speckle photography. Each vector results from the analysis of 1 Young's fringe pattern. (b) Orientation of crack relative to the coordinate system. (c), (d) u_x and u_y contour maps of the displacement field shown in (a). Contour interval = $1 \mu\text{m}$.
- Fig. 50 Electrical method for measuring crack velocity.
- Fig. 51 Typical digital oscilloscope trace of the resistor network signal.
Hor. scale: $20.0 \mu\text{s div}^{-1}$.
Distance between silver strips: 6 mm.
- Fig. 52 Typical digital oscilloscope trace of the resistor network signal when the crack is initiated by the detonator-driven wedge. Channel 1 ('CH1') is a photodiode signal showing the light produced by the ruby laser. The time resolution of the scope ($0.2 \mu\text{s}$) meant that the signal had to be low-pass filtered in order to record the 50 ns pulses.
- Fig. 53 Print of a dynamic speckle photograph recorded with the ruby laser, together with some representative fringe patterns from the points indicated.
Crack velocity = 287 m s^{-1} .
- Fig. 54 Measured displacement field from the speckle photograph shown in Fig. 53. A and B show the approximate crack tip positions at the time of the first and second light pulses respectively. The inter-pulse time was $14.6 \mu\text{s}$. Displacements are shown on a 1.7 mm square mesh, scaled by 40 times.
- Fig. 55 Experimental arrangement for high resolution moiré photography. X: Xenon flash tube; F: filter (Kodak Wratten No. 44); FL1, FL2: field lenses; SG: specimen grating; RG: reference grating; OL1: high quality objective lens with masked aperture; OL2, C: recording camera with lens.
- Fig. 56 Moiré fringe pattern around a quasi-statically loaded crack in PMMA. The crack orientation is as shown in Fig. 49(b). The dimensions of the scribed rectangle are $26 \times 36 \text{ mm}^2$. The grating (spatial frequency: 150 l mm^{-1}) tended to inhibit crack growth and was therefore removed from the expected crack path: this region shows up as a horizontal white strip.

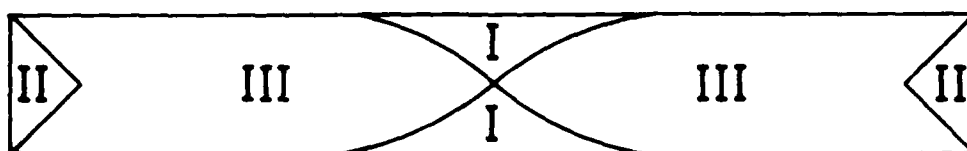
- Fig. 57 Phase maps showing the u_x (a) and u_y (b) displacement components, resulting from the analysis of the fringes in Fig. 56 by the Fourier transform method. The phase ranges from 0 (black) to 2π (white); the phase discontinuities occur at intervals of 2π , representing a relative displacement equal to the specimen grating pitch, $6.58\mu\text{m}$.
- Fig. 58 Moiré fringe pattern showing the horizontal displacement component produced by impact of a 2 mm diameter steel ball on the edge of a plate of PMMA, at 115 m s^{-1} . Area of plate within field of view = $15 \times 15\text{ mm}^2$. Specimen grating pitch = $6.7\mu\text{m}$; interframe time = $0.95\mu\text{s}$.
- Fig. 59 Moiré fringe pattern showing the vertical displacement component produced by ball impact. Experimental details as for Fig. 58.
- Fig. 60 Results for PBX 0344.
(a) Stress versus time plot; (b) Strain versus time plot; (c) Stress versus strain plot.
- Fig. 61 Results for PBX 0298.
(a) Stress versus time plot; (b) Strain versus time plot; (c) Stress versus strain plot.
- Fig. 62 Results for PBX 9501
(a) Stress versus time plot; (b) Strain versus time plot; (c) Stress versus strain plot.
- Fig. 63 Results for PBX 0407.
(a) Stress versus time plot; (b) Strain versus time plot; (c) Stress versus strain plot
- Fig. 64 Results for 9502
(a) Stress versus time plot; (b) Strain versus time plot; (c) Stress versus strain plot.
- Fig 65 Contour maps for PBX 0344/10
(a) Tensile strain distribution after 108 s; (b) Tensile strain distribution after 162 s; (c) Tensile strain distribution after 216 s; (d) Tensile strain distribution after 270 s.
- Fig 66 Contour maps for PBX 0344/10
(a) Contour plot of the horizontal displacements at 270 s.
(b) Contour plot of the corresponding tensile strain field.
(c) Contour plot of the vertical displacements at 270 s.
(d) Contour plot of the corresponding comprehensive strain field.
- Fig. 67 Time-lapse sequence for X-0298.
- Fig. 68 Fracture route montage for X-0298.
- Fig. 69 Time-lapse sequence for PBX 9501. Δ
- Fig. 70 Fracture route montage for PBX 9501.
- Fig. 71 Fracture route montages through a sample of 9501 before and after Brazilian Test.



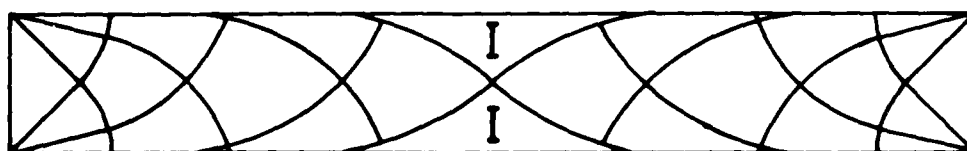
(a)



(b)

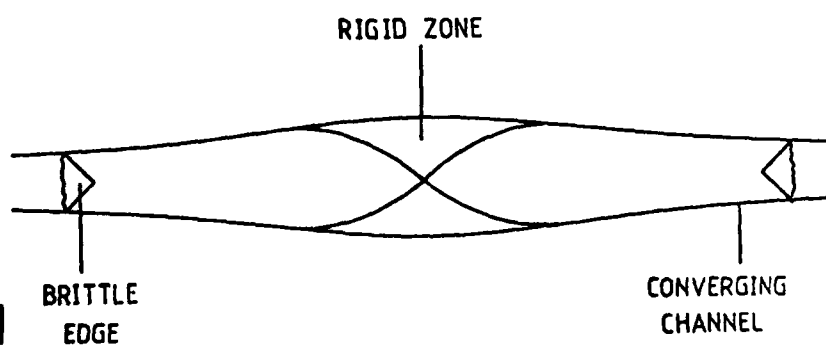


(c)

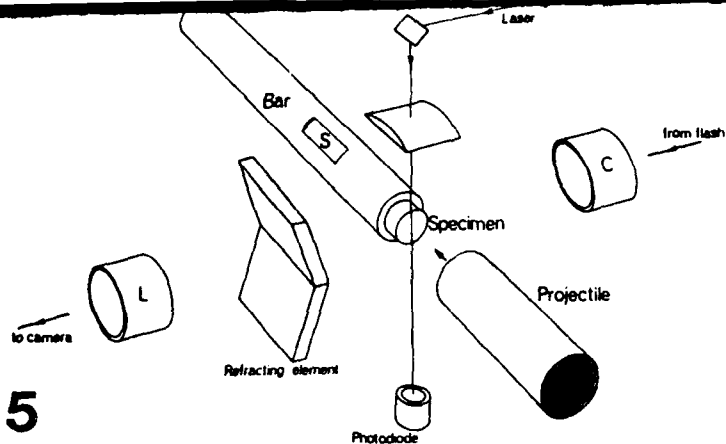


d

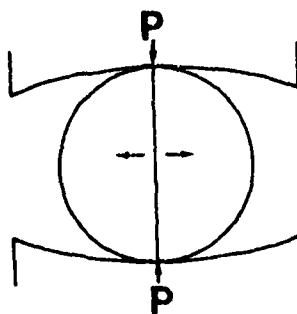
4



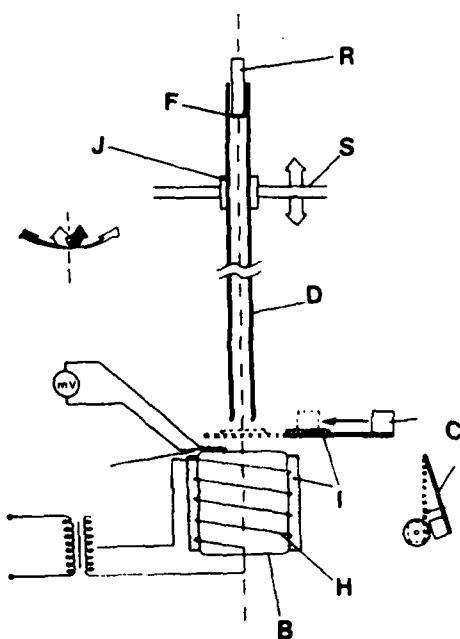
5



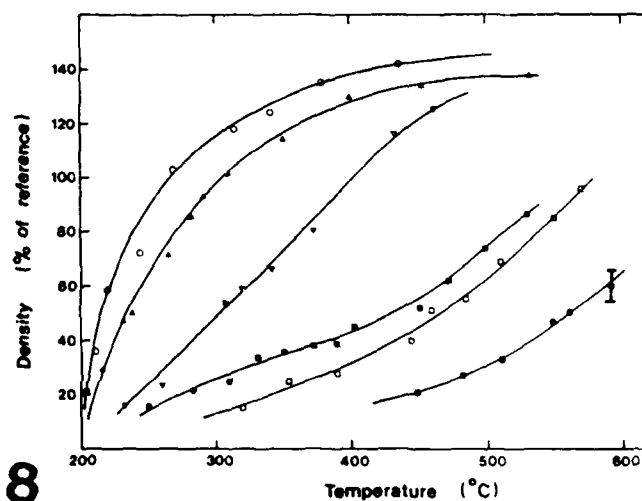
6



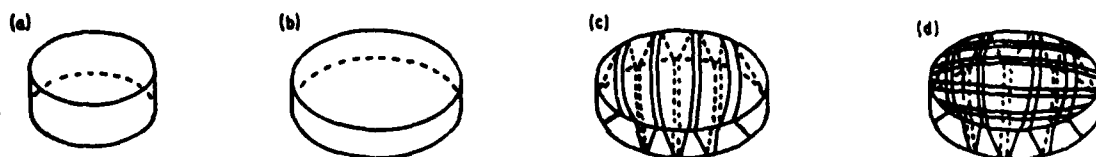
7

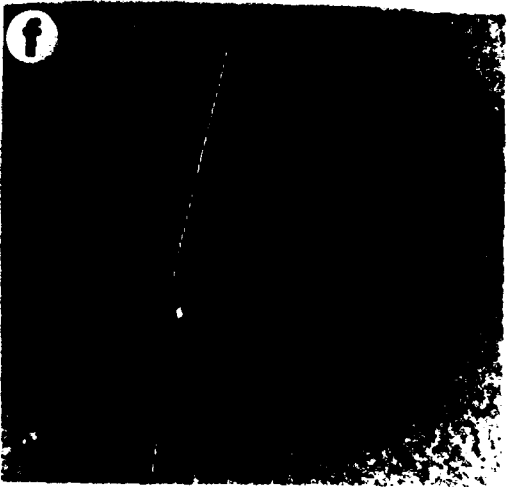
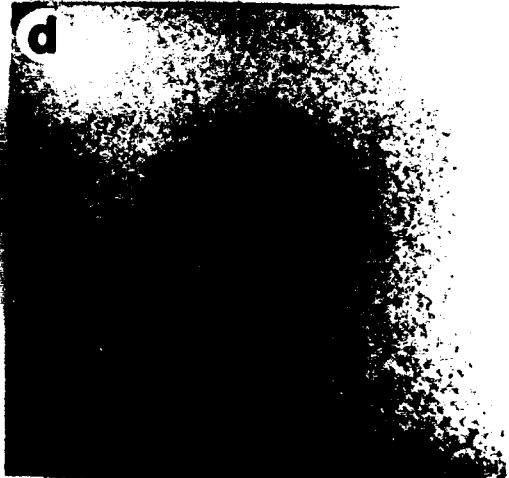
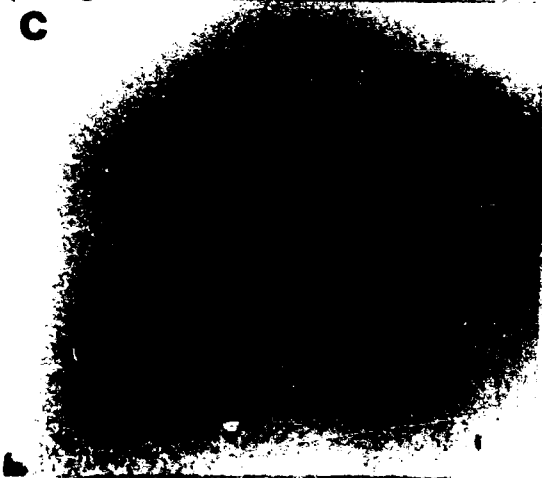
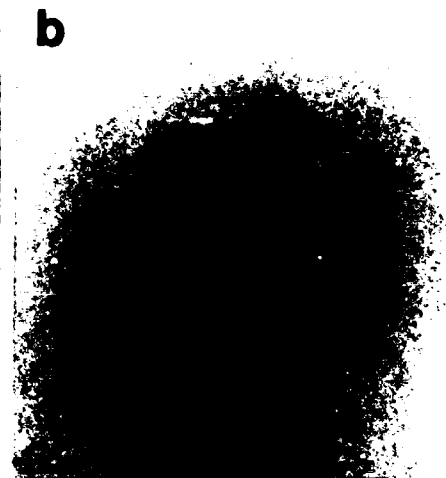


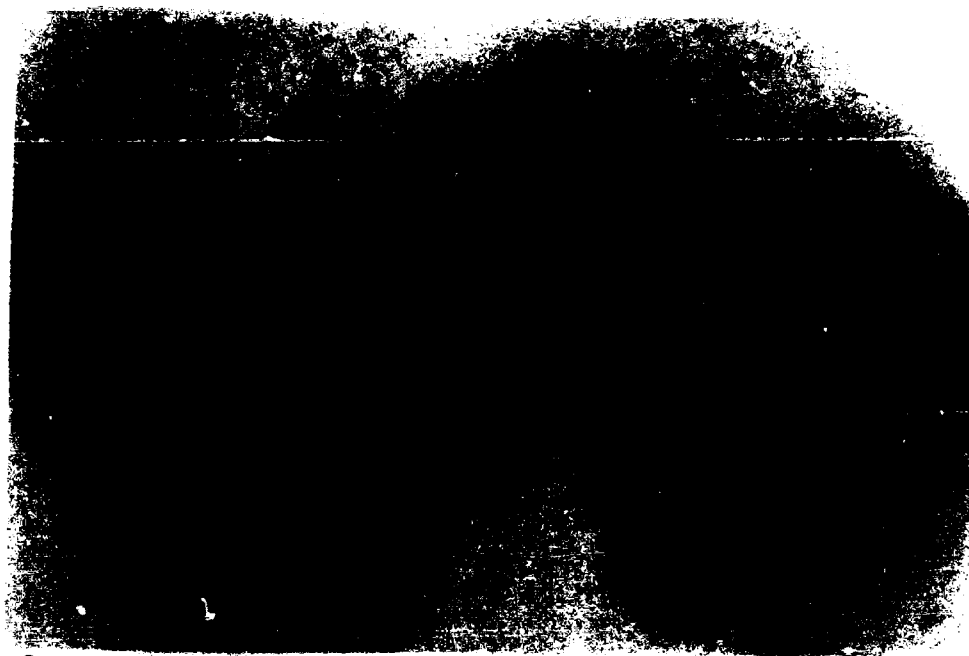
8



12



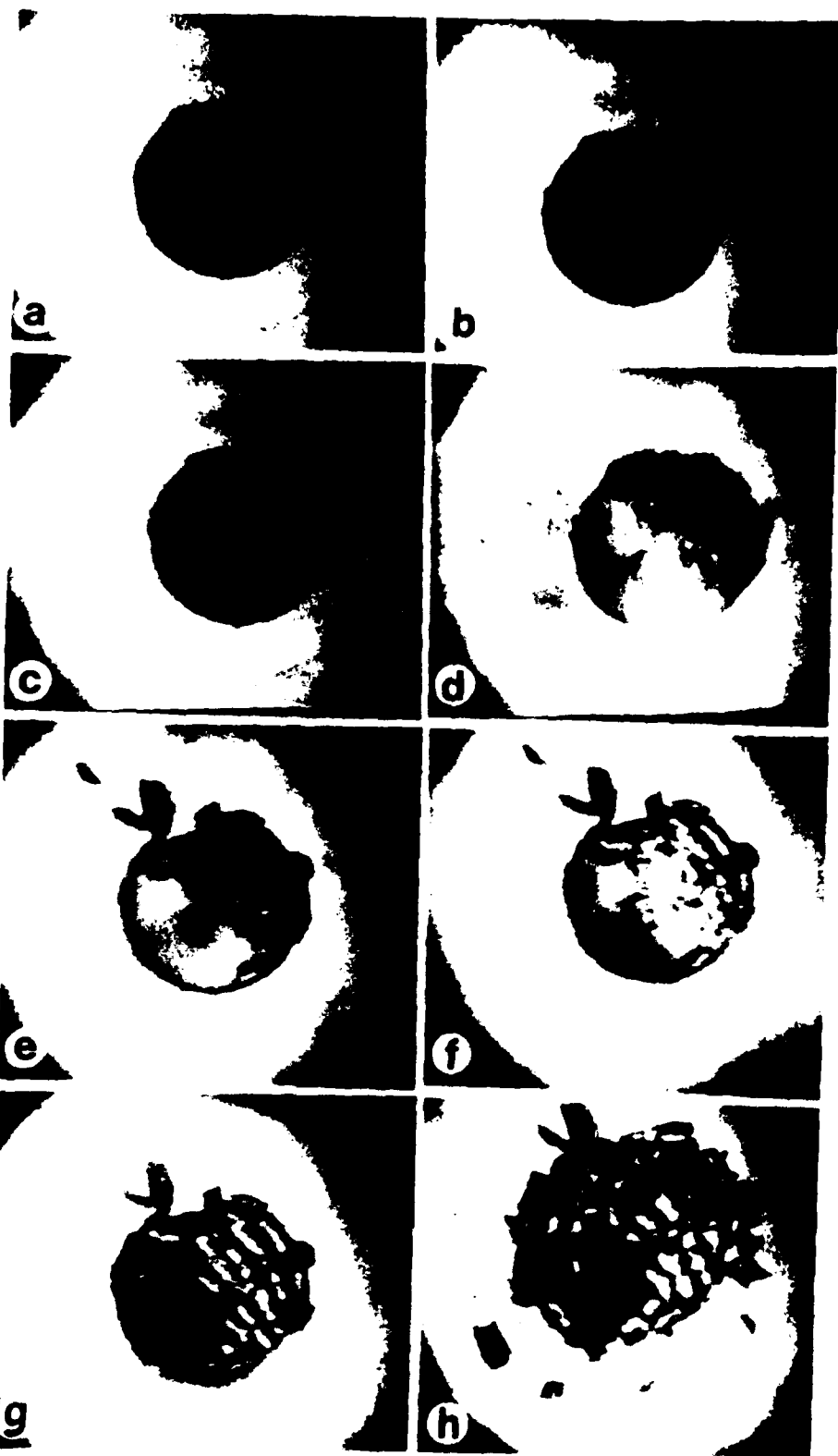


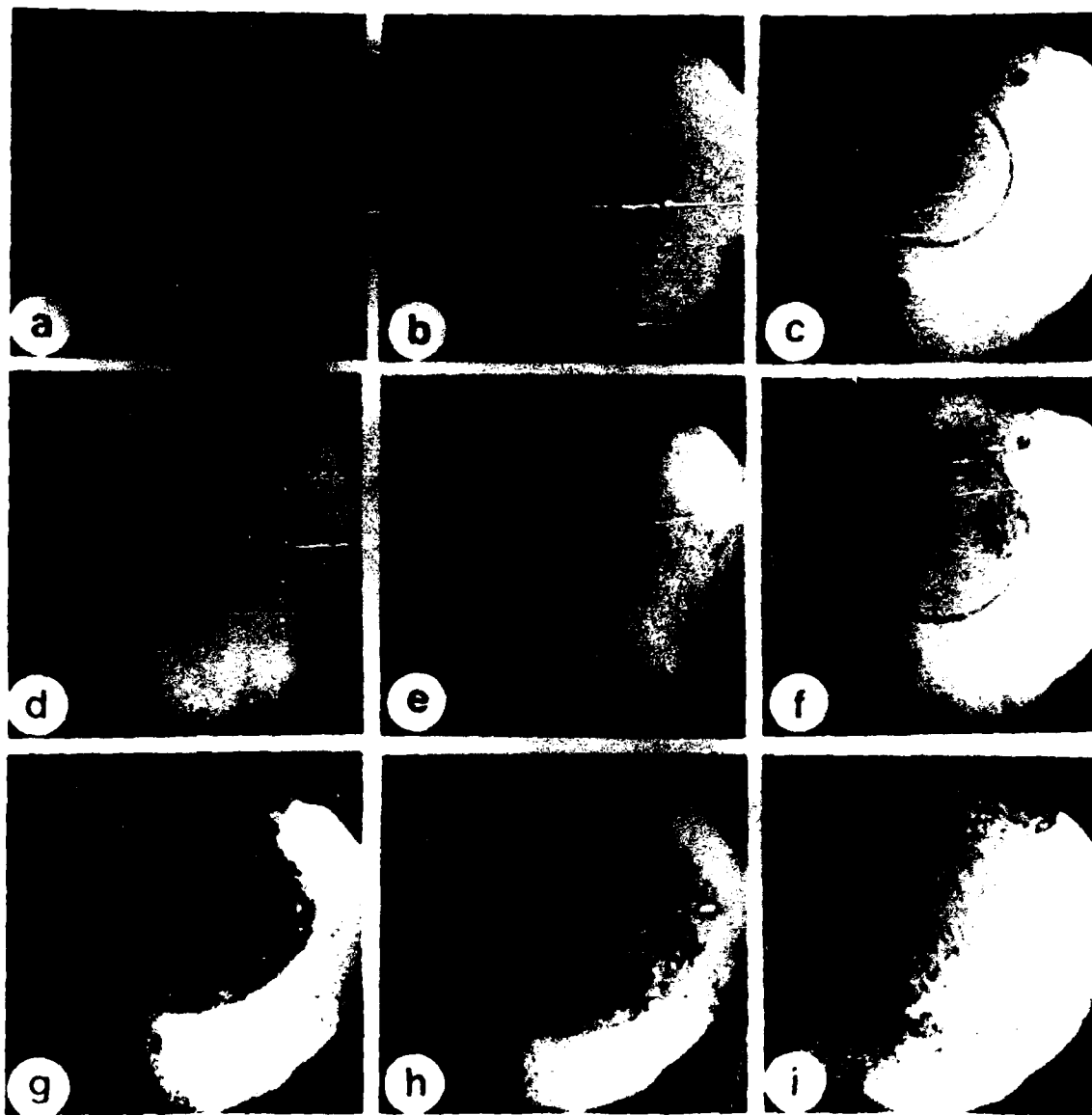


10



11



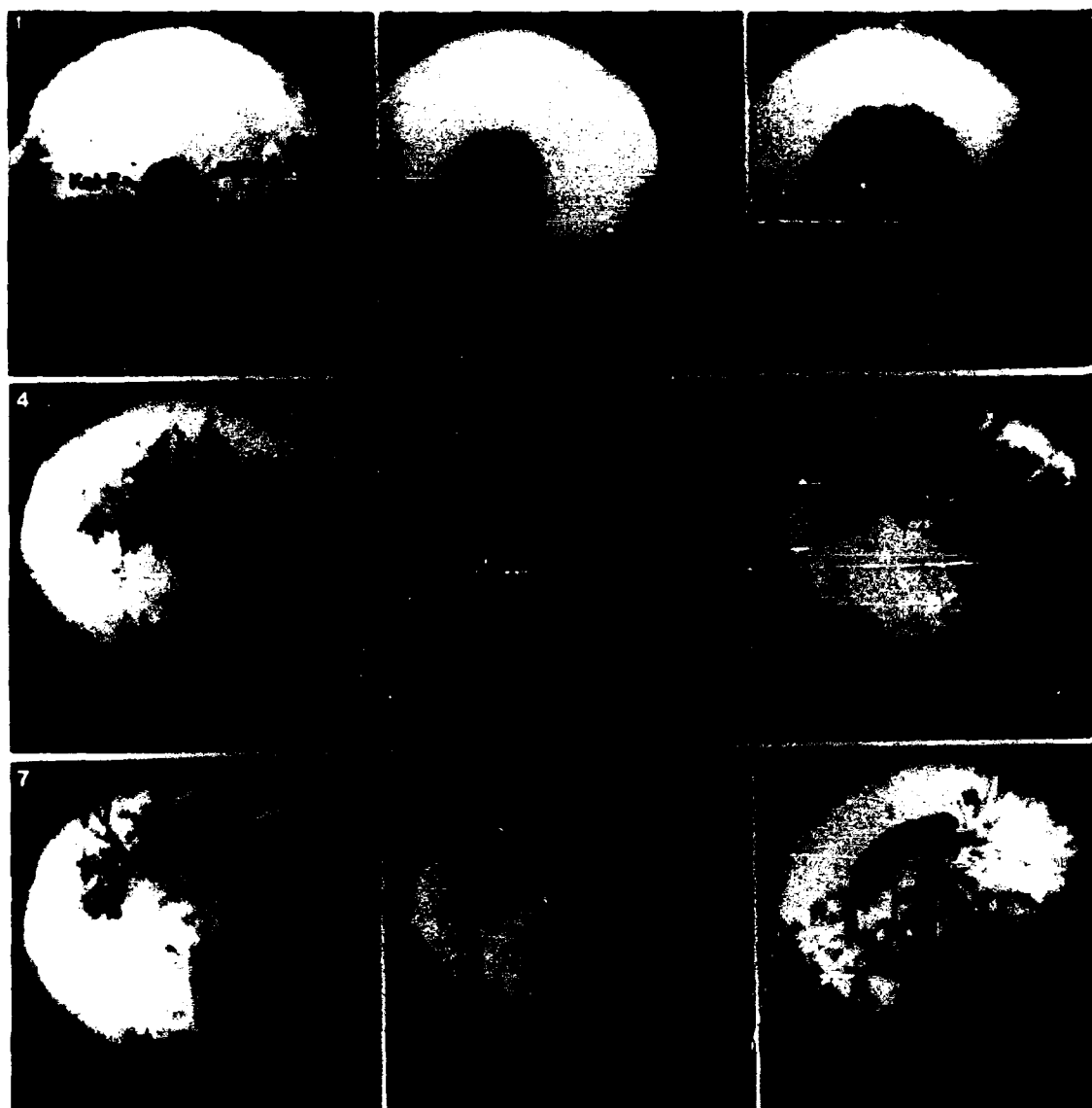


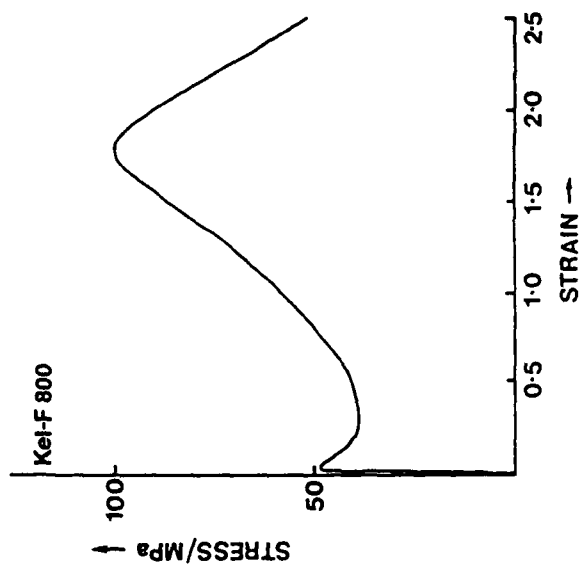
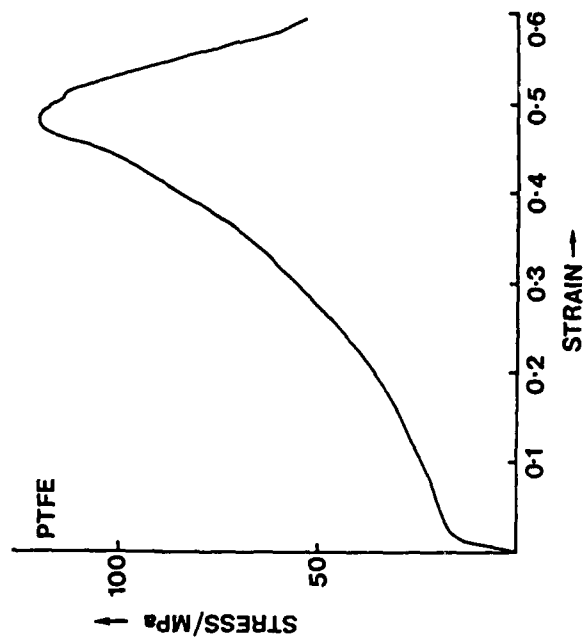


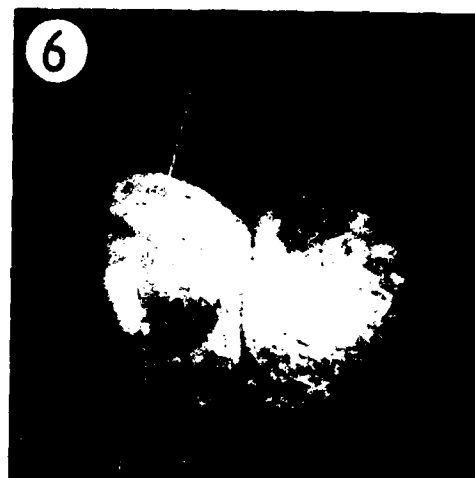
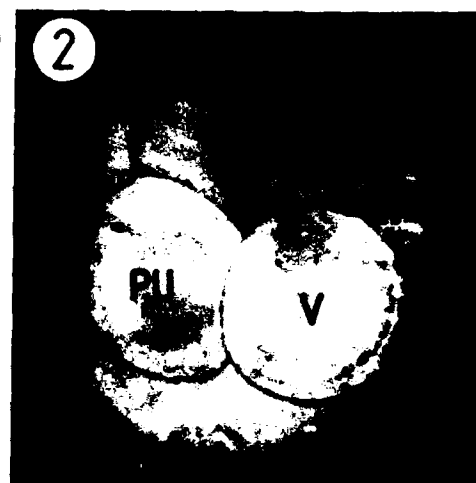
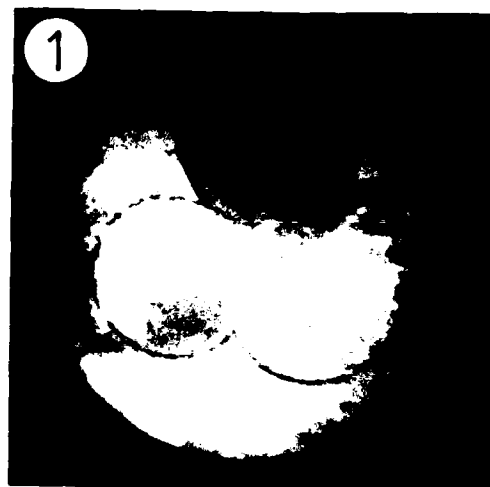
15

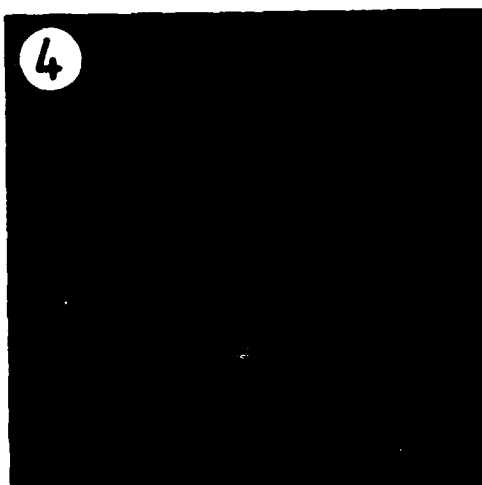
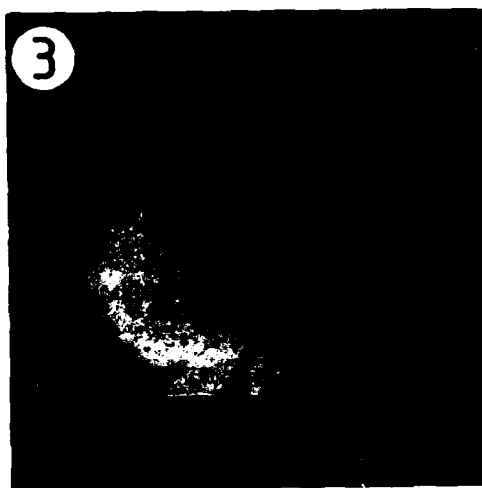
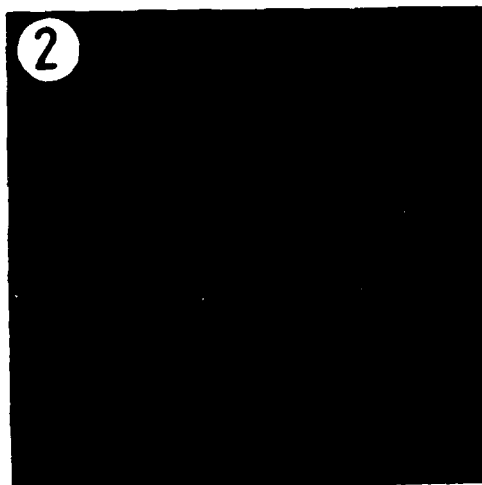
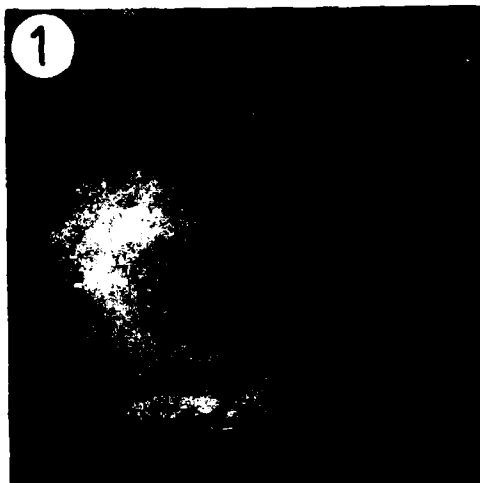


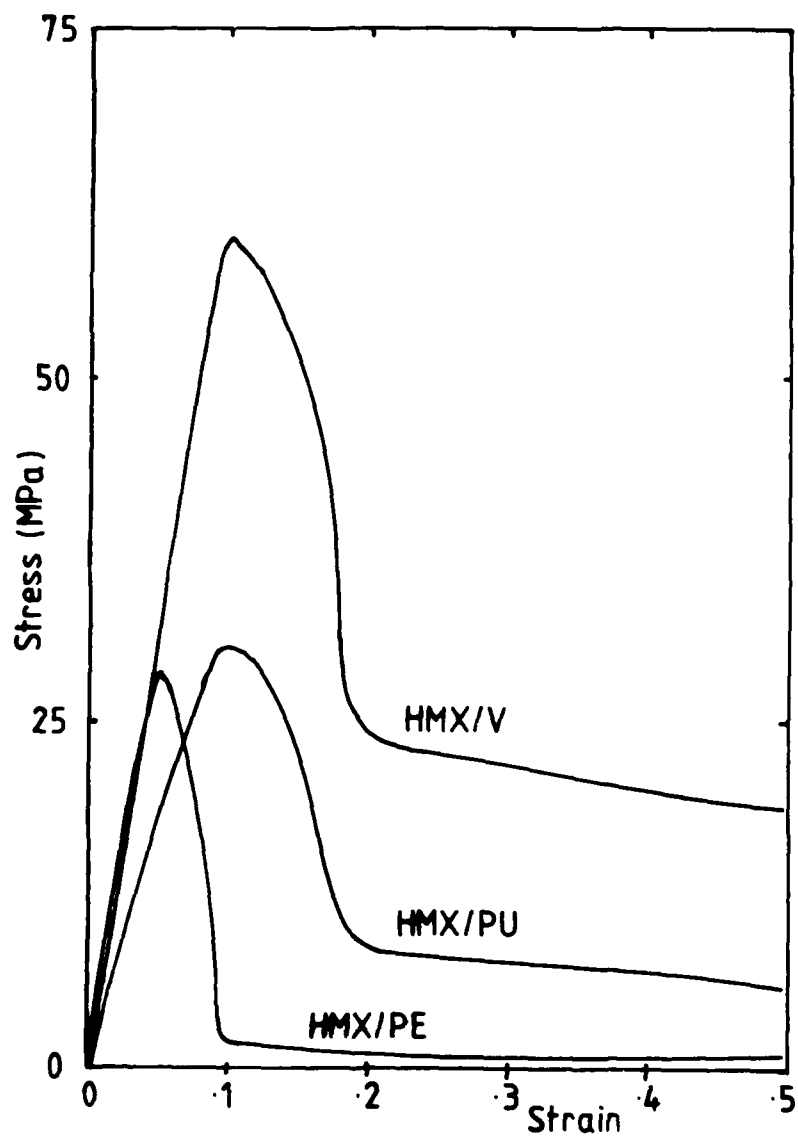
16

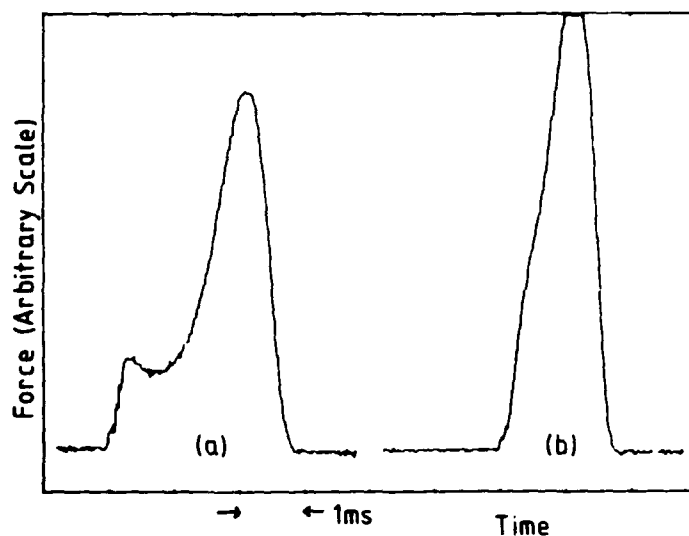




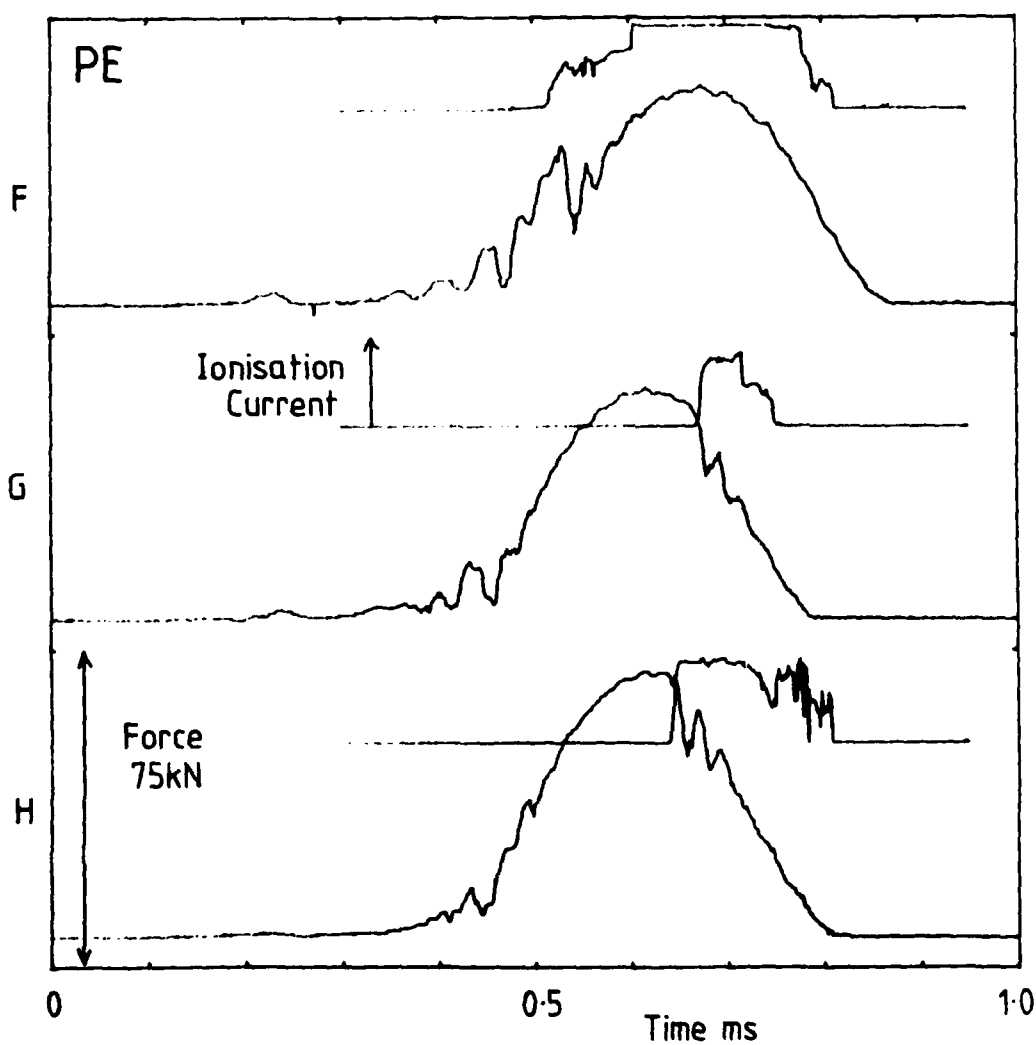




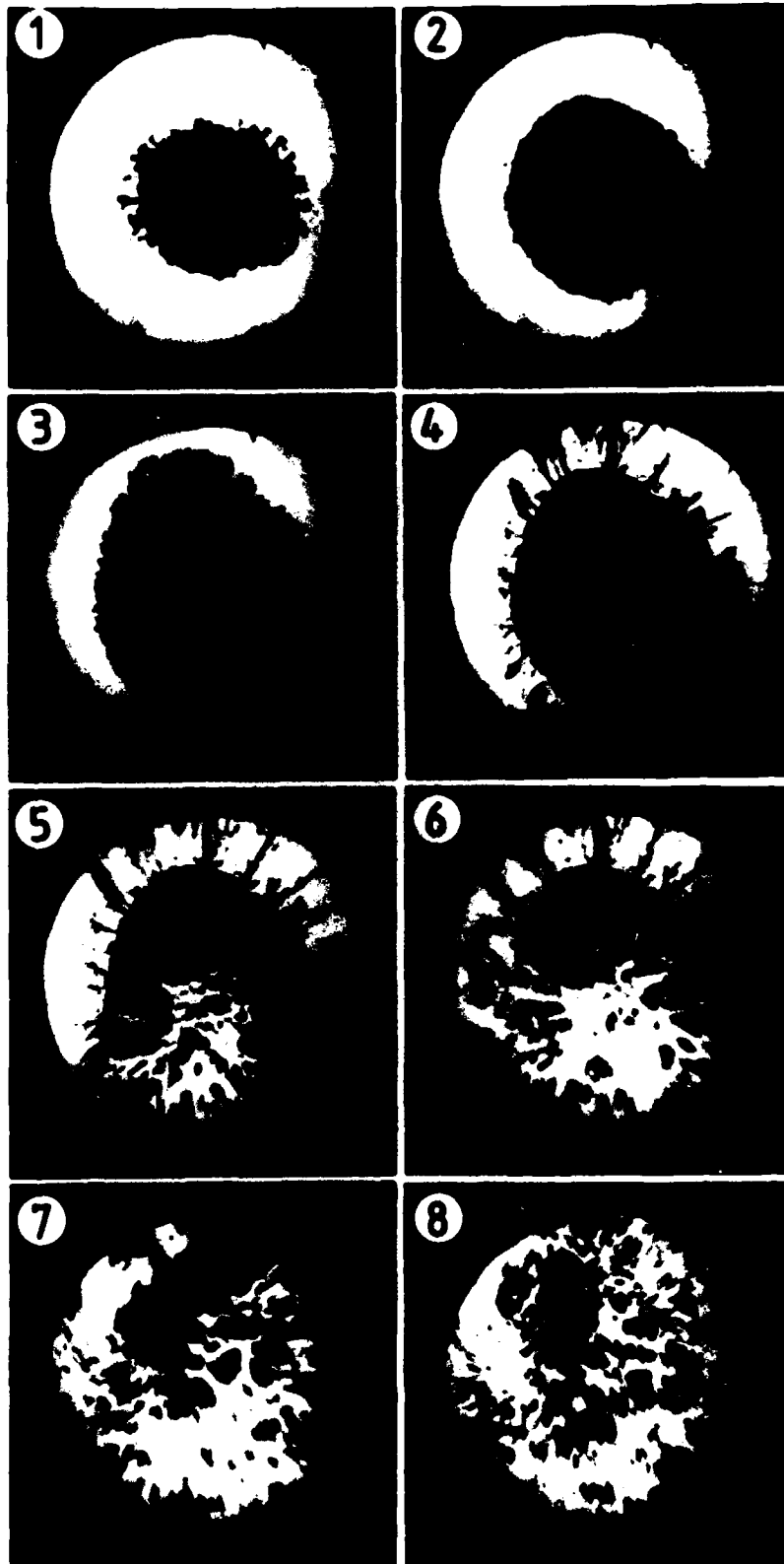




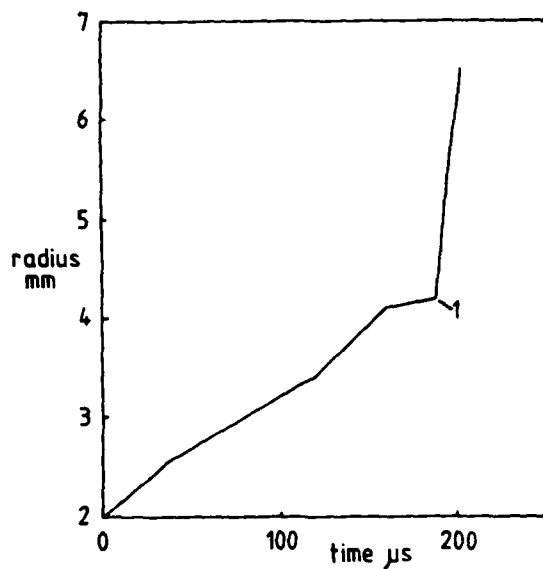
22



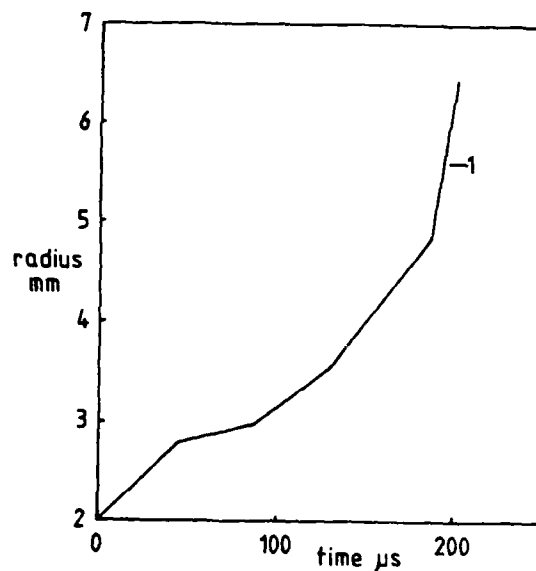
23



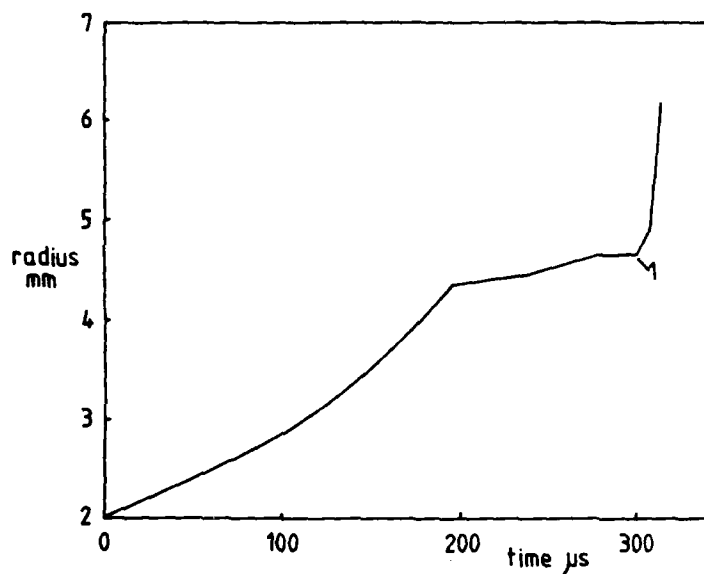
24a



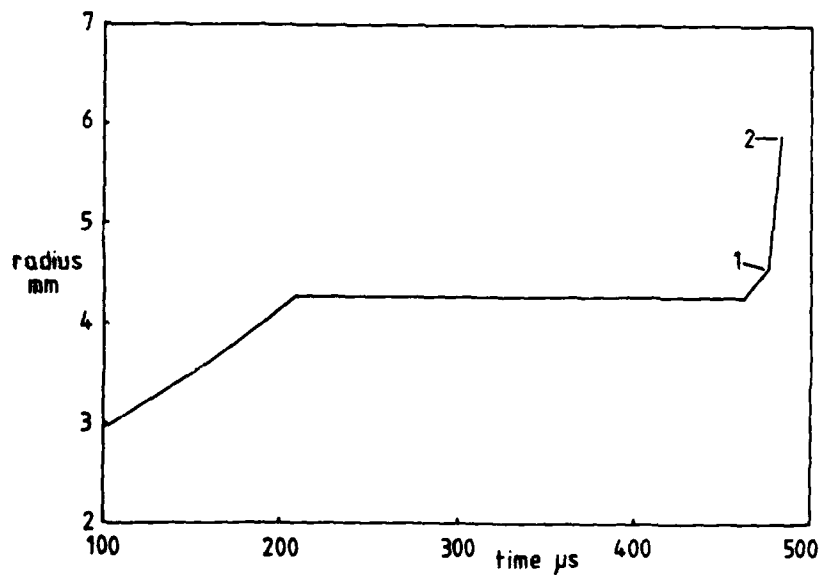
24b



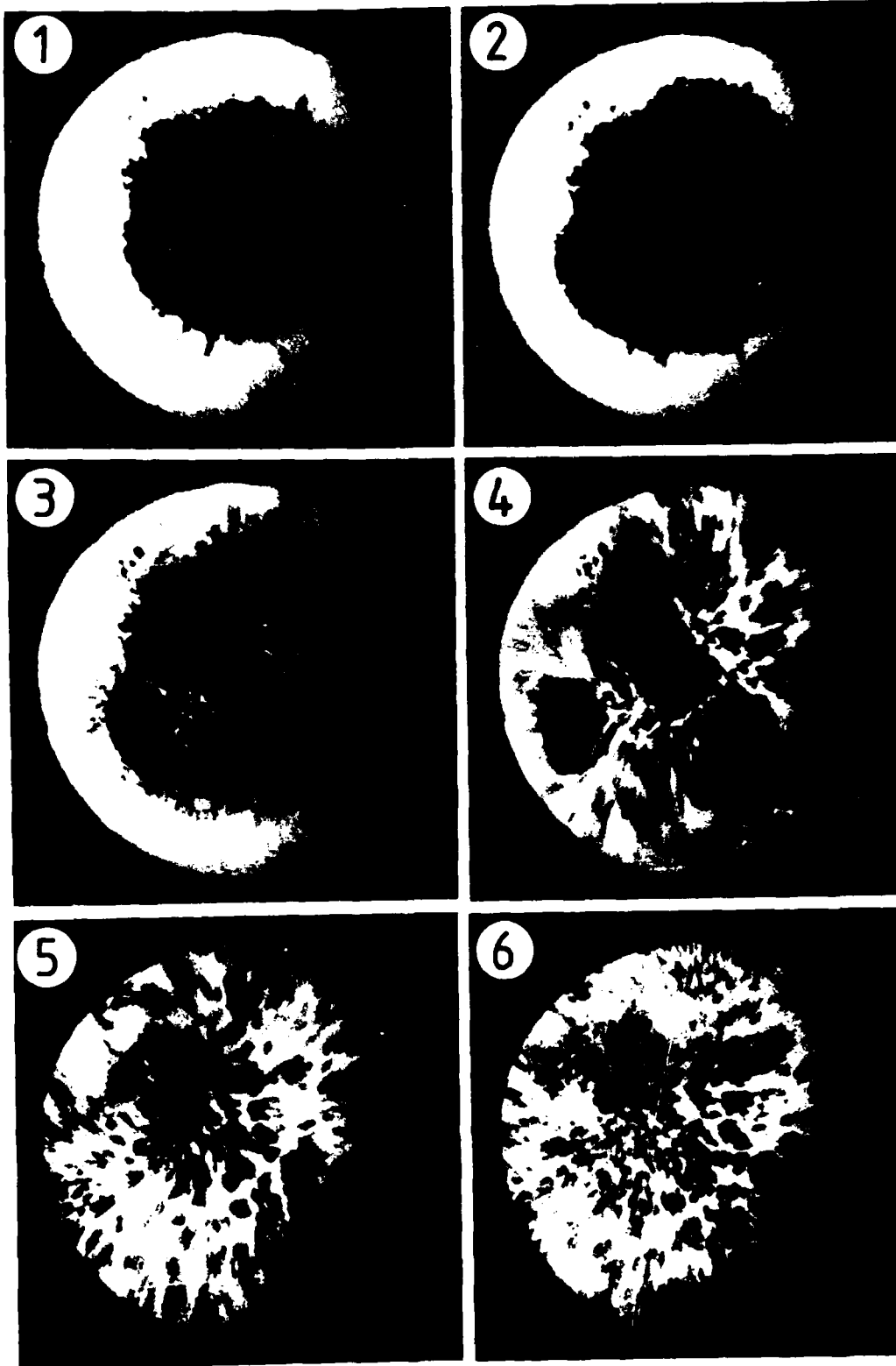
25b



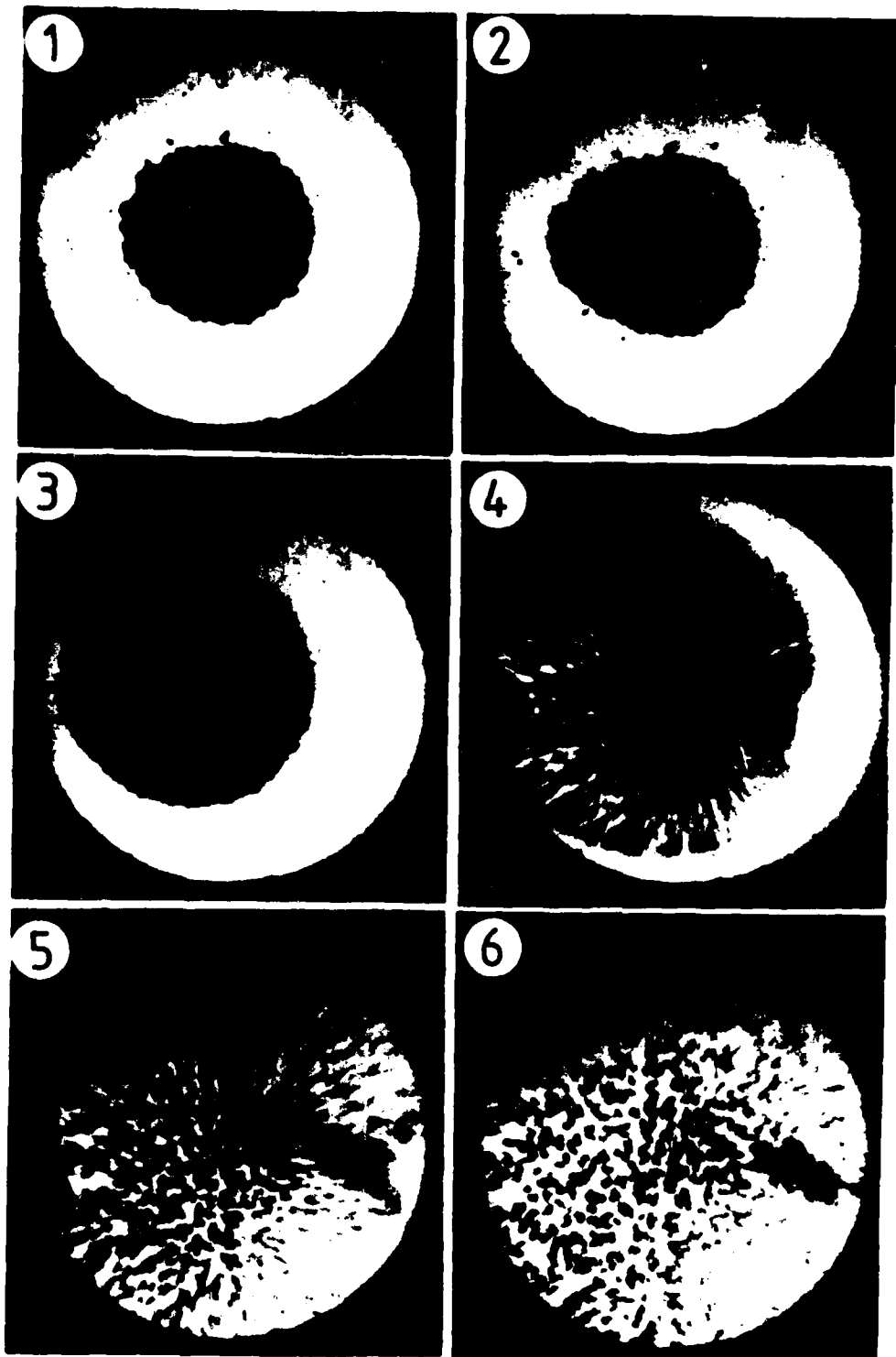
26b

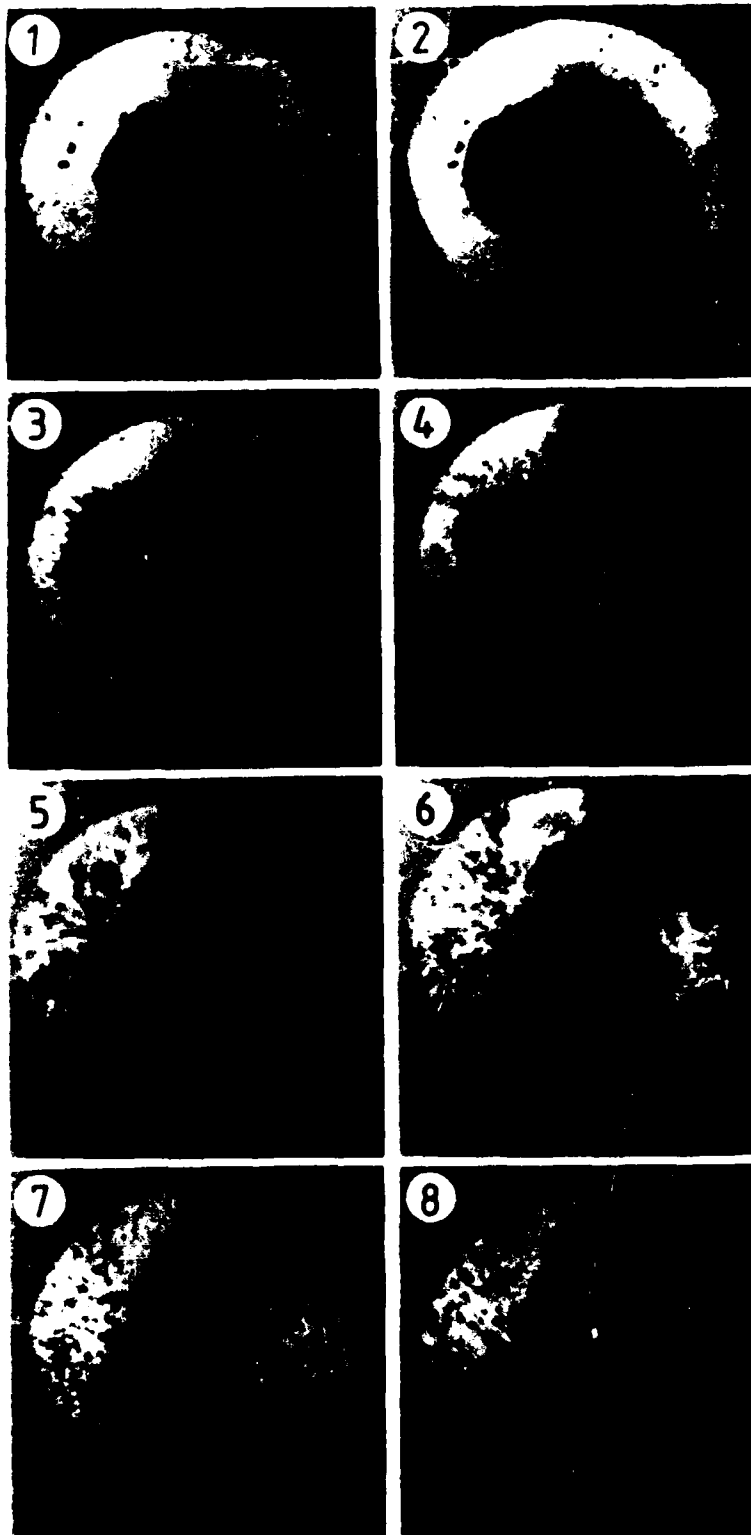


27b

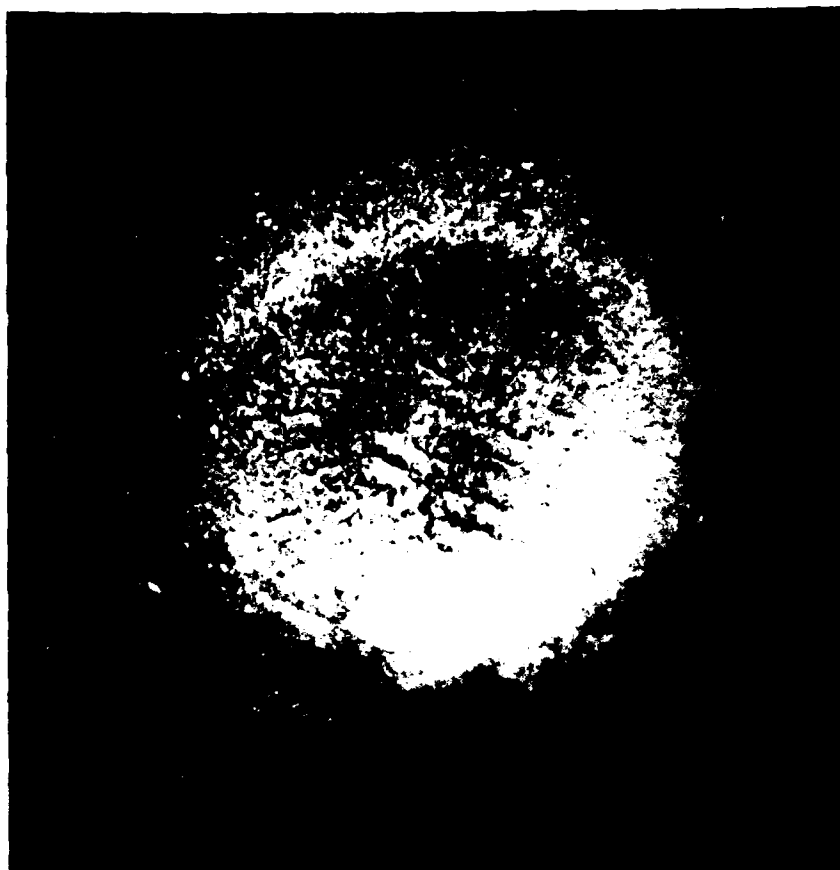


25a



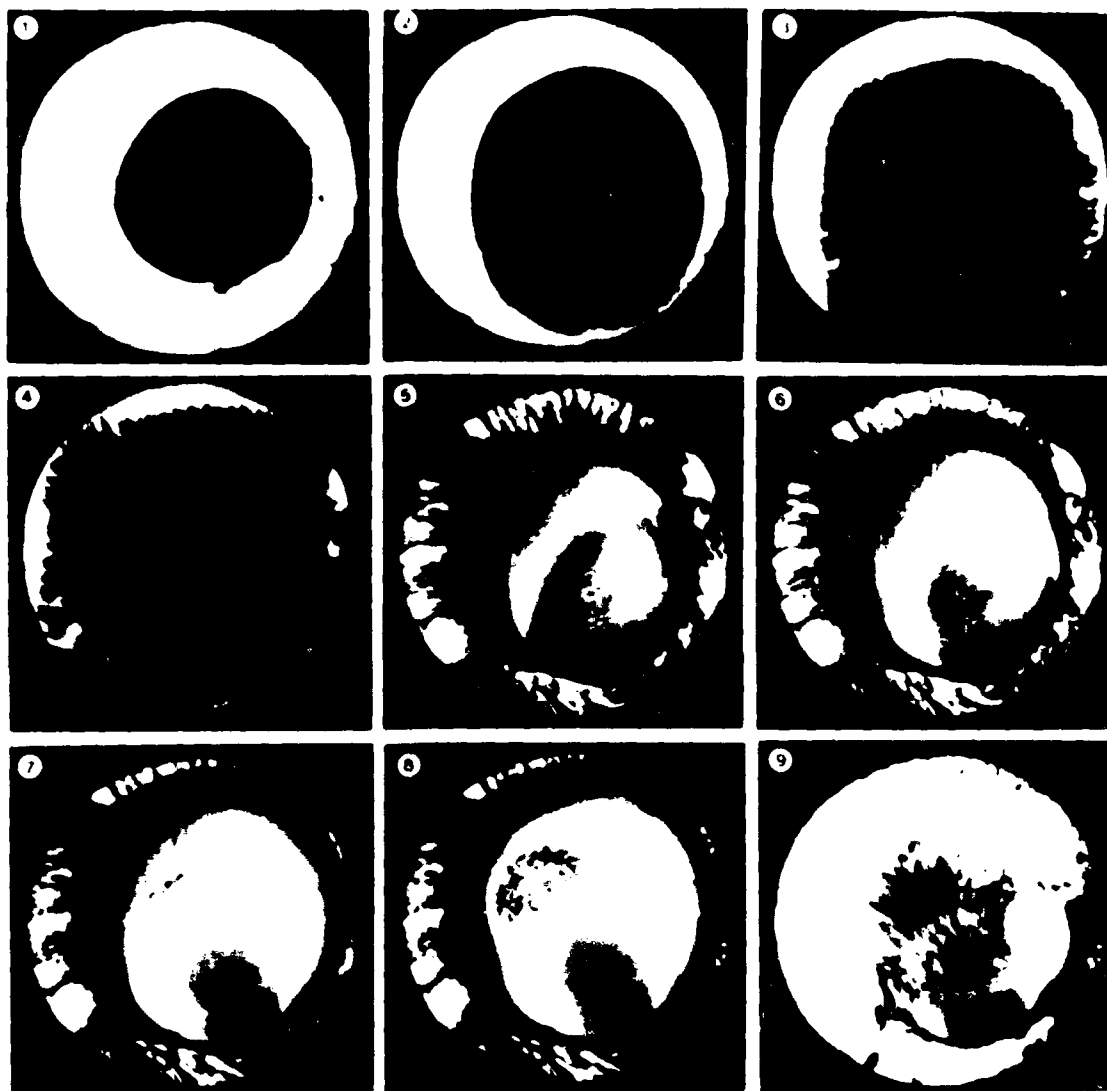


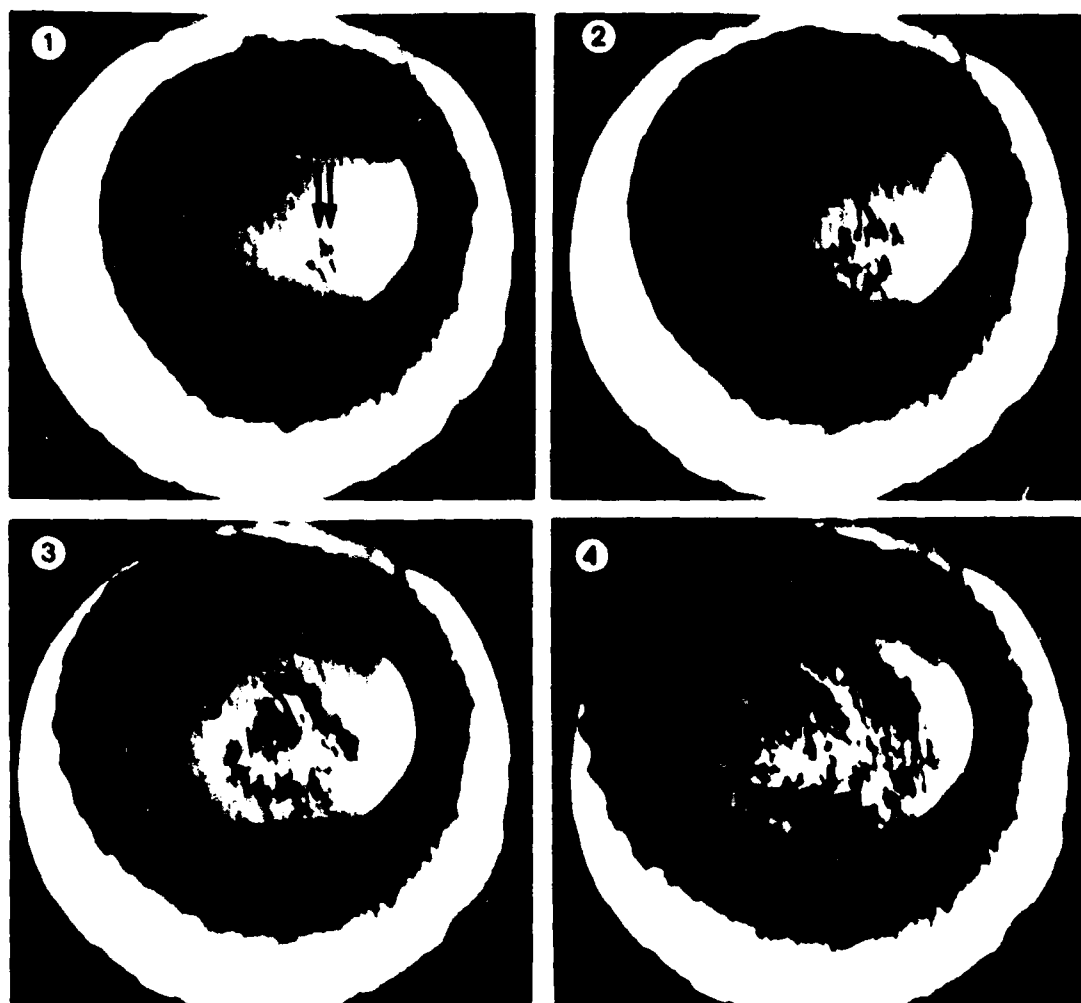
27a



5 mm

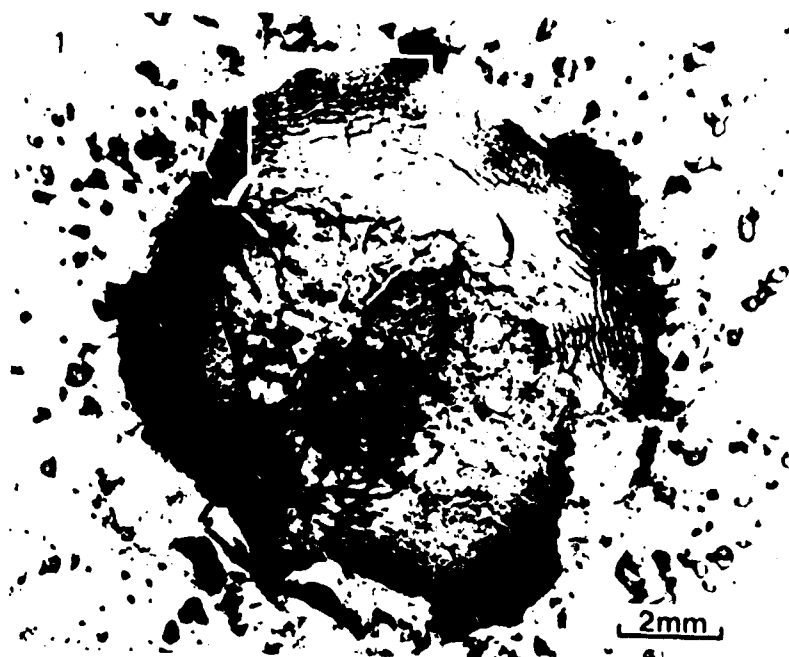
28



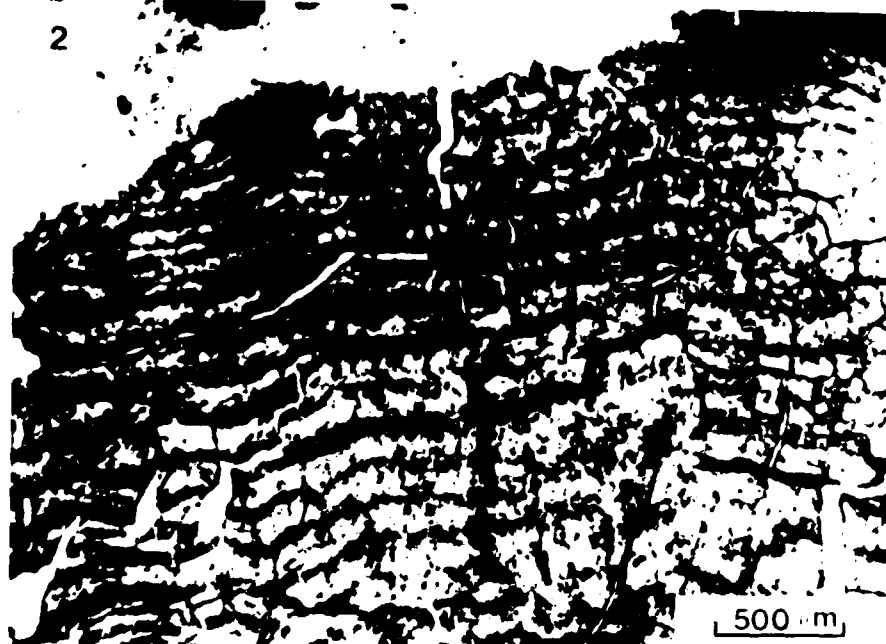


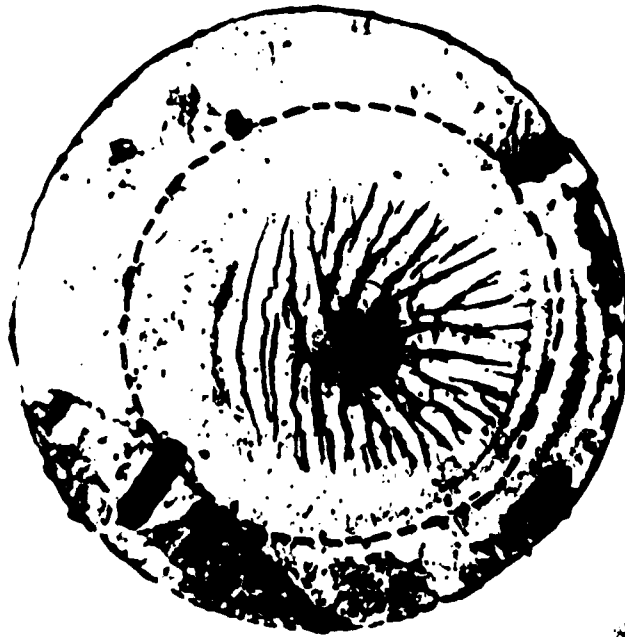


31



2





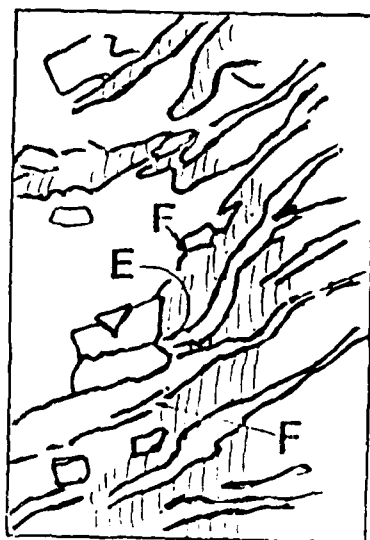
(a)



(b)







36



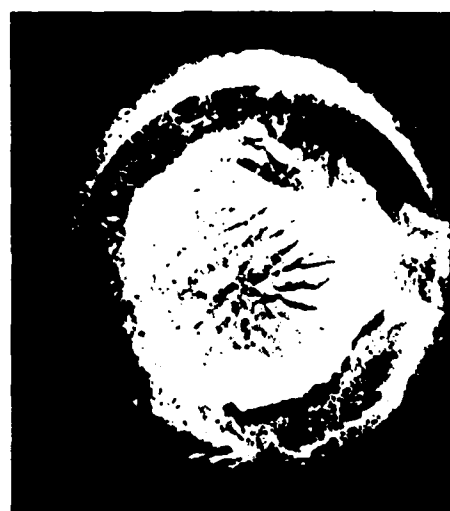
(a)



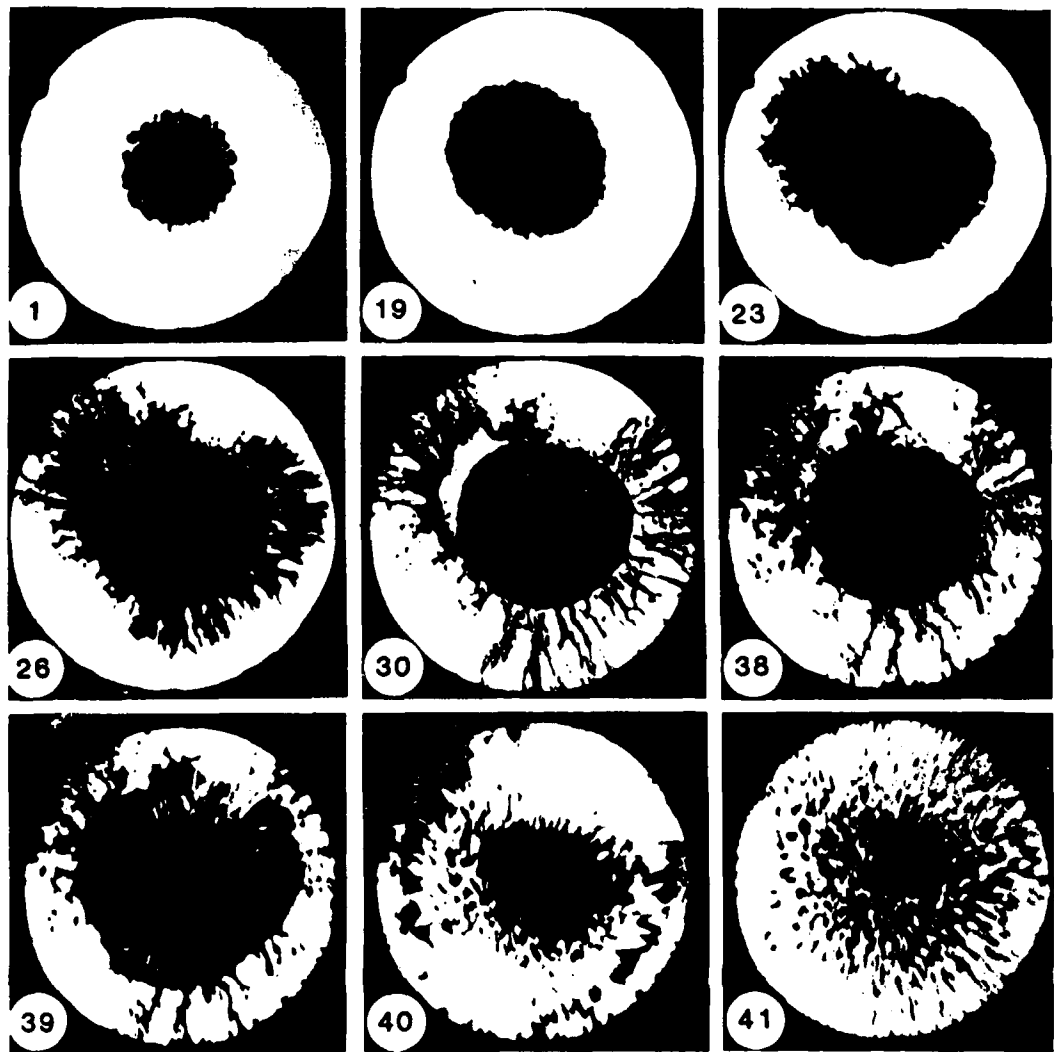
(b)

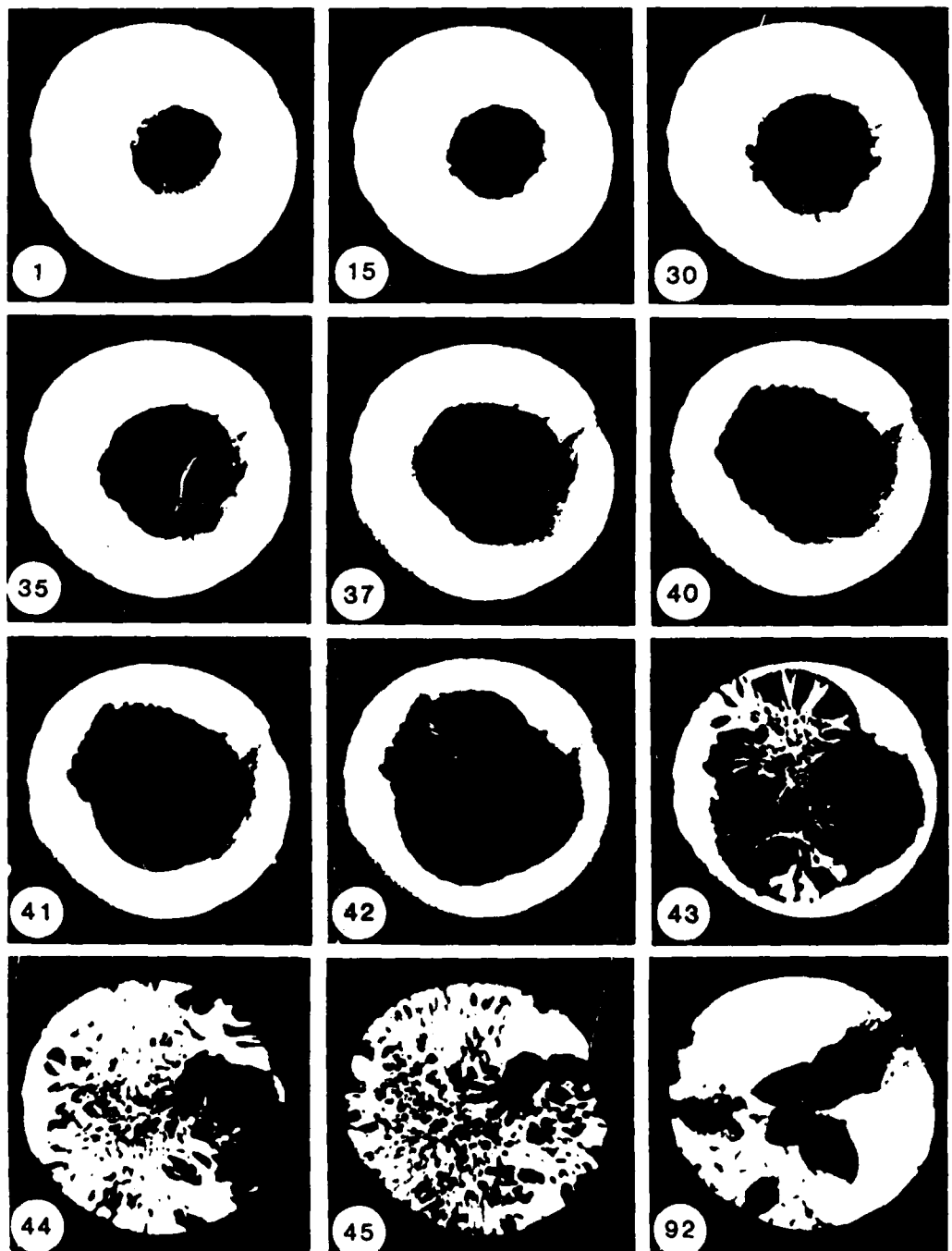


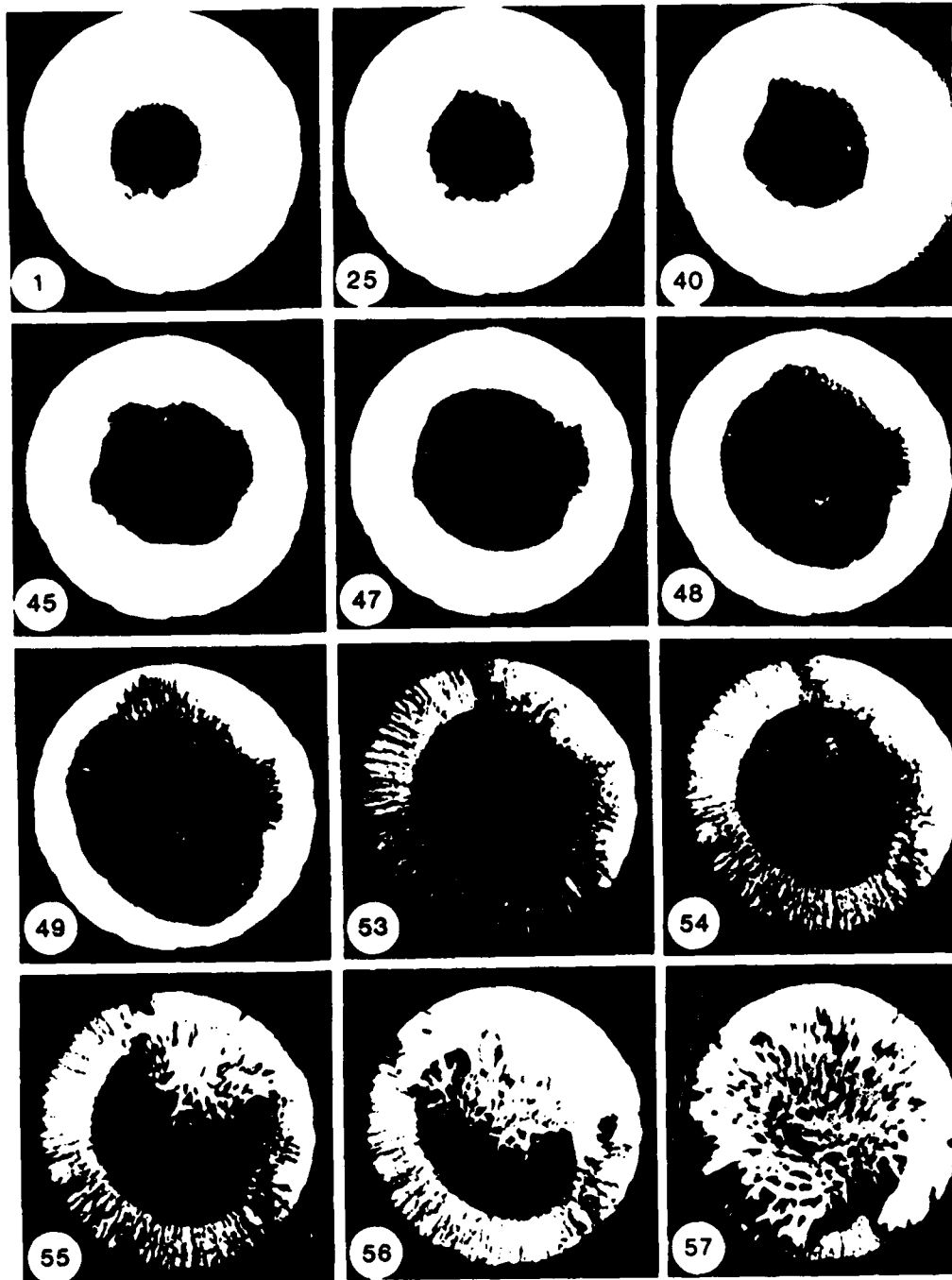
(c)



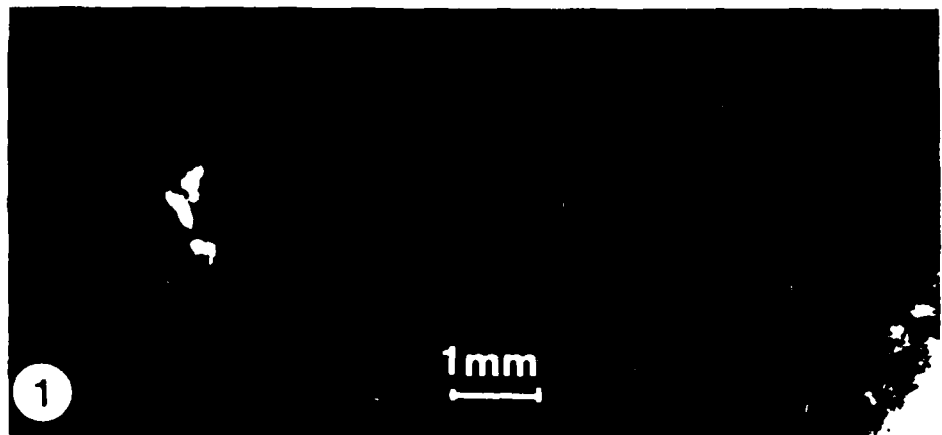
(d)







40





(a)



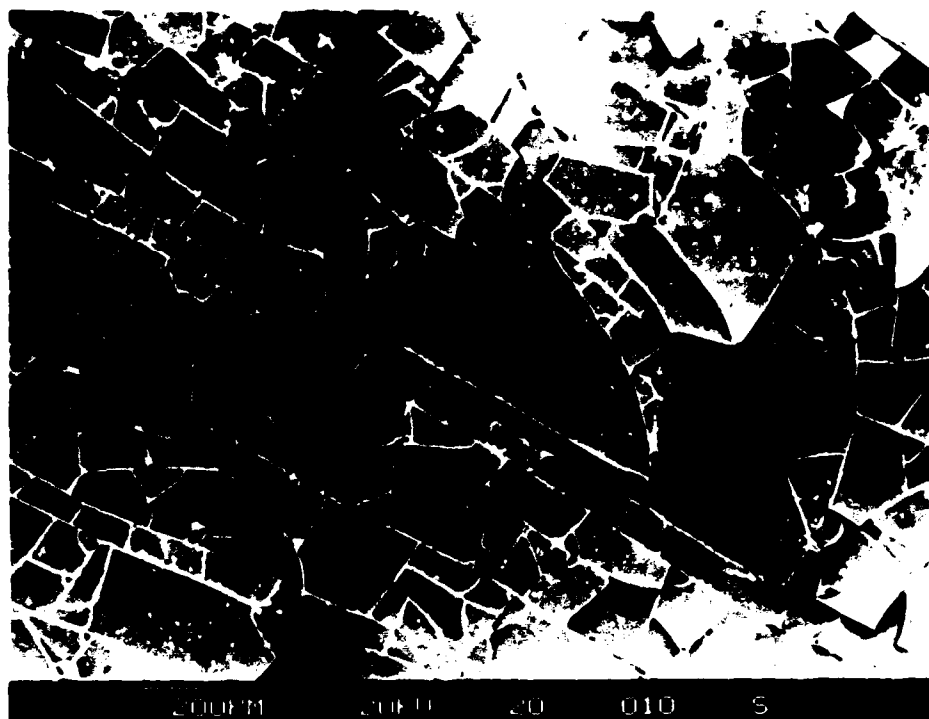
(b)



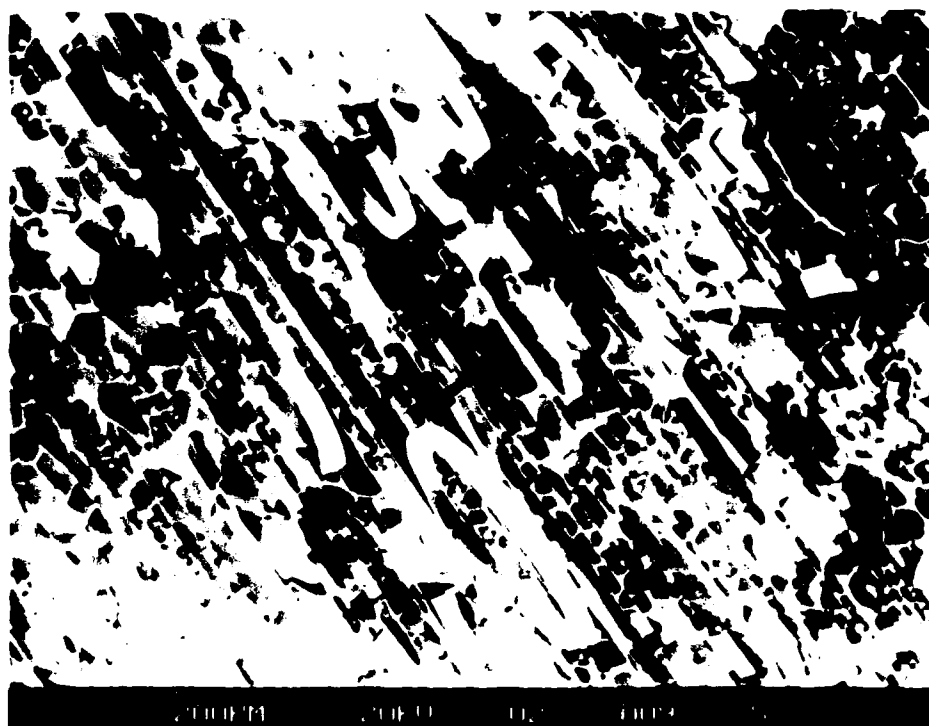
(c)



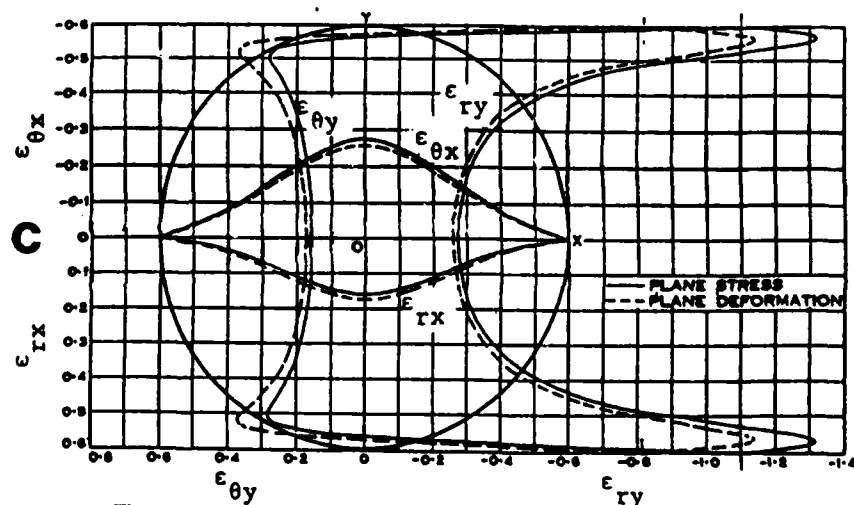
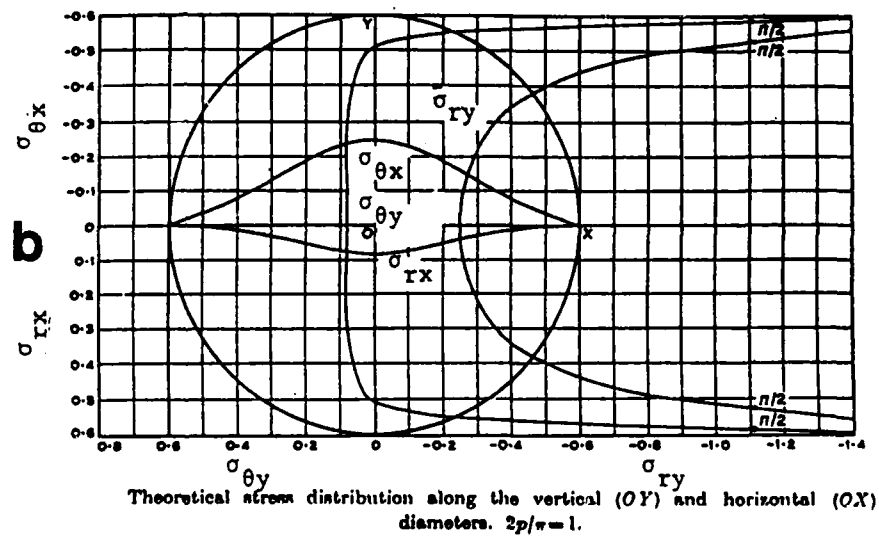
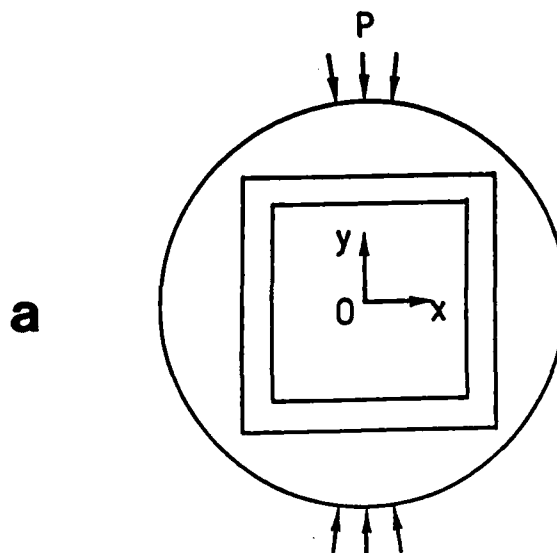
(d)

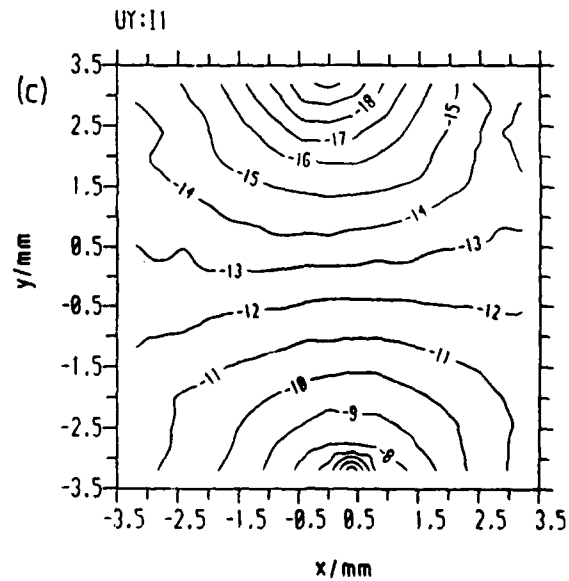
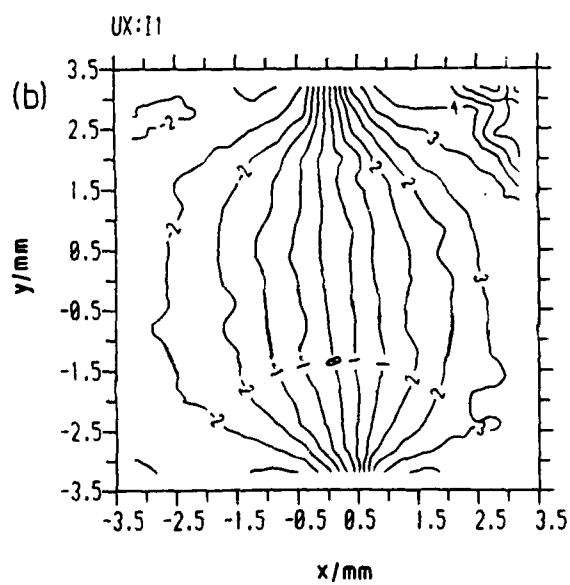
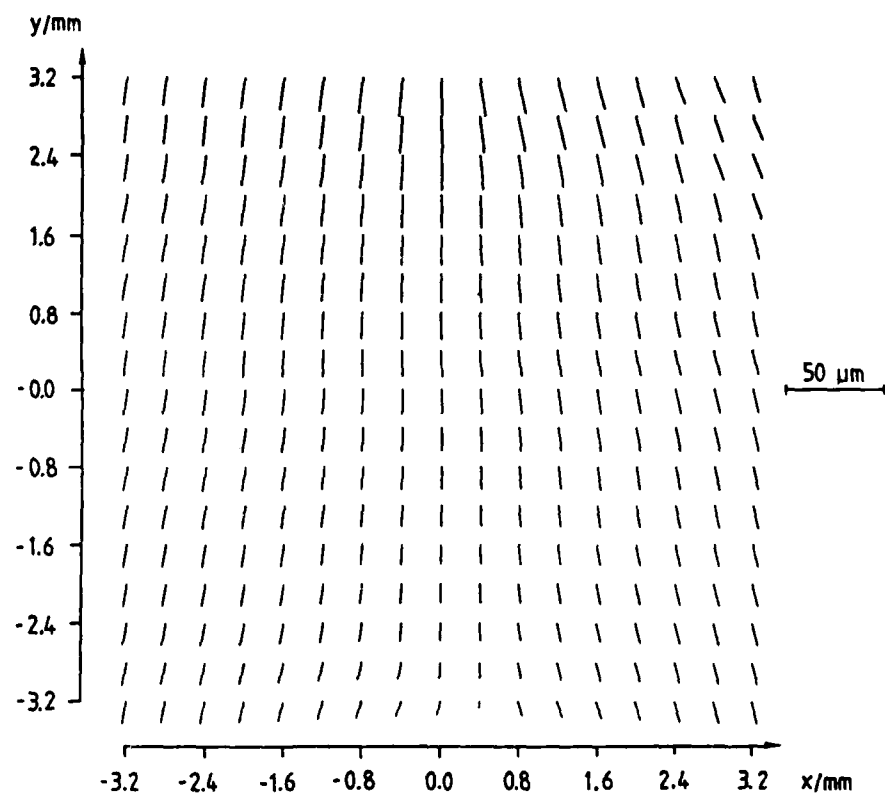


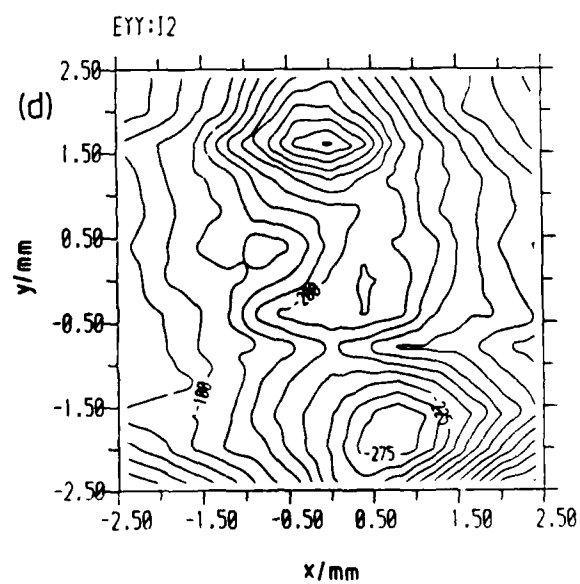
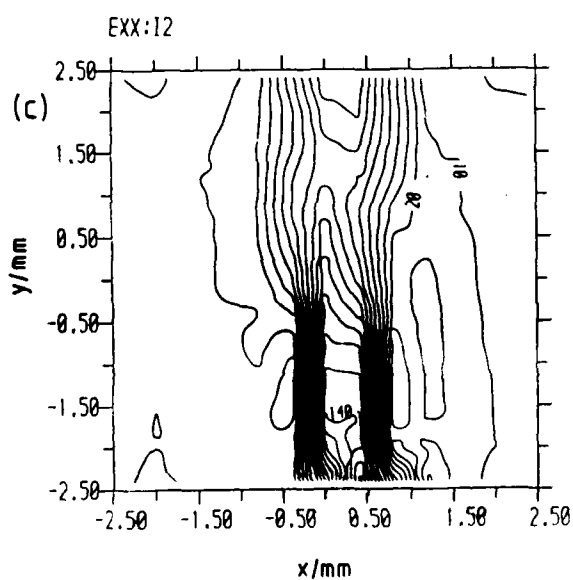
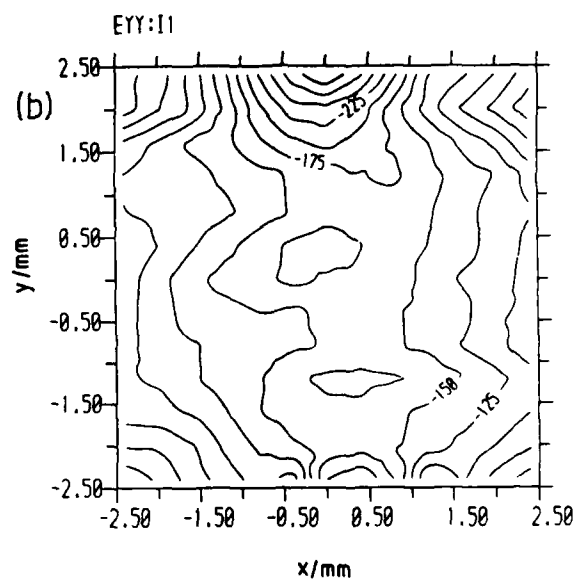
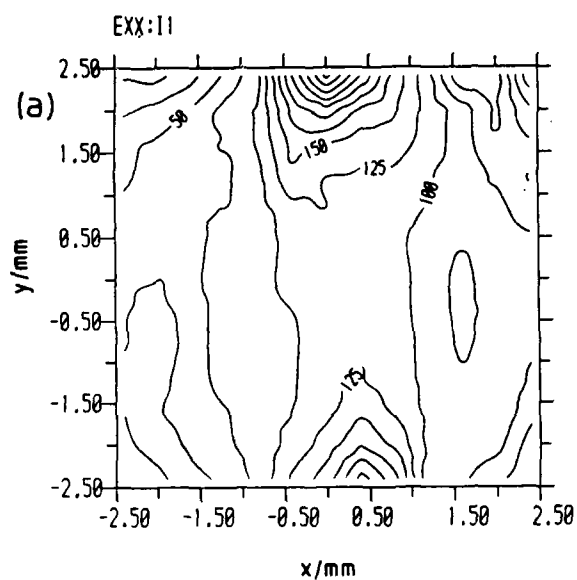
(a)

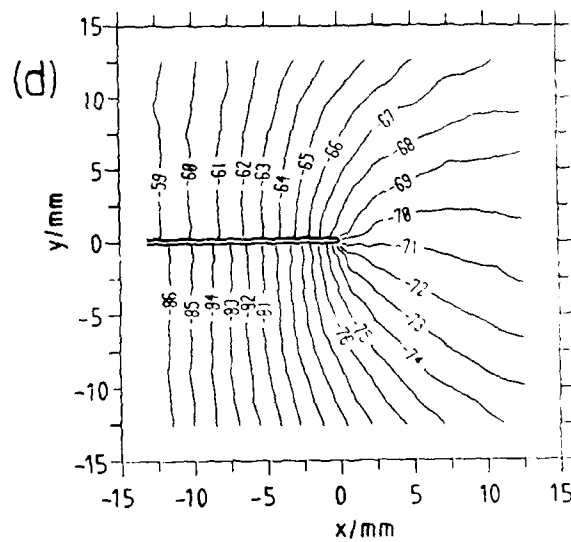
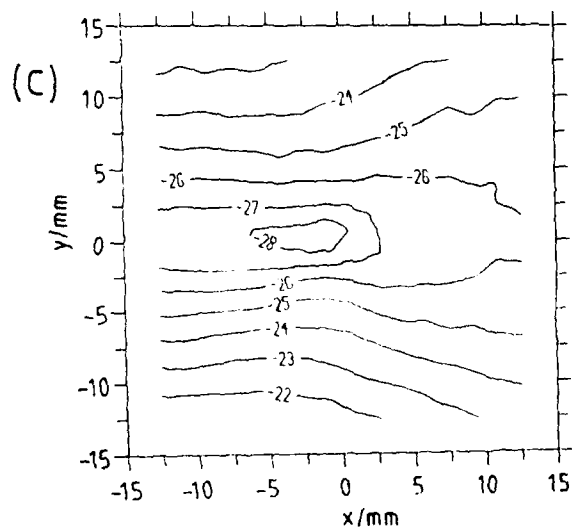
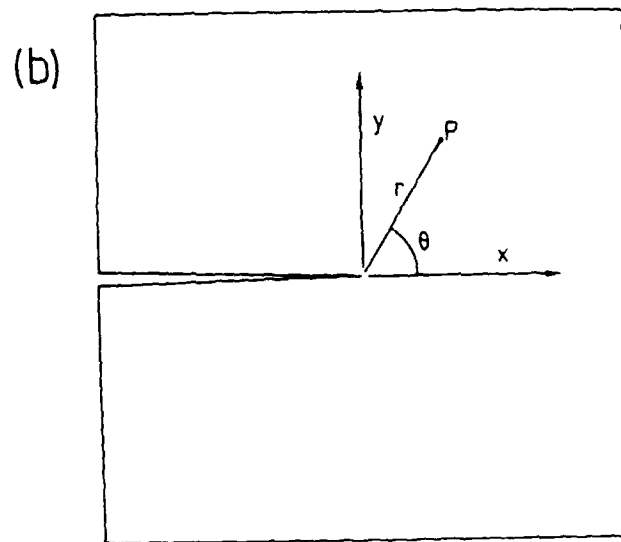
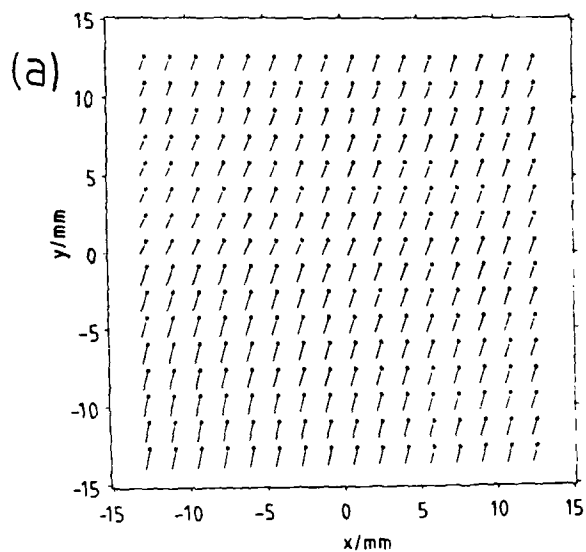


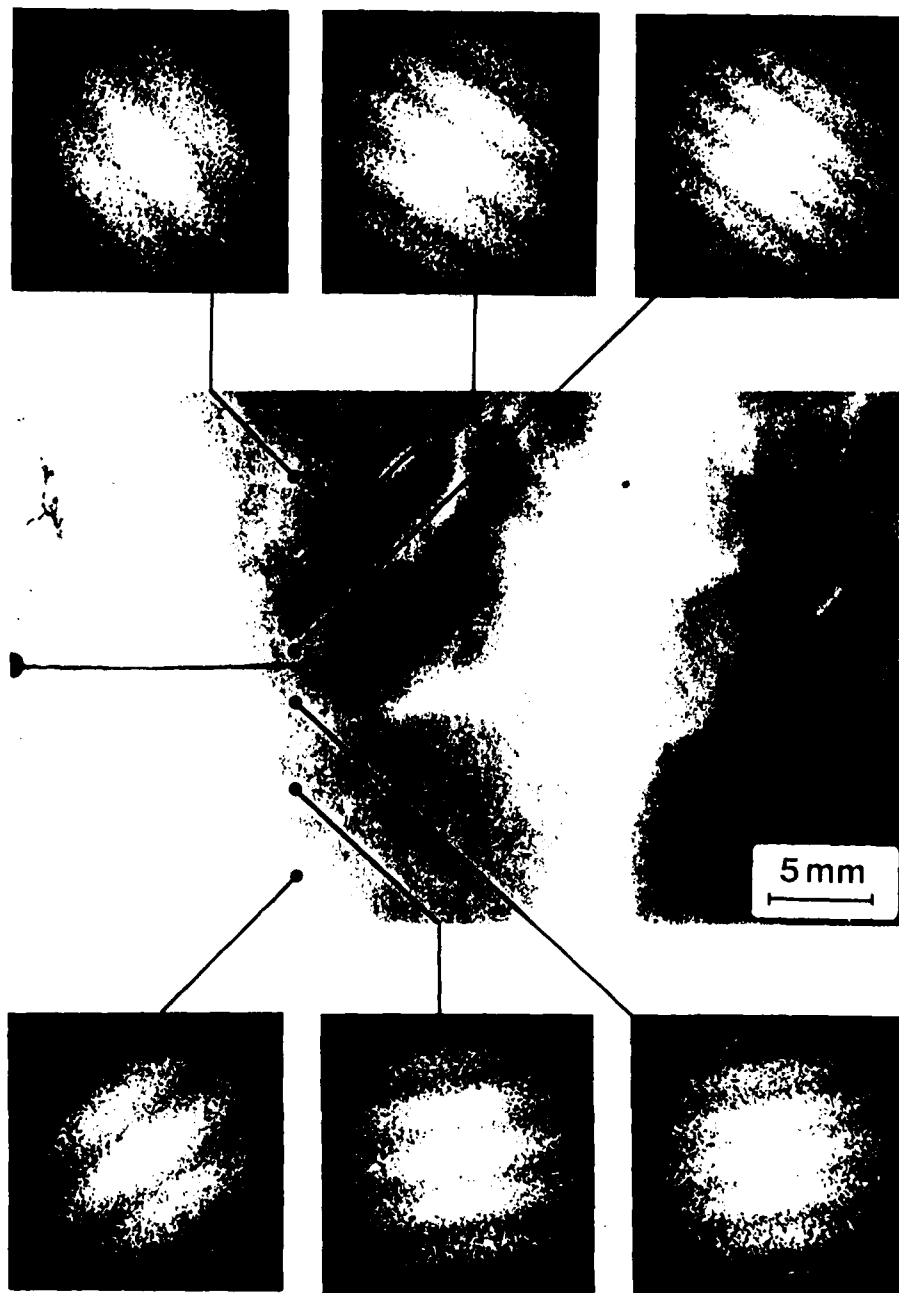
(b)



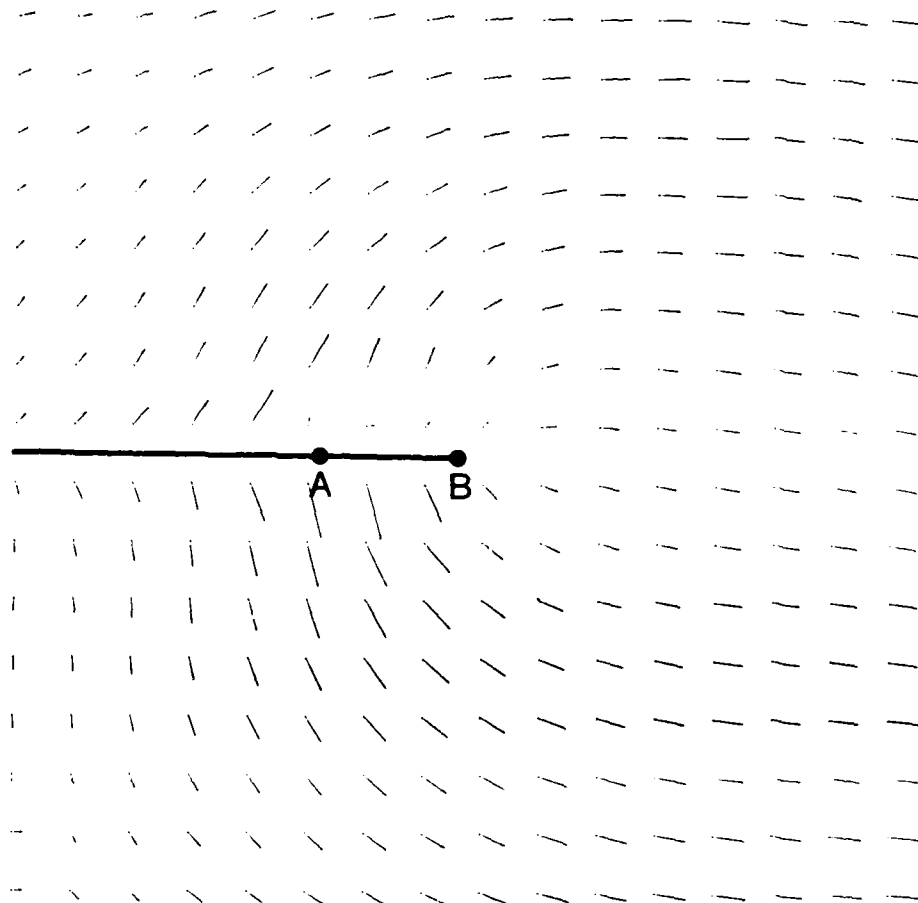


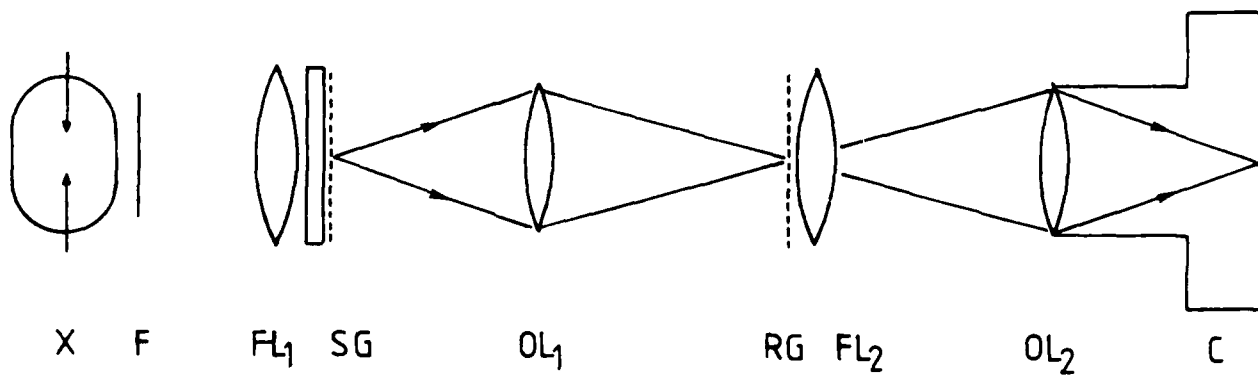


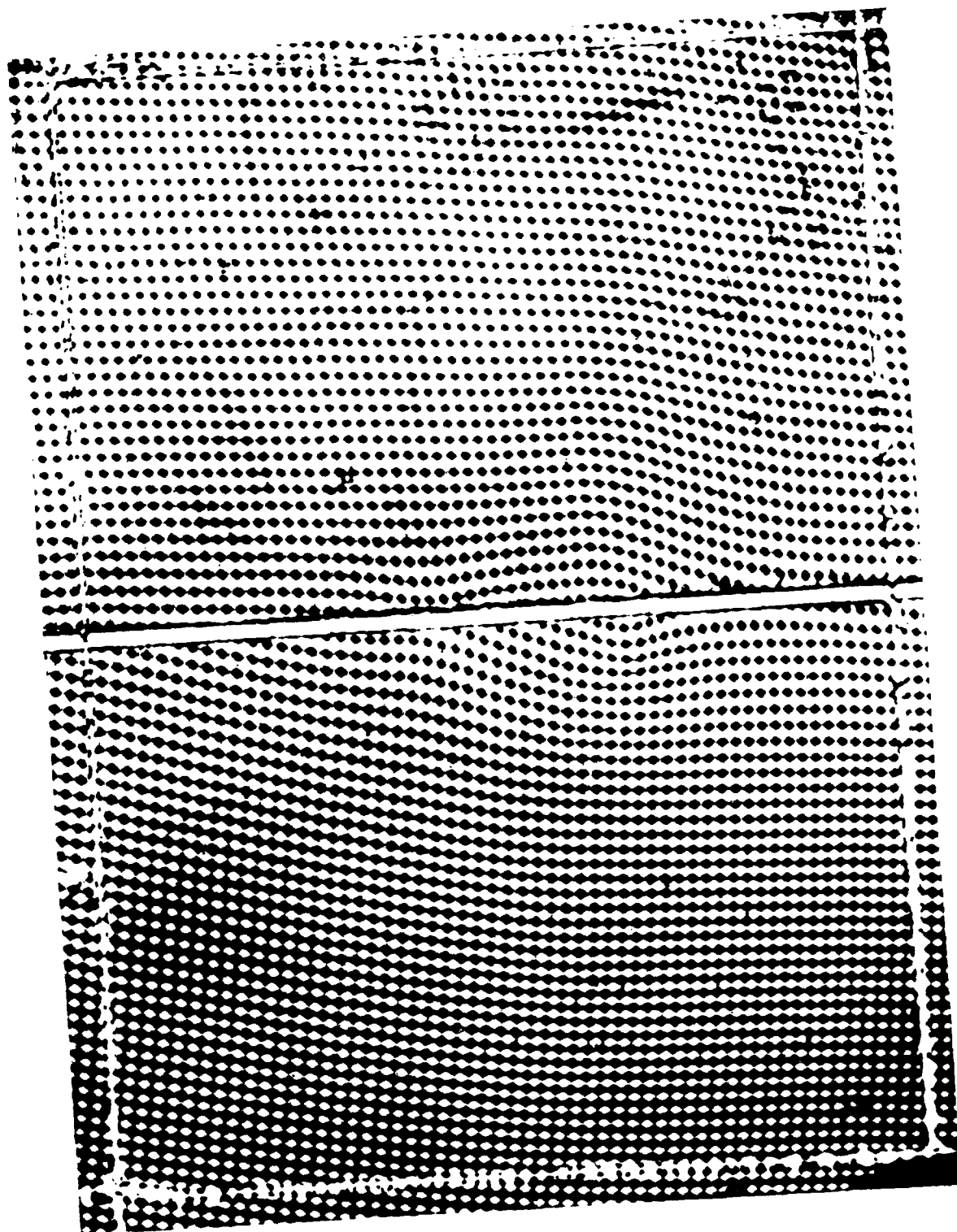




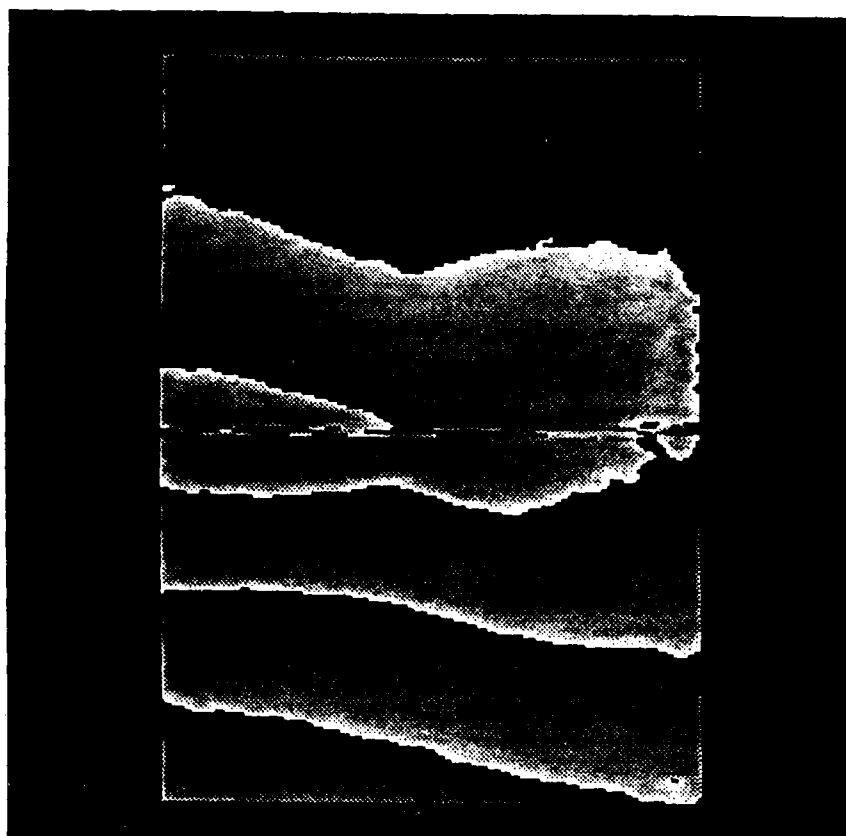
53



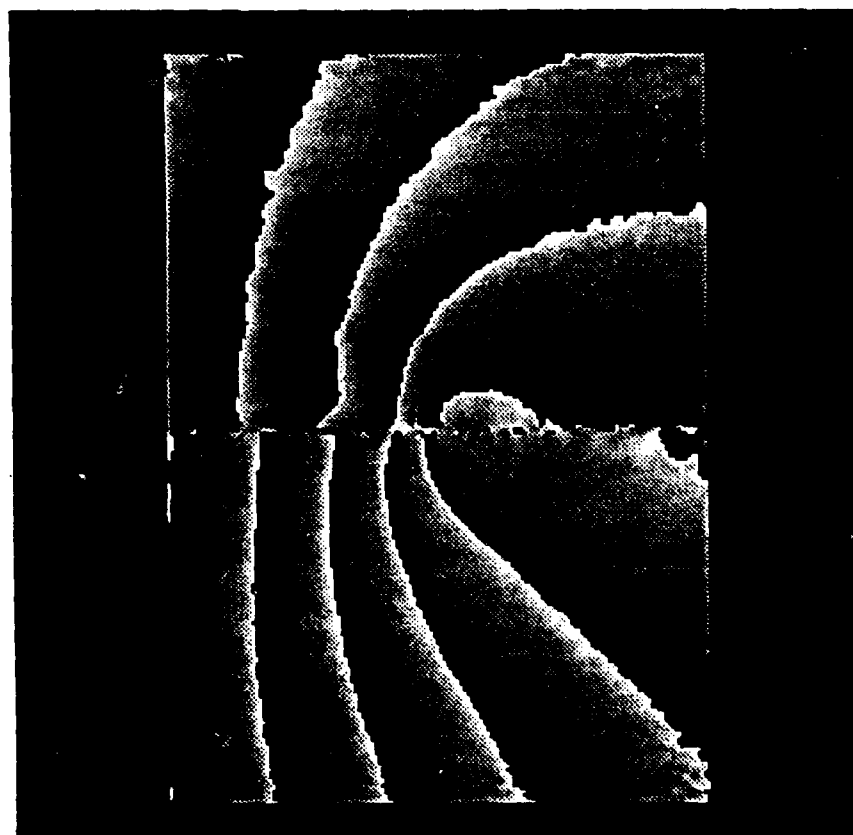


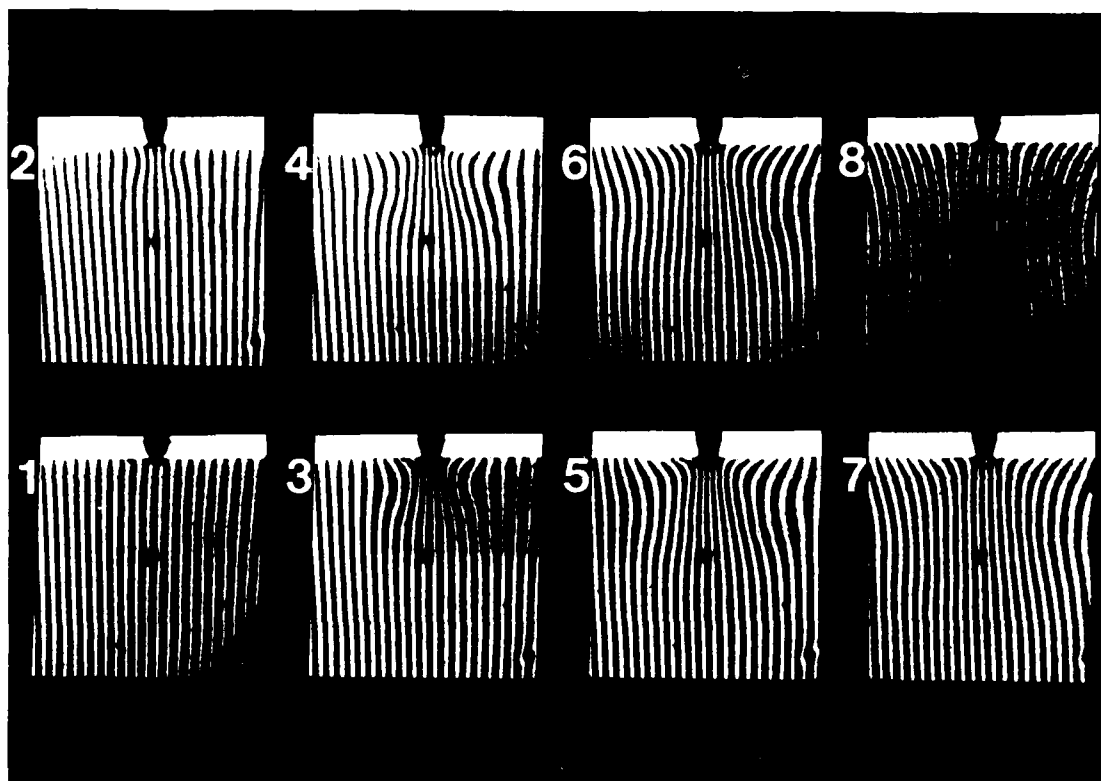


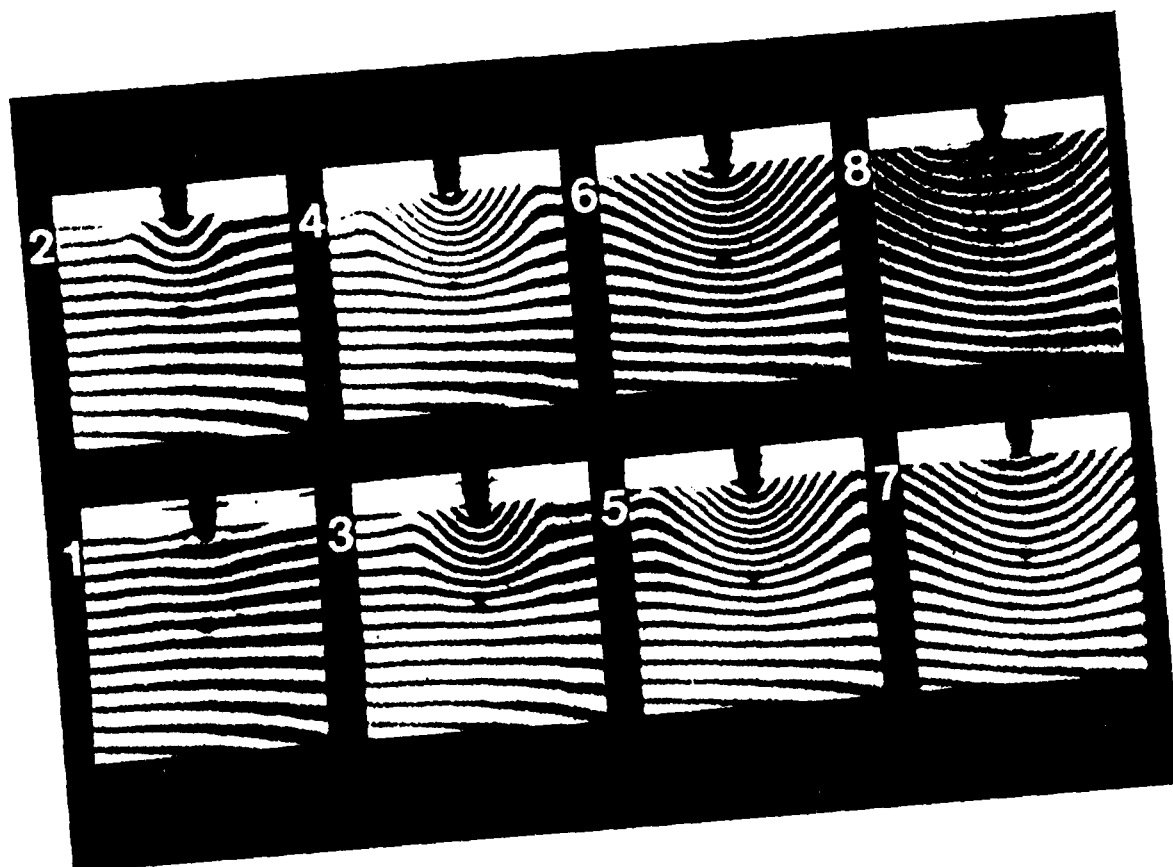
(a)

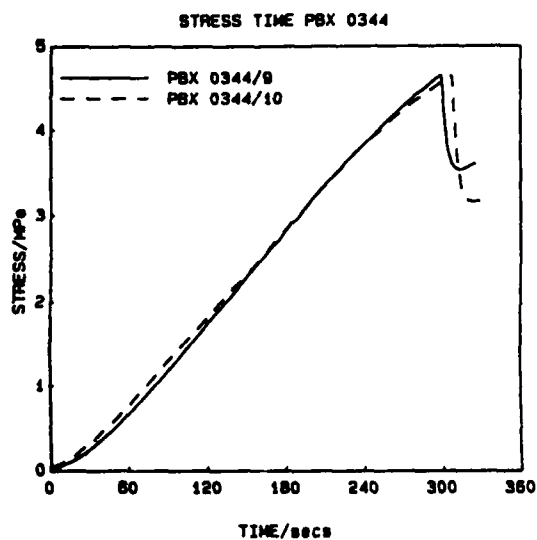


(b)

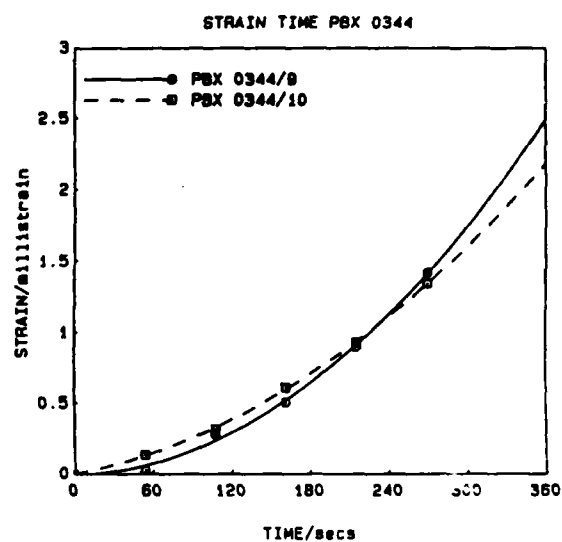




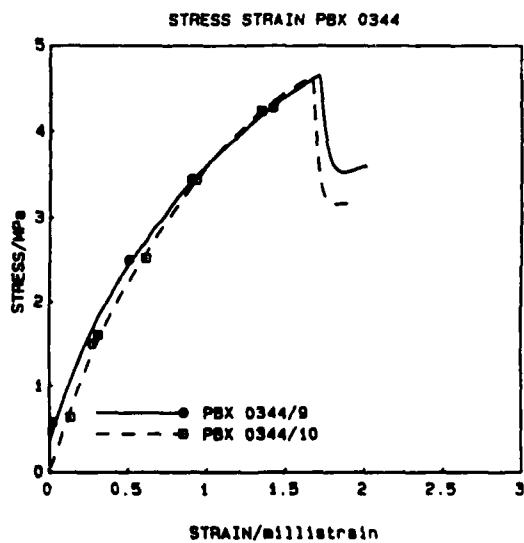




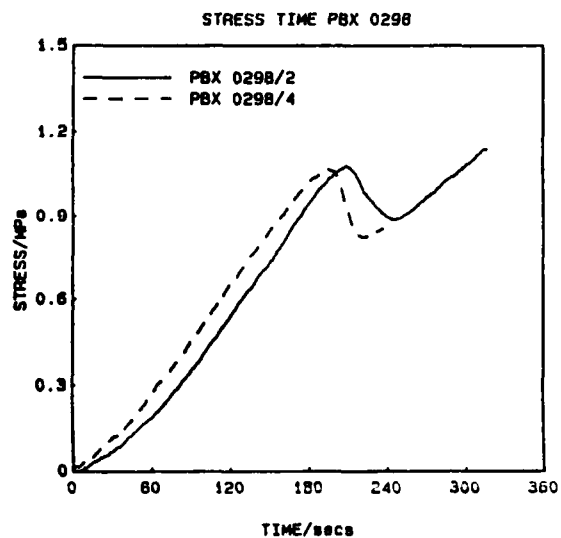
a



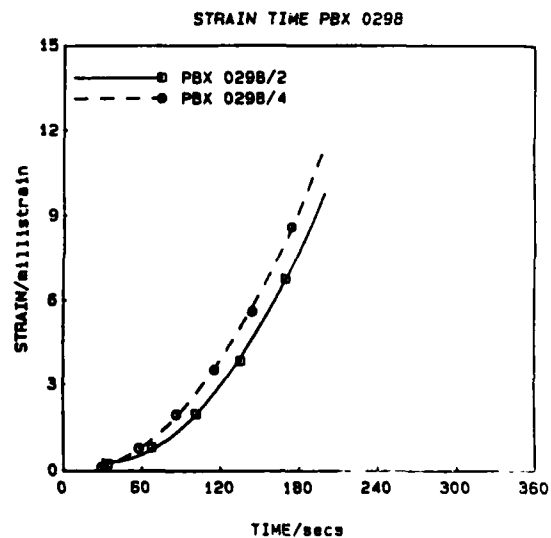
b



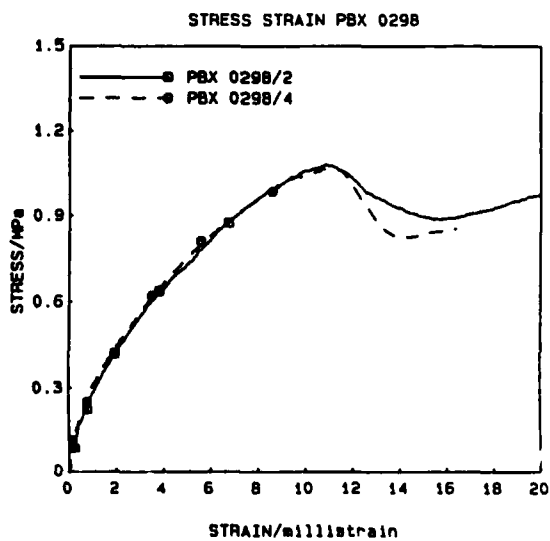
c



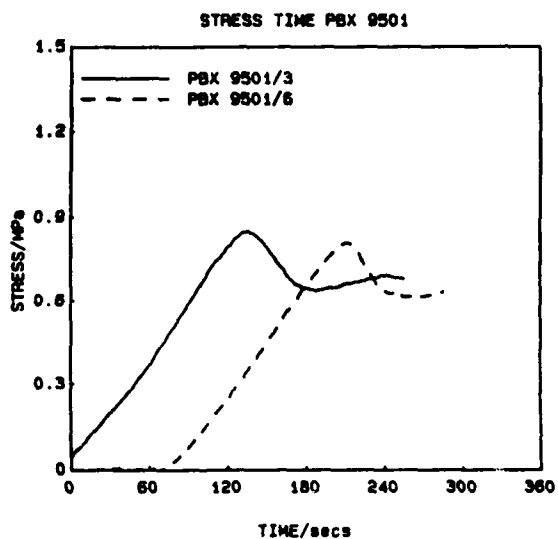
a



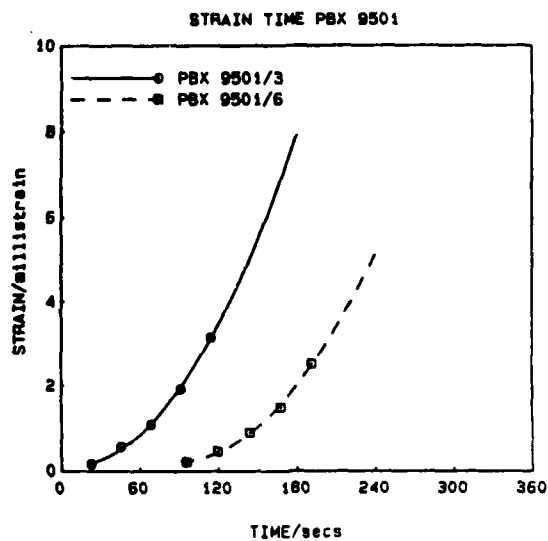
b



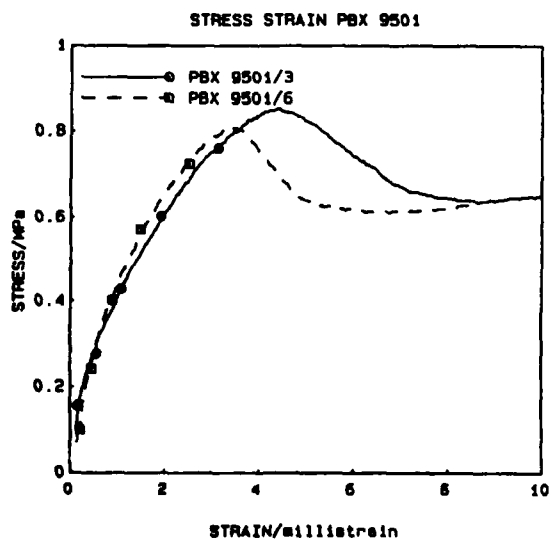
c



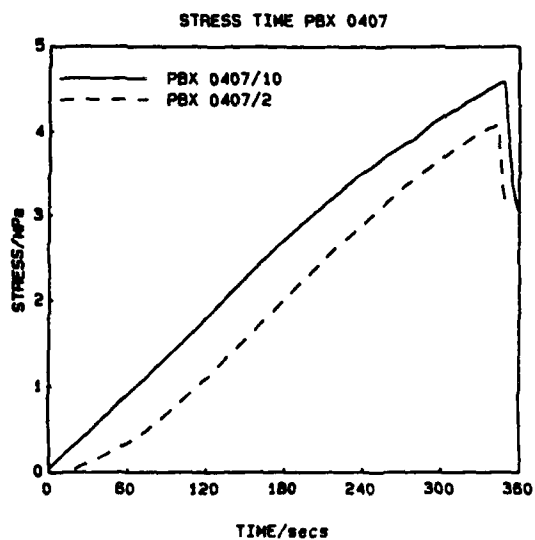
a



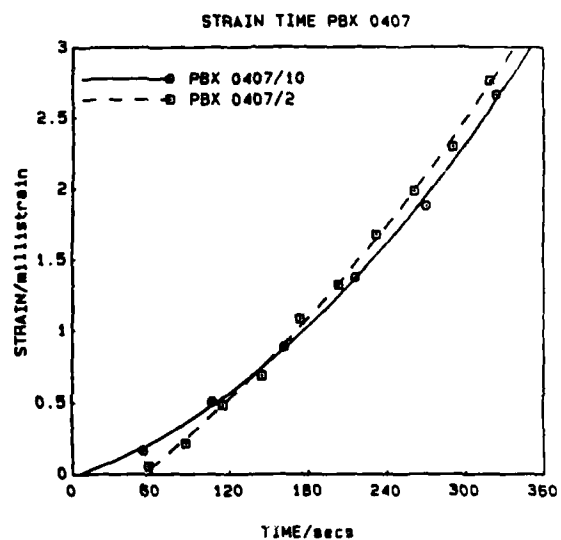
b



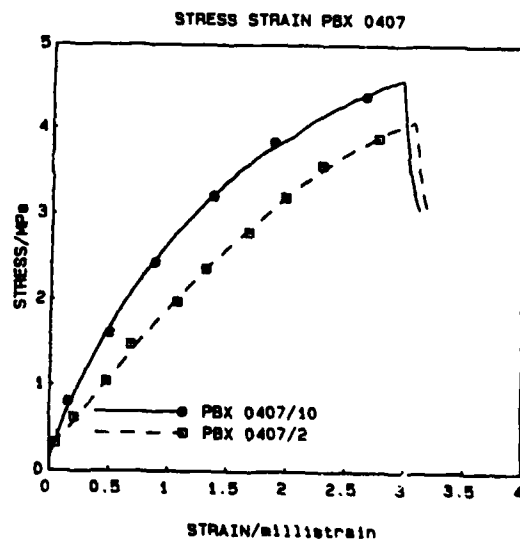
c



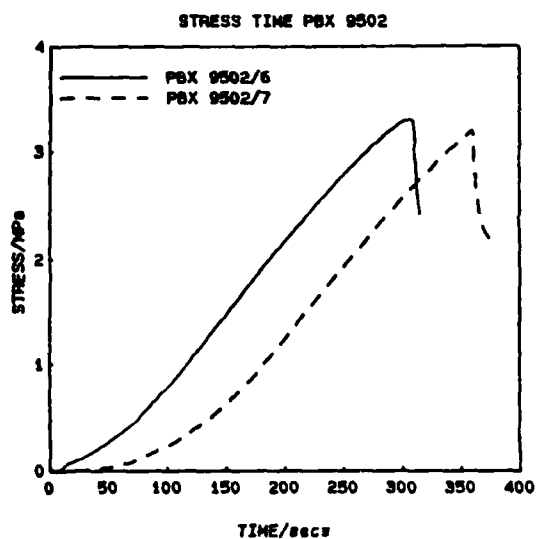
a



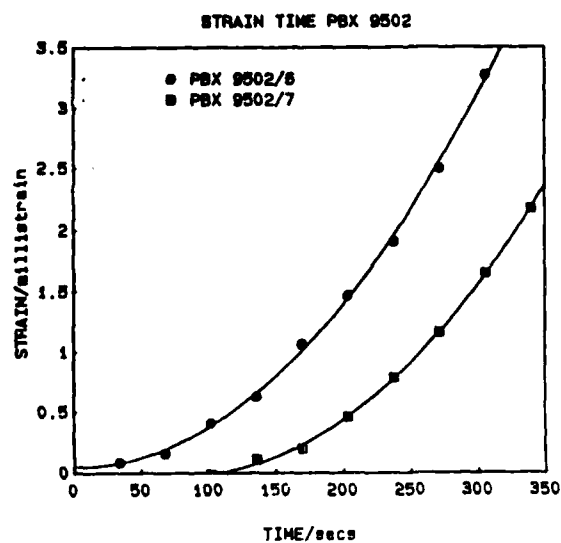
b



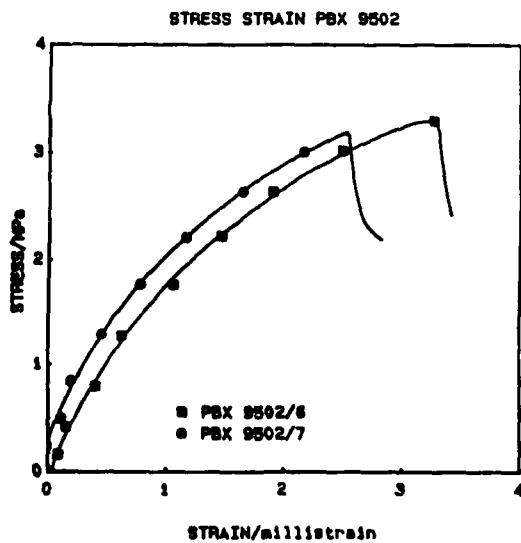
c



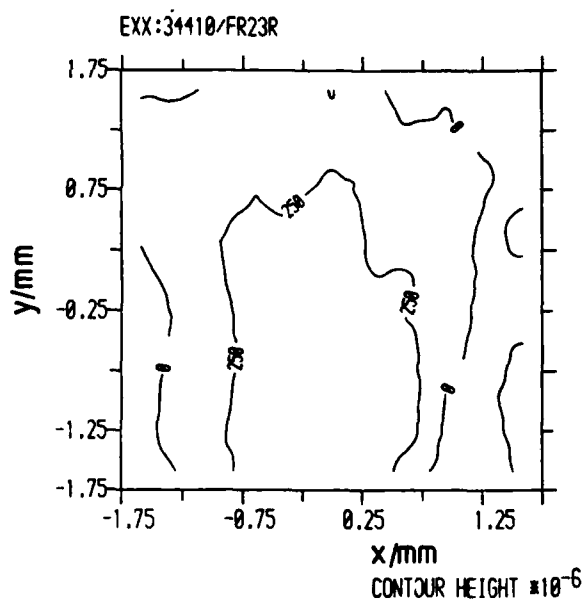
a



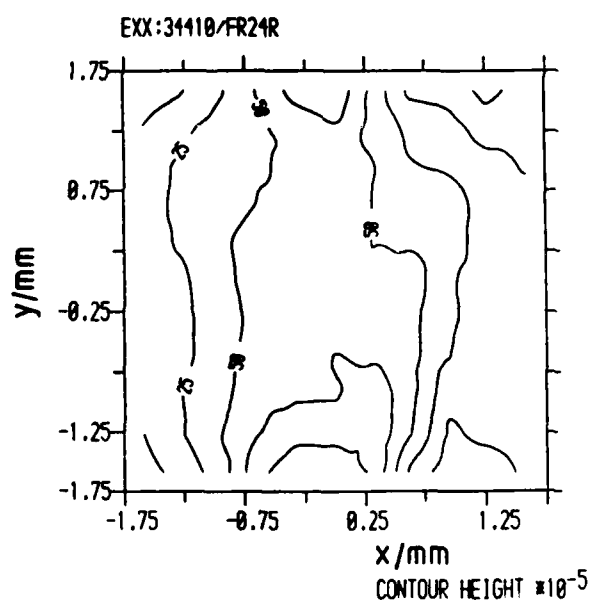
b



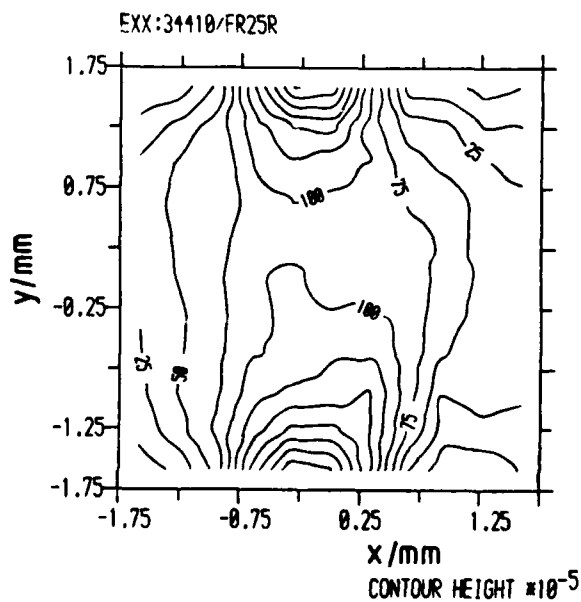
c



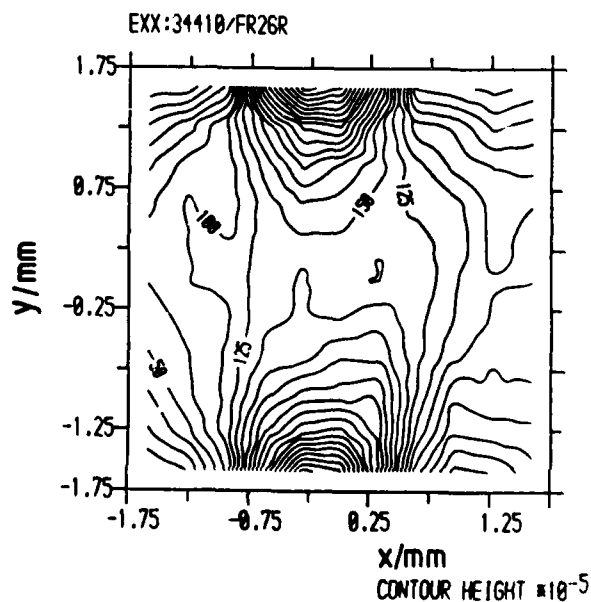
a



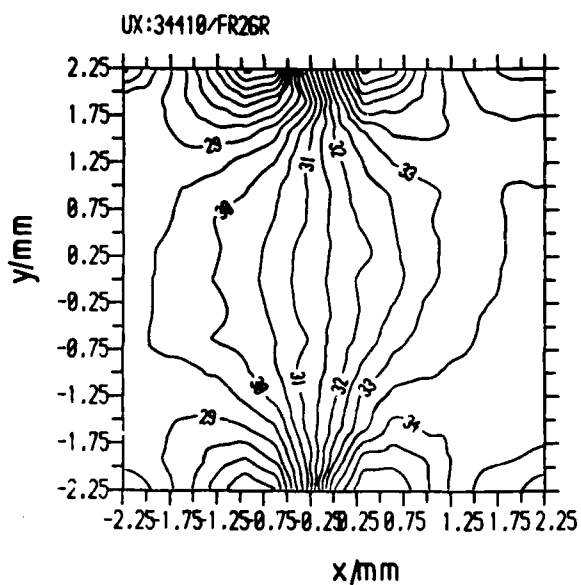
b



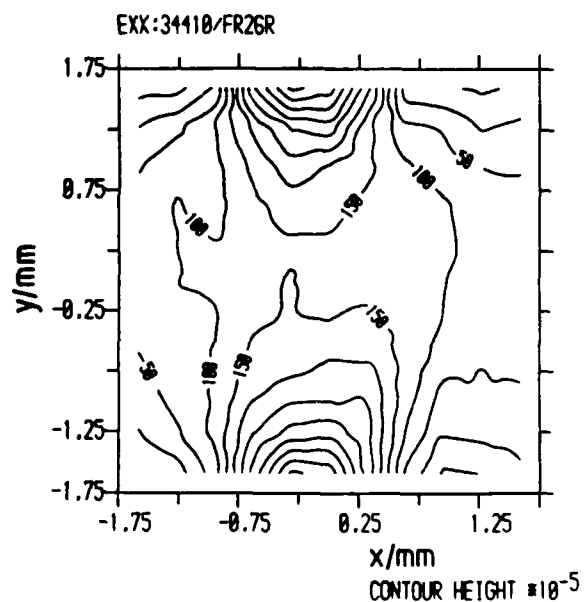
c



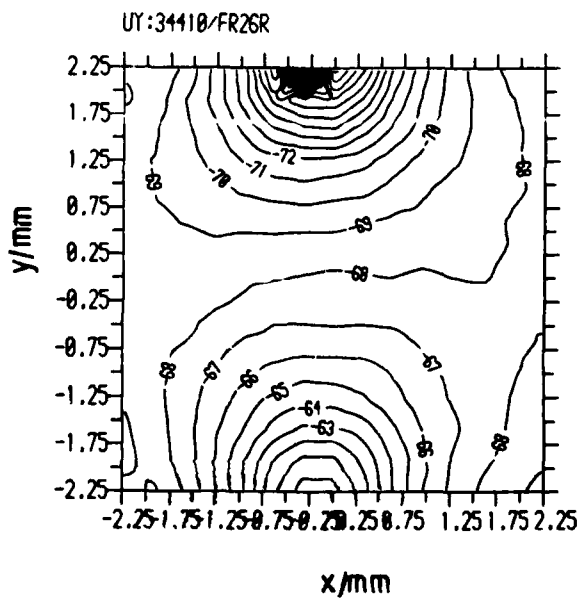
d



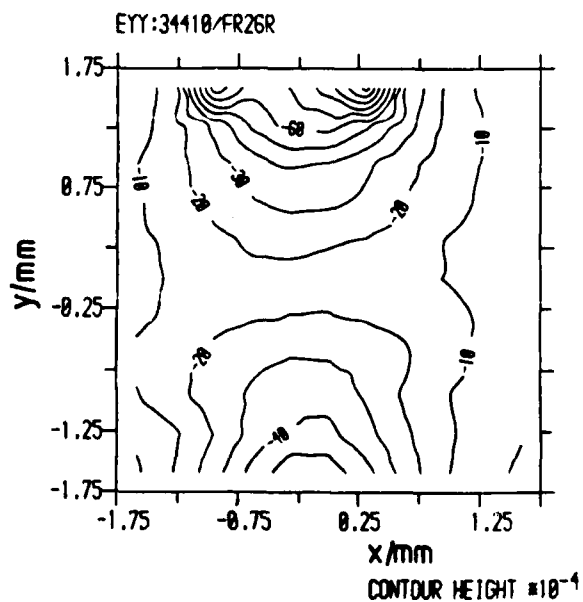
a



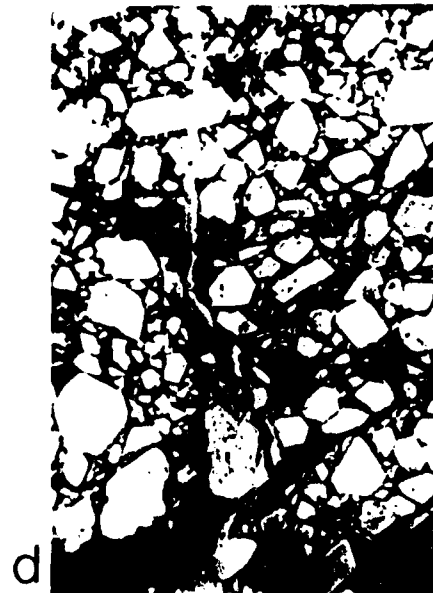
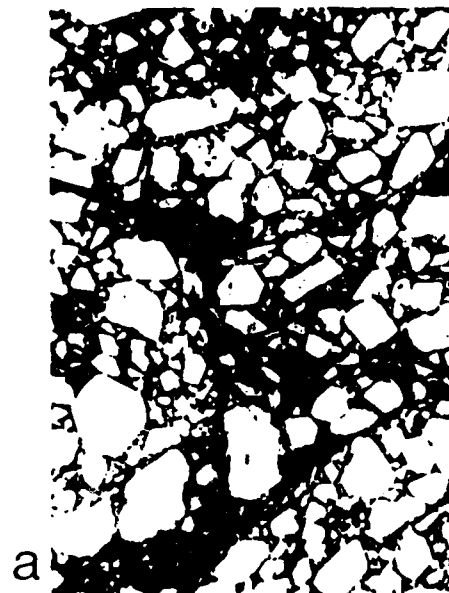
b



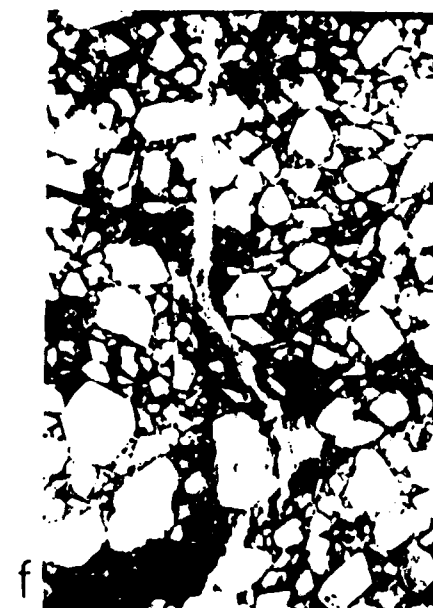
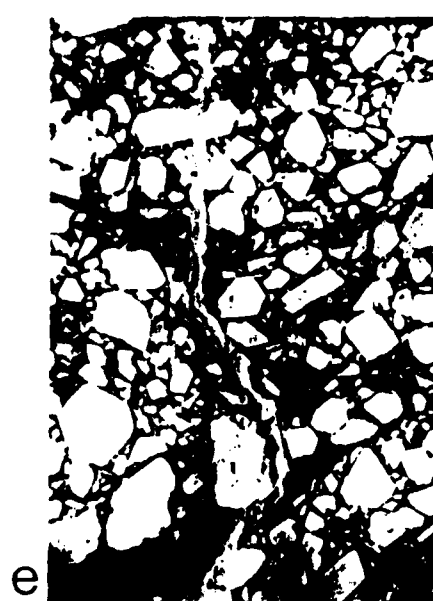
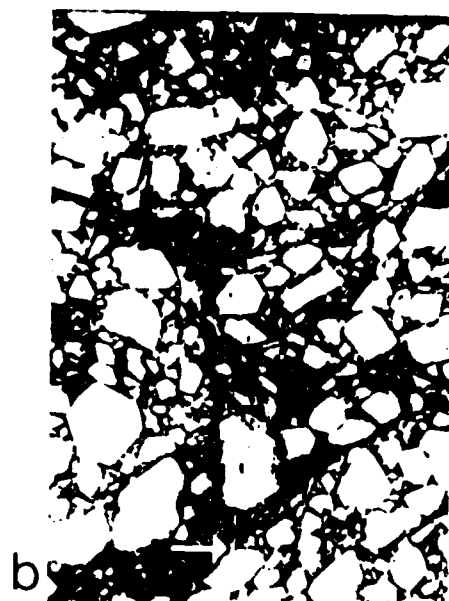
c

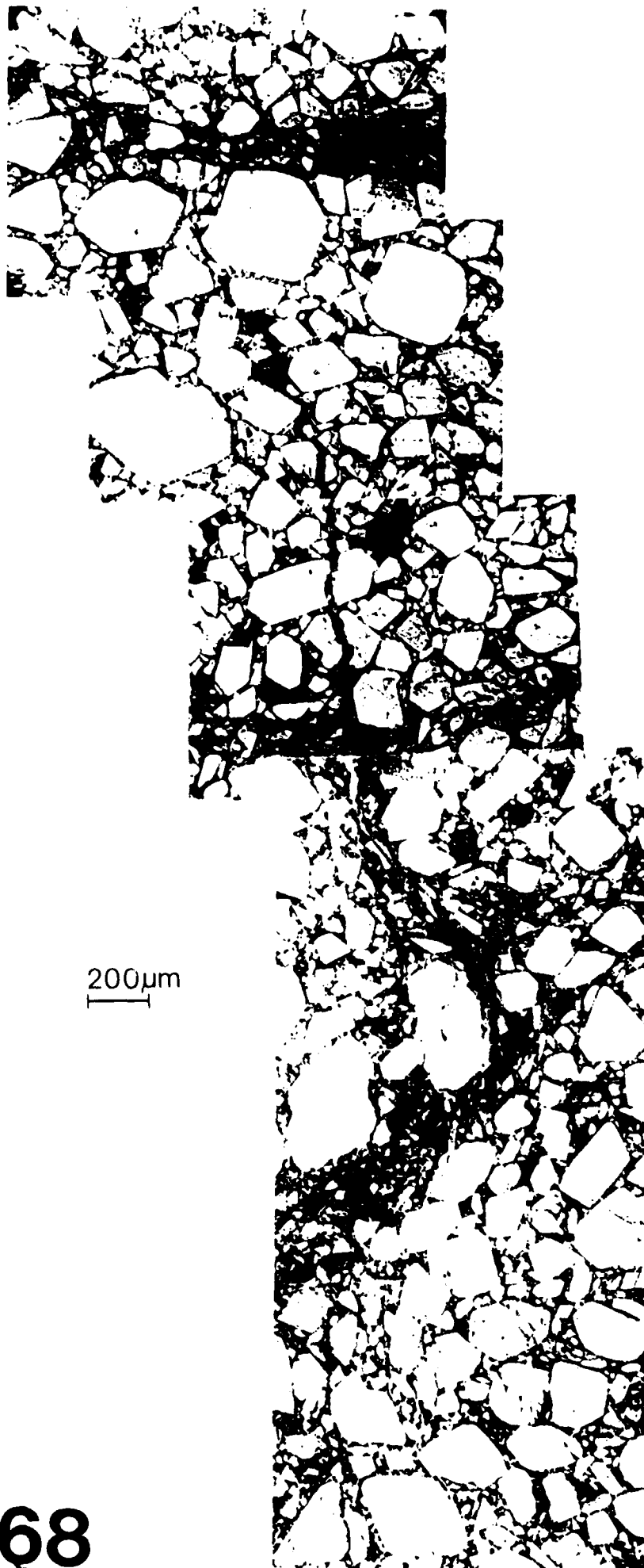


d



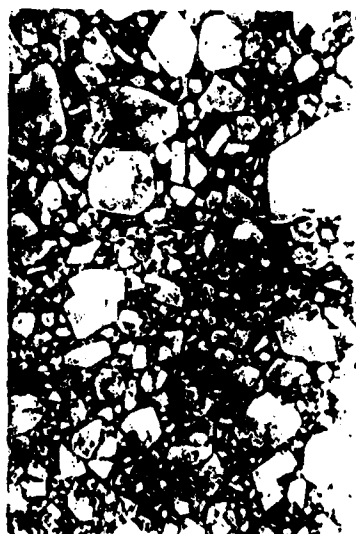
400 μ m







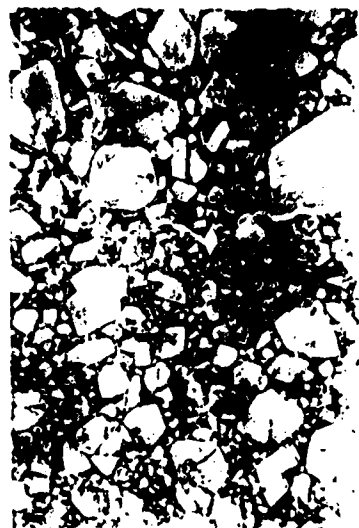
a



b



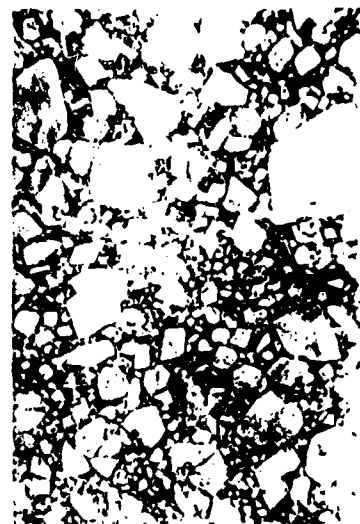
c



d



e



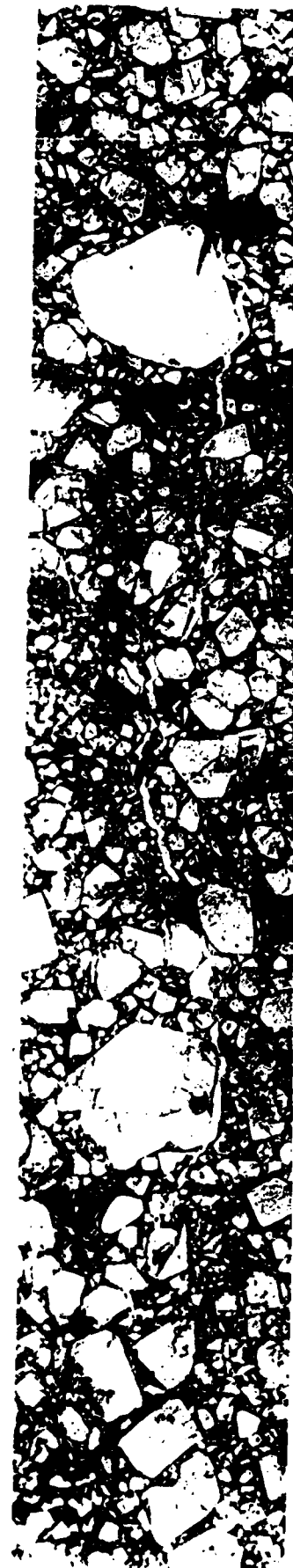
f

400 μ m

70



200μm
—



71

200μm
I